UNIVERSITY OF CALIFORNIA,
IRVINE

Directionally Controlled Thermal and Wave Transport by Phonons and Photons in Nanoporous Structures

DISSERTATION

submitted in partial satisfaction of the requirements
for the degree of

DOCTOR OF PHILOSOPHY

in Mechanical and Aerospace Engineering

by

Ziqi Yu

Dissertation Committee:
Assistant Professor Jaeho Lee, Chair
Professor Yun Wang
Assistant Professor Mohammad Javad Abdolhosseini Qomi

2020

DEDICATION

To

my parents, family

in recognition of their love and support

TABLE OF CONTENTS

LIST OF FIGURES

LIST OF TABLES

ACKNOWLEDGMENTS

I would like to deeply thank my advisor, Professor Jaeho Lee, for his continuous support, guidance, and mentorship that not only shaped my research aptitude but also my mindset of life and career. He constantly encouraged me to think and act as a scholar, who can research both an individual and a team member. He gave me the liberty to explore new areas and ideas and be responsible for the development of my projects. I had enjoyed the individual meetings, where occasional brainstorming sessions and questions came out, that oftentimes led to fruitful discussions and directions. He kindly supported me to reach out to the industry and perform internships at one of the best research institutes across the country where I met and worked with a group of brilliant researchers in several interesting and challenging multidisciplinary projects. He has been always my best example in both academic research and career development. The valuable experience and skills I have learned along the way have impacted me significantly. I also would like to appreciate Professor Yun Wang for attending both my Qualifying Exam and Doctoral Dissertation committees. Professor Wang is very knowledgeable in the field of multiphase flow and fuel cells. I am still very impressed by the questions and advice given to me and the guidance to my research and the completion of my dissertation. I especially value the experience when I was serving as a teaching assistant in his class, where I learned effective ways of communication and resolving unexpected issues. I thank Professor Mohammad Javad Abdolholsseini Qomi for serving as my Qualifying Exam and Dissertation committee members. I appreciate his kind mentorship and personal advice he gave me at various points of my time at UC Irvine. I thank Professor Tim Rupert for being on my Qualifying Exam committee, his advice to my research, and his kind support that allowed me to perform the electrodeposition using his lab equipment for one of my research projects. I also would like to be grateful to Professor Dimitri Papamaschou for joining

my Qualifying Exam committee and the questions and suggestions he kindly provided me which led me to think more deeply.

I gratefully acknowledge funding supports from the Henry Samueli School of Engineering, Samsung Electronics, and Defense Advanced Research Projects Agency. I thank Dr. Jae Choon Kim from Samsung Electronics for the research collaboration and for offering industrial perspectives to my research. In particular, his mentorship and the interaction I had during his one-year visit have been invaluable to me. I thank Dr. Jae-Hong Lim (currently affiliated to Gachon University, Korea) and Dr. Ji-won Kim (currently affiliated to Institute for Advanced Engineering, Korea) from Korea Institute of Materials Science for their research collaboration which allowed me to expose to advanced thermoelectric materials and experimentally characterized the unique properties. The interactions I had with them is a unique and precious experience during the pursuit of my doctoral degree. I also would like to thank Dr. Ercan M. Dede for the three-month internship at the Toyota Research Institute of North America (TRINA). He is a knowledgeable researcher and a great team leader. I greatly enjoyed the projects I was involved in, which significantly expanded my portfolio and broadened my horizon. I also thank Dr. Hideo Iizuka for his support and mentorship during my internship. He was always patient in our discussions and provided me with his thoughts that often led to fruitful outcomes. I appreciate the team members and colleagues at TRINA for their friendly support, care, and help throughout my entire stay.

I owe many thanks to Laia Ferrer-Argemi who was the most senior lab member, my early mentor, one of my best teammates and best friends since I joined the lab, and our expert in nanowires and 3ω measurement techniques. We worked together when the lab just started, went through hard times, and harvested significant achievements. She is always honest and straightforward to point out what I did not do well which motivated me greatly to gain

improvement and growth. Her critical thinking, unique and innovative views of research have always inspired me to learn and have always been one of my best examples in the lab. She is not only a great colleague but also a valuable friend. I also owe many thanks to Zongqing Ren who is our expert in holey silicon and thermoelectric cooling and worked with me in various projects, especially those where we needed to start from scratch with no backgrounds and explored all the resources available to us. Those times we spent and the inspirations obtained from discussions have shaped me into a more mature researcher, who is willing to and able to embrace the unknowns and challenges. I especially thank his accompany when we were working together in the cleanroom, where we went through challenges in developing fabrication recipes and harvested excitement and happiness when things worked out well. He is not only a great person to work with but also a great person to be friends with. I am grateful to Majed Sameer M. Madani, who contributed to the early development of the nanowire projects. He was very friendly and read a lot. I always enjoyed talking to him where I could learn different aspects of life. I thank Shiva Farzinazar, who is our expert in the micro lattices, for her friendship, support, and advice to my research projects and career developments. We worked on characterizing thermoelectric materials in the early stage of the lab, where I gained much experience in the experimental skills and learned a lot from her. I also appreciate Jonathan Sullivan, who is our expert in the finite-difference time-domain technique, for guiding me the method and his valuable perspectives and suggestions in my research related to optics and selective emitters. I enjoyed the time when we worked together for the micropyramidal structures and phase change materials very much. I am grateful as well to Xiao Nie who is our expert in glass bubbles and in rooftop measurements for radiative cooling coatings for giving me lots of constructive suggestions and lend helps when we worked on the theoretical and numerical investigation of microsphere composites and hierarchical materials. He was always

ready to share his thoughts and engaged in fruitful discussions. His being diligent and meticulous has impressed and motivated me greatly. I want to thank Anirudh Bharadwaj, who joined the lab at similar times as me, for his founding work in the radiative thermal transport projects and his suggestions in the selective emitters and radiative cooling materials which were very helpful for me. His excellent presentation skill has always been what I tried to catch up and sharpen. I also want to extend my appreciation to Jungyun Lim, Yi Tuan, Jiajian Luo, and Hasitha Hewakuruppu for their friendship and interactions and advice in various research projects.

Lastly, I am deeply thankful to my family for their support, patience, and sacrifice. My parents have always put my education and better development first and supported me to explore my potential in the United States. They helped me when I experienced hard times, corrected me when I made mistakes, encouraged me when I gained success, and suffered from failure. They shared my happiness and sadness and have always been my most important motivation and strongest support. I could not have reached this far without their accompany. I dedicate this thesis to them.

VITA

Ziqi Yu

2011-14	B.S. in Mechanical, Aerospace, and Nuclear Engineering, Rensselaer Polytechnic Institute
2013-14	M.S. in Mechanical, Aerospace, and Nuclear Engineering, Rensselaer Polytechnic Institute
2015-20	Graduate Student Researcher, Mechanical and Aerospace Engineering, University of California, Irvine
2016-18	Teaching Assistant, Mechanical and Aerospace Engineering, University of California, Irvine
6-9/2019	Co-op Researcher, Toyota Research Institute of North America, Ann Arbor MI

FIELD OF STUDY

Micro/nanoscale thermal transport, thermoelectrics, phononics, topological insulators, metamaterials, selective emitters

PUBLICATIONS

Peer-reviewed Journals

J1. **Z. Yu**, L. Ferrer-Argemi, and J. Lee, Investigation of thermal conduction in symmetric and asymmetric nanoporous structures, *Journal of Applied Physics*, **122** (24), 244305, 2017.

J2. **Z. Yu**, L. Ferrer-Argemi, J. Kim, JH. Lim, NV. Myung, and J. Lee, Phase-dependent thermal conductivity of electrodeposited antimony telluride films, *Journal of Materials Chemistry C*, **6** (13), 3410, 2018.

J3. **Z. Yu**, Z. Ren, and J. Lee, Phononic topological insulators based on six-petal holey silicon structures, *Scientific Reports* **9** (1), 1805, 2019.

J4. **Z. Yu**, X. Nie, A. Yuksel, and J. Lee, Reflectivity of solid and hollow microspheres composites and the effects of uniform and varying diameters, 2020, *submitted*.

J5. E.M. Dede, **Z. Yu**, P. Schmalenberg, H. Iizuka, Thermal metamaterials for radiative plus conductive heat flow control, *Applied Physics Letter*, **116**, 191912, 2020. (**Featured Article**)

J6. Z. Ren, **Z. Yu**, J.C. Kim, and J. Lee, TSV-integrated thermoelectric cooling by holey silicon for hot spot thermal management, *Nanotechnology* **30** (3), 035201, 2018.

J7. L. Ferrer-Argemi, **Z. Yu**, J. Kim, N.V. Myung, J.H. Lee, and J. Lee, Silver content-dependent thermal conductivity and thermoelectric properties of electrodeposited antimony telluride thin films, *Scientific Reports*, **9** (1), 9294,2019.

J8. L. Ferrer-Argemi, **Z. Yu**, and J. Lee, Effects of metal silicide inclusion interface and shape on thermal transport in silicon nanocomposites, *Journal of Applied Physics*, **126** (3), 035106, 2019.

J9. M. Sala-Casanovas, A. Krishna, **Z. Yu**, and J. Lee, Bio-inspired stretchable selective emitters based on corrugated nickel for personal thermal management, *Nanoscale and Microscale Thermophysical Engineering*, **23** (3), 173, 2019. (**Cover Page Article**)

J10. H. Yu, J. Wang, B. Deng, X. Wei, Y.K. Wong, W.L. Chan, K.M. Tsang, and **Z. Yu**, Chaotic phase synchronization in small-world networks of bursting neurons, *Chaos: an interdisciplinary journal of nonlinear science* **21** (1), 013127, 2011.

Conference Proceedings

C1. **Z. Yu**, L. Ferrer-Argemi, and J. Lee, Temperature-dependent thermoelectric properties of electrodeposited antimony telluride films. *In: Proceedings of the IEEE 17th Intersociety Conference on Thermal and Thermomechanical Phenomena in Electronic Systems*. San Diego, CA, 2018.

C2. **Z. Yu**, Z. Ren, and J. Lee, Investigation of thermal metamaterials based on nanoporous silicon using ray tracing and finite element simulations. *In: Proceedings of the IEEE 18th Intersociety Conference on Thermal and Thermomechanical Phenomena in Electronic Systems*. Las Vegas, NV, 2019. **(Best Paper Award)**

C3. Z. Ren, **Z. Yu**, and J. Lee, Hotspot management by holey silicon-metal composites for 1 kW/cm^2 and beyond. *In: Proceedings of the IEEE 18th Intersociety Conference on Thermal and Thermomechanical Phenomena in Electronic Systems*. Las Vegas, NV, 2019.

C4. J. Sullivan, L. Ferrer-Argemi, **Z. Yu**, and J. Lee, Wafer-scale hierarchically textured silicon for surface cooling. *In: Proceedings of the IEEE 18th Intersociety Conference on Thermal and Thermomechanical Phenomena in Electronic Systems*. Las Vegas, NV,2019.

Conference Presentations

P1. **Z. Yu** and J. Lee, Thermal transport modeling of asymmetric nanostructures by Monte-Carlo ray tracing. *In: The 36th International Conference on Thermoelectrics*. Pasadena, CA, 2017.

P2. **Z. Yu** and J. Lee, Temperature-dependent thermoelectric properties of electrodeposited antimony telluride films. *In: IEEE 17th Intersociety Conference on Thermal and Thermomechanical Phenomena in Electronic Systems*. San Diego, CA, 2018.

P3. **Z. Yu**, L. Ferrer-Argemi, and J. Lee, Thermal transport in electrodeposited antimony telluride films with varying silver contents. *In: 2019 Spring Materials Research Society Meeting & Exhibit*. Phoenix, AR, 2019.

P4. **Z. Yu**, Z. Ren and J. Lee, Investigation of thermal metamaterials based on nanoporous silicon using ray tracing and finite element simulations. *In: Proceedings of the IEEE 18th Intersociety Conference on Thermal and Thermomechanical Phenomena in Electronic Systems*. Las Vegas, NV, 2019.

ABSTRACT OF THE DISSERTATION

Controlled Thermal Transport by Phonons and Photons in Nanoporous Structures

by

Ziqi Yu

Doctor of Philosophy in Mechanical and Aerospace Engineering

University of California, Irvine, 2020

Professor Jaeho Lee, Chair

Intriguing transport phenomena of phonons and photons in nanoporous structures have revolutionized the development of materials in recent decades. The particle- and wave-like transport of phonons have respectively demonstrated significant thermal conductivity reduction in thermoelectrics and backscattering-immune waveguiding in topological insulators; the photon transport in nanoporous composites have demonstrated enhanced solar reflectivity for radiative cooling. This doctoral research focuses on understanding phonon and photon transport in nanoporous structures that will guide optimal designs of thermoelectric energy harvesting systems, future phononic circuits, and hierarchical materials for optical and thermal management.

Phonon transport can be viewed in the particle-like picture when the phonon wavelength is much shorter than the structure's critical dimension. A good example is heat conduction in solids at THz frequencies. Though significant thermal conductivity reduction due to phonon size effect has been observed in nanoporous structures, the presence of various geometric parameters complicates the understanding of governing mechanisms. To investigate phonon-boundary scattering phenomena in Si nanoporous structures with varying pore shapes, alignments, and size distributions, we develop a ray tracing technique that is experimentally validated by bulk Si and Si nanomeshes. The results show that, with identical porosities, asymmetric pore shapes offer a

lower thermal conductivity than symmetric ones due to smaller neck sizes that localize heat fluxes; asymmetric pores with fully diffuse surface boundaries show possibilities of realizing a thermal rectification ratio up to 13 by optimally controlling phonon injection angles. Symmetric pore shapes arranged in a hexagonal-lattice provide a lower thermal conductivity than in a squared-lattice due to the limited phonon line of sight; alternating pore size distributions yield a lower thermal conductivity than uniform ones at the same porosity. When phonon wavelength is much longer than the structure's critical dimension, phonon transport is wave-like. One frequently asked question in condensed matter physics was if the Quantum Spin Hall Effect observed in electrons and photons could be analogously realized for phonons despite their lacking spin-like degrees of freedom and transverse polarizations. Here we numerically demonstrate a six-petal holey Si-based topological insulator, where simple geometric control enables topological edge states for both in- and out-of-plane phonon polarization up to GHz ranges with a submicron periodicity. The unique six-petal geometry induces zone-folding to form a double Dirac cone and breaking discrete translational symmetry leads to the topological phase transition. Our design supports robust backscattering-immune elastic wave transmission up to 90% despite the existence of geometric uncertainties. Though the design has not yet been demonstrated by experiments due to nanofabrication and measurement challenges, the numerical results clearly show the signature of topologically-protected edge transport of phonons, evident by the band inversion and backscattering-immunity. The improved understanding of particle- and like-like phonon transport in Si nanoporous structures regarding phonon-boundary scattering phenomena and phononic topological insulators will pave the way for developing future thermoelectric energy harvesting systems and phononic circuits.

As another bosonic particle, photon's transport can also be modified by nanoporous structures. Here we focus on understanding the enhanced solar reflection realized by dielectric nanoporous composites, which is important for designing selective emitters that are attractive for radiative thermal management. We employ Mie theory and finite-difference time-domain simulations to study the solar reflectivity of SiO_2 and TiO_2 microspheres in a polydimethylsiloxane (PDMS) matrix. Our analysis shows that hollow microspheres with a thinner shell are more effective in scattering the light, compared solid microspheres, and lead to a higher solar reflectivity. The high scattering efficiency, owing to the large interface density, in hollow microspheres allows low-refractive-index materials to have high solar reflectivity. The uniform- and varying-diameter design of 0.75 μm and 0.5-1 μm provide the highest solar reflectivity of 0.81 and 0.84, respectively. The effect of varying diameter is characterized by strong backscattering in the electric field. The enhanced solar reflectivity and effectiveness of hollow glass microsphere composites for radiative cooling have been experimentally demonstrated in our recent work. The findings in the current work will guide the optimal designs of microsphere composites and hierarchical materials for optical and thermal management systems.

Chapter 1 INTRODUCTION

1.1 Phonon Transport in Nanoporous Structure and Thermal Conductivity Reduction

Understanding the thermal transport in porous materials has far-reaching significance in applications of thermoelectric energy conversion, thermal energy storage, thermal management, and proton exchange membrane fuel cells [1,2]. Reduced thermal conductivity from its bulk value has been demonstrated by inducing phonon-boundary scattering on top/bottom surface boundaries in Si thin films [3–6]. The thin-film thermal conductivity can be further reduced by introducing microporous or nanoporous patterns [7–14]. While the experimental characterization of Si nanoporous structures of varying geometries are abundant in the literature, theoretical explanations regarding the reduced thermal conductivity and the mismatch between the experimental data and predictions based on the classical phonon transport model have not yet come into a conclusive agreement. Despite the intensive study of phonon coherence in superlattice thin films with atomically smooth interfaces between alternating layers, where coherent phonon transport becomes dominant at 300 K for periodicity smaller than 5 nm [15,16]. It has been long debated if the phonon coherent effect, or phononic effect, should be responsible for the thermal conductivity reduction experimentally observed in periodic Si nanoporous structures, or phononic crystals, at room temperature with critical dimension from 10 nm to 100 nm (see Figure 1.1). Such debate partially originates from the challenge to fabricate ultrathin patterns with pitches less than 10 nm to impact the short-wavelength phonons at room temperature [17,18] and the rough pore edges [13,19,20] that destroy coherent phonon phases [21]. Phonon particle effect, where the majority of phonon wavelengths is smaller compared to the critical size of the structure, leads to phonon scattering on surface boundaries, which can significantly suppress the phonon mean free path and

results in lower thermal conductivity. Recent work suggested unimportant phonon coherent effects to the thermal conduction in Si nanoporous structures with pitches greater than 100 nm and at temperatures higher than 14 K [7]. Early experimental observations [10,22–26] made on Si phononic crystals, where potential phonon coherent effects were reported, are now often explained by the amorphous pore edges and thermal contact resistance [25,27]. With negligible phonon coherence at 300 K in the reported samples acknowledged [7,17,28,29], the observed thermal conductivity reduction is expected to be explained by the phonon size effect. Despite the still on-going debate on the reduced thermal conductivity contributed by coherent and incoherent phonon transport and the relevant research progress, the key mechanisms of phonon transport in Si nanoporous structures without considering the coherent effect also requires attention. The presence of multiple geometrical parameters including the film thickness, pore shapes, and neck sizes complicate the understanding of thermal conduction in these structures [30] (see Figure 1.1). Simple theoretical models based on Boltzmann-Transport-Equation and kinetic theory assuming a constant phonon mean free path are not able capture the complex multi-dimensional phonon-boundary scattering phenomena in complicated structures. To cope with this challenge and provide physical insights into the effects of geometry on the phonon transport in nanoporous Si thin films, this work has developed a Monte Carlo ray tracing model, where detailed phonon trajectories are tracked, enabling the calculation of phonon-boundary mean free path in complicated pore geometries. By systematically investigating varying pore shapes, pore alignments, and pore size distributions, we identify key mechanisms that are primarily responsible to thermal conductivity reduction in symmetric and asymmetric Si nanoporous structures and discuss the possibility of realizing thermal rectification using asymmetric nanopores enabled by the ballistic phonon transport at low temperatures and optimal control of phonon injection angles.

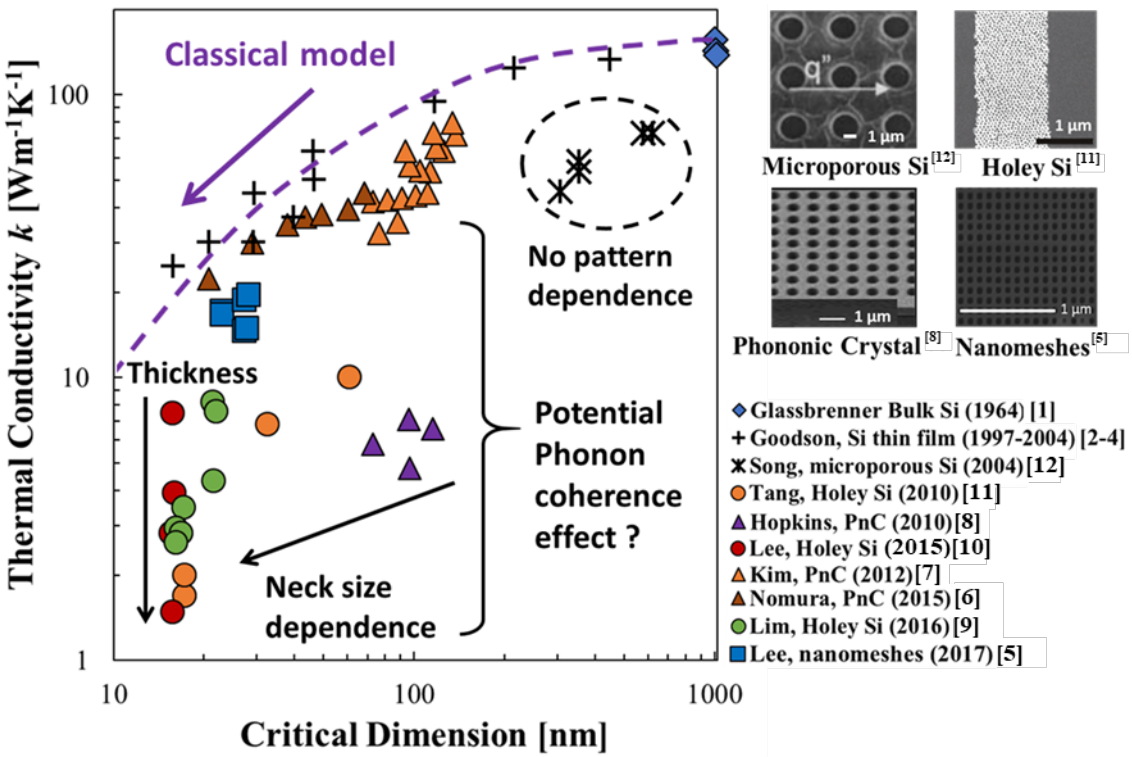

Figure 1.1 Experimental data for thermal conductivity of bulk Si, Si thin films, and Si nanoporous structures vs. the critical dimension of the structure. The classical model based on phonon particle effect is not able to capture complex multi-dimensional phonon-boundary scattering phenomena in such complicated structures. The presence of multiple geometrical parameters complicates the understanding of key mechanisms that are primarily responsible for the thermal conductivity reduction. The potential phonon coherence effect cast doubt onto the applicability of the phonon particle-based model to explain the thermal transport in Si nanoporous structures when the pitch goes sub-100 nm above the cryogenic temperature.

1.2 Phonon Transport for Novel Phononic Wave Control

The discovery of the topological states of matters is one of the most important highlights in the development of condensed matter physics [31,32]. The enriched physics underlying the electronic topological states, such as Quantum Hall Effect [33], Quantum Spin Hall effect, Valley Hall effect, have opened new opportunities for fundamental research and practical applications including topological quantum computing. The robust edge states that are immune to the backscattering due to the bulk-boundary correspondence [34,35] may benefit applications in low-

power electronics and spintronics. Since first discovered in electron gases, the Quantum Hall effect was demonstrated in graphene [36,37], and then carried over to photonic systems [38–40]. Time-reversal symmetry can be broken by a static magnetic field for both electrons and photons due to their spin nature [41]. The difference is that electrons are charged whereas photons are electrically neutral; breaking time-reversal symmetry in photonic systems is done by constructing both static and time-harmonic couplings that stimulate the electron's behavior in a uniform magnetic field [40]. The phononic analog of the Quantum Hall effect is indeed challenging as phonons are charge-neutral (magnetic inert) [41]. Early attempts to mimicking the Quantum Hall effect in phononic systems, such as acoustic systems, involved constructing sound vorticity [42], using resonators [43], and circulating fluids [44–47]. Though at first sight, these approaches are intuitively obvious according to the underpinning mechanism, their practical implementation is difficult due to the requirement of high rotating speed which inevitably leads to nonlinear and viscous effects. For mechanical systems, available mechanically rotating components including gyroscopes or direct-current motors can be easily incorporated [48]; another mechanism that is based on centrifugal forces in spring-coupled mass systems has also be explored [49]. Though effective, these components are bulky and may not be applicable for systems where only constrained space is allowed. As an alternative way to introduce spin-like states, by emulating the Quantum Spin Hall effect in electronic systems due to strong spin-orbit coupling [50–52], the pseudospin scheme has been successfully demonstrated in phononic systems [53,54] to mimic the Kramers pair intrinsic for electrons but lacking for phonons. One study [54] used a metallic rod-air configuration and demonstrated the pseudospin states induced by the hybridization of a pair of acoustic vortices carrying opposite orbital angular momenta. The two pseudospins support the acoustic flux flowing along the interface between the two topologically distinct phononic crystals and the propagation

of acoustic waves is backscattering-immune. A different scheme based on the zone-folding effect has also be developed and demonstrated for phononic topological insulators [55–65]. This effect maps the Dirac cone located at the Brillouin zone corners K and K' points back to the Brillouin zone center, and thus form a double Dirac cone with dipole and quadruple modes. These modes then hybridize to form vortex states, emulating the Kramers degeneracy. The topological phase transition is done by tuning the geometrical parameters that break the symmetry [55]. For elastic waves, extra considerations on their polarization are required for realizing pseudospin states as these polarizations can mix in most solid materials; other than this, the slow wave speed and high density of states poses challenges as well [64]. Detailed understanding and systematic investigation of realizing topological edge states for elastic waves of longitudinal, transverse, or both are needed, especially in miniaturized platforms, such as nanoscale, where the on-chip applications requiring the integration to modern electronics and quantum computing systems can be made possible. My research has developed a novel six-petal holey structure using Si, which is one of the most matured Complementary-Metal-Oxide-Semiconductor-compatible materials, and numerically demonstrate the realization of phononic topological insulators that support backscattering-immune propagation of elastic waves in both in- and out-of-plane directions. The work provides insights into the relationship between geometries and topological properties. The robustness and unique unidirectional propagation capability of the design may benefit potential applications such as advanced lossless waveguiding and phononic computing.

1.3 Photon Transport in Nanoporous Structures and Radiative Cooling

Finding a cost-effective and eco-friendly alternative to the widely-used electricity-driven cooling methods for human-made structures [66–69], such as buildings, have received great attention in recent years due to the aggressive urbanization in response to the population growth [66]. Radiative cooling coatings, that efficiently reflects solar irradiation [70] in the wavelength range of 0.4 to 2.4 μm and emits in the mid-infrared wavelength [71] between 8 to 13 μm, can be a promising candidate thanks to its passive nature that requires no energy consumption and low impact to the ecosystem by incorporating environmental-friendly materials [66]. The experimental demonstration of radiative cooling based on Si or SiO_2-based layered structures [72], dielectric pigments-embedded paints [73,74] and polymer-particle composites [75–77] with metal mirrors are abundant in the literature. However, they face challenges either due to the cost [76] and complicated processing or undesired heating due to limitations of the intrinsic material properties of their constituents. Novel solutions have overcome these challenges by developing close-packed silica microsphere [78] and nanoporous structures, such as glass bubbles [66] and porous polymers [67], which enable simple fabrication and scaling up. Hierarchical coatings [67], in which scatters of contrasting sizes are combined in a random media, have shown effective optical scattering across the solar wavelength due to the blended optical response of building blocks of varying sizes [79]. Though, ultrahigh solar reflectivity over 92% has been achieved by varying-diameter glass bubble composites [66] and porous P(VdF-HFP) [67]. Understanding of photon transport in such systems and driving mechanisms relevant to the optical properties remains relatively unclear. The study focusing on the investigation of photon transport in hollow microspheres with varying diameters has only received limited attention, which is in sharp contrast to their success in achieving effective radiative cooling. Systematic investigations into the effects of the diameter

variation and relevant geometrical parameters are vital for guiding future optimal designs of hollow microsphere composites and hierarchical materials for thermal and optical management systems. My research has used Mie theory and finite-difference time-domain simulations and showed the geometrical parameters of SiO_2 and TiO_2 microspheres that lead to high solar reflectivity, identify the driving mechanisms for the optical property, and discuss the effects of varying diameter.

1.4 Outline of Doctoral Research

Chapter 2 presents the thermal conductivity calculation based on the Monte Carlo ray tracing technique and identifies the key mechanisms of multi-dimensional phonon boundary scattering phenomena in symmetric and asymmetric Si nanoporous structures with varying pore shapes and identical porosities, varying pore alignments, and varying pore size distributions. Chapter 3 investigates the possibilities of realizing thermal rectification based on asymmetric Si nanoporous structures using the ray tracing simulation and presents the optimal design and strategy for maximizing thermal rectification ratio with fully diffuse pore surface boundaries. Chapter 4 presents a novel six-petal holey Si nanoporous structure for achieving phononic topological insulators using finite-element simulations and performs a detailed analysis of the relationship between the geometry and topological properties. Chapter 5 shows the Mie theory and finite-difference time-domain simulation results for achieving a high solar reflectivity driven by the photon transport in hollow microsphere composites of varying shell thicknesses and materials when the diameter is uniform and varying. Chapter 6 offers concluding remarks on the phonon and photon transport in nanoporous structures for controlled thermal transport and opportunities for future research advancements.

CHAPTER 2: INVESTIGATION OF THERMAL CONDUCTION IN SYMMETRIC AND ASYMMETRIC NANOPOROUS STRUCTURES

Nanoporous structures with a critical dimension comparable or smaller than the phonon mean free path have demonstrated significant thermal conductivity reduction and are attractive for thermoelectric applications, but the presence of various geometric parameters complicates the understanding of governing mechanisms. Here we use a ray tracing technique to investigate phonon boundary scattering phenomena in Si nanoporous structures of varying pore shapes, pore alignments, and pore size distributions, and identify mechanisms that are primarily responsible for thermal conductivity reductions. Our simulation results show that the neck size, or the smallest distance between the nearest pores, is the key to understanding nanoporous structures of varying pore shapes and the same porosities. When the neck size and porosity are both identical, asymmetric pore shapes provide a lower thermal conductivity compared with symmetric pore shapes, due to localized heat fluxes. For symmetric nanopore structures, hexagonal-lattice pores achieve larger thermal conductivity reduction than square-lattice pores due to the limited line-of-sight for phonons. We also show that nanoporous structures of alternating pore size distribution from large to small pores yield a lower thermal conductivity compared with those of uniform pore size distributions in the given porosity.

2.1 Introduction

Si nanoporous structures [7,9–14,25,27,80] have demonstrated significant thermal conductivity reductions beyond the predictions of classical models [3,81–83]. While the possibilities of selectively scattering phonons and reducing the thermal conductivity without sacrificing electrical properties are promising for thermoelectric applications, theoretical interpretations of thermal transport mechanisms in nanoporous structures are challenging. One of the major challenges in understanding thermal transport in nanoporous structures is in modeling

the phonon mean free path for multi-dimensional geometries or nanostructures with rough boundaries [84] or intersecting channels [83] that induce complex boundary scattering. Though having shown successes in capturing thermal transport and explaining size dependencies in simple nanostructures [6,86] simple boundary scattering models using constant mean free path values without Monte Carlo [85,87] or ray tracing treatment may not be appropriate for studying nanoporous structures. Detailed information about phonon trajectories for varying pore shapes and alignments is necessary to explain important thermal transport mechanisms. Ray tracing technique [7,86,87] can track a transport path of individual phonons, fully accounting for complex phonon boundary interactions in nanoporous structures. A recent study of Si nanomeshes [7] presented a good agreement between the thermal conductivity predicted by using the ray tracing technique and experimental investigations and validated that particle-based BTE models can successfully capture thermal transport phenomena in Si nanostructures when the artificial periodicity is larger than 100 nm and when the temperature is above 14 K. Various physical mechanisms have been proposed to explain thermal conductivity reductions in nanoporous structures such as phonon coherence and wave-related effects [10,24,25,27], phonon backscattering and multiple boundary scattering [84,88], increased defect concentration [89], and native oxide effects [20]. While the thermal transport studies have mostly explored the size effects in nanoporous structures, the impacts of nanopore shape, alignment, and distribution on phonon boundary scattering have received relatively little attention. Hao et al. presented a modified phonon mean free path to replace the time-consuming Monte-Carlo (MC) simulation by comparing the latter with the kinetic theory and demonstrated good applicability in circular and squared nanopores [90,91]. A weak pore shape dependency was found in their observations, motivating a more comprehensive inspection comparing other pore shapes. Accordingly, Romano and Grossman solved the mean-free-path-

BTE to study thermal transport dependence on pore shapes (squared, circular, and triangular) and alignments (squared and staggered) when porosity remains the same [92]. They attributed thermal conductivity disparity between different pores to the dissimilar neck size. However, the precise understanding of thermal conductivity reduction mechanisms in nanoporous structures is missing due to the lack of studies controlling the neck size and the porosity at the same time. It is also important to study the effect of temperature on Si nanoporous structures due to their increasing relevance to high-temperature thermoelectric generators and low-temperature cooling systems. Wang *et al.* used the 3ω technique and the Debye model assuming a frequency-dependent grain boundary scattering to explain the temperature-dependent thermal conductivity of polycrystalline materials from 16 to 310 K [93]. Romano *et al.* solved the mean free path-dependent BTE to show the temperature-dependent thermal conductivity of Si nanoporous structures with the periodicity of 10 nm from 100 K to 300 K [94]. However, investigations of a wider temperature range, which are relevant to both fundamental understanding and technological aspects of thermoelectric systems, are still needed. In this study, we use a ray tracing technique as investigation tool and systematically identify thermal transport mechanisms in nanoporous structures of various pore shapes, neck sizes, pore alignments, and pore size distributions over a wide temperature range and provide design guidelines to induce thermal rectification and maximize thermal conductivity reductions for the fixed porosity in artificially engineered nanoporous structures.

2.2 Methodology

We use the Landauer formalism [95,96] to compute the thermal conductivity by correlating the thermal conductance G with the phonon transmission function $\mathcal{T}(\Omega, \omega)$ as

$$G = \frac{A}{4}\int C_v \langle \mathcal{T} \rangle v_g d\omega, \tag{1}$$

where A is the cross-sectional area, C_v is the volumetric heat capacity, Ω is the solid angle, ω is the angular frequency, and v_g is the phonon group velocity. We obtain an averaged transmission coefficient $\langle \mathcal{T} \rangle = \int_0^{2\pi} \int_0^{\pi/2} \tau(\theta, \phi, A) \cos\theta \sin\theta d\theta d\phi dA/\pi A$ using ray tracing simulations with Monte-Carlo integration, where θ denotes the polar angle, and ϕ is the azimuthal angle.

The thermal conductivity k is related to the thermal conductance G in intrinsic materials by $k = \frac{GA}{L}$, where L is the length. However, to account for a conductance reduction due to material removal caused by the patterned nanopores, the above formula needs to be modified by a porosity correction factor f as

$$k = \frac{GL}{fA}. \tag{2}$$

For squared and circular pores, f can be approximated using the classical relation $\frac{1-\phi}{1+\phi}$[92,97] whereas for other shapes we perform a series of numerical simulations using finite-element-methods and correlate f with ϕ by polynomial fitting [7]. These correction factors are detailed in TABLE 2.1.

The thermal conductivity is calculated by using the kinetic theory as [98]

$$k = \frac{1}{3} \int C_v v_g \Lambda d\omega \tag{3}$$

where Λ is the phonon mean free path and ω is the phonon frequency. We use the full phonon dispersion relations by taking quadratic fits of each phonon dispersion branch in bulk Si obtained from neutron scattering data,[99,100] which derives Eq. (4) considering Eq. (3) as

$$k = \frac{1}{6\pi^2} \sum_n \int C_v(\omega, n) v_g^2(\omega, n) \tau(\omega, n) D(\omega, n) d\omega, \tag{4}$$

where $D(\omega, n)$ is the phonon density of states and n is the phonon mode. As suggested by previous works of Si nanostructures [101–106], especially the recent study of Si nanomeshes [7] with comparable dimensions, the optical branches contribute negligibly to thermal conductivities. Hence, in this work, we only consider the longitudinal acoustic (LA) branch and two transverse acoustic (TA) branches. The quadratic fits approximating the phonon dispersion relation can be expressed as $\omega_q = \omega_0 + v_s q + cq^2$ [99,100] where ω_q and q denote the phonon frequency and the phonon wavevector, respectively. For the LA and TA branches, the fitting coefficients are $\omega_{0,LA} = \omega_{0,TA} = 0\ \frac{rad}{s}$, $v_{s,LA} = 9010\frac{m}{s}$, $v_{s,TA} = 5230\ \frac{m}{s}$, $c_{LA} = -2 \times 10^{-7}\frac{m^2}{s}$, and $c_{TA} = -2.26 \times 10^{-7}\frac{m^2}{s}$ [99,100]. The group velocities are determined by explicitly expressing v_g as $\frac{d\omega}{dk}$ which can be readily obtained from the above quadratic fits [107,108]. Different phonon scattering mechanisms are combined via Matthiessen's rule under relaxation time approximation, in which $\tau^{-1} = \tau_b^{-1} + \tau_U^{-1} + \tau_{imp}^{-1}$, where the subscripts denote phonon-boundary, -Umklapp, and -impurity scattering, respectively. We use the expressions of relaxation time detailed in the previous study [7] to compute Umklapp and impurity scatterings, which are $\tau_U^{-1} = P\omega^2 T\exp\left(-\frac{C_U}{T}\right)$ and $\tau_{imp}^{-1} = C_I\omega^4$, where $P = 1.53 \times 10^{-19}\frac{\mathrm{S}}{\mathrm{K}}$, $C_U = 144$ K, and $C_I = 2.54 \times 10^{-44}$ s^3. Detailed derivation of the modeling of the thermal conductivity *k* can be found in Appendices 1.

The phonon coherence and wave effects are neglected in our simulations because the geometries of interest in this study are much larger than the length scale where phonon wave-interference may become significant [7,85]. The validity of combining ray tracing boundary scattering with frequency-dependent intrinsic scattering when predicting the thermal conductivity [7,109,110] is first assessed and the details can be found in the supplementary material. Hence, the mean free path for phonon boundary scattering Λ_b is determined by comparing Eq. (1) and Eq. (3).

We follow the previous work [7] and calculate Λ_b at the long-length limit where it saturates to the diffuse limit.

$$\Lambda_b = \frac{3L\langle \mathcal{T} \rangle}{4f} \tag{5}$$

There has been debate over using 2D or 3D ray tracing; the former significantly reduces computational load while the latter reflects more precisely the phonon transport in 3D nanoporous structures [111]. In this work, we choose the 2D ray tracing since we are interested in thermal transport in laterally confined systems, where boundary scattering phenomena on the top/bottom surface boundaries are not very relevant. We select a unit cell based on which the entire geometry can be recovered by translational and mirror symmetry. For top and bottom boundaries, we impose specular boundary conditions, while for left and right boundaries, we impose periodic boundary conditions allowing exit and re-entrance of the phonon. We conduct ray tracing assuming mode-independent phonon boundary scattering which has been well validated in the previous studies [7,112]. If the surface is fully specular, a phonon will undergo specular reflection, whereas, for the rough surface, phonon direction is fully randomized after each diffuse scattering. The good agreement of calculation with experimental data for Si nanowires [113,114] validated the fully diffuse approximation. In each simulation, we launch at least 5×10^5 total phonons to ensure the fluctuation of the calculated phonon transmission coefficient is within 5‰. The detailed procedure of our ray tracing simulations can be found elsewhere [7].

We have successfully validated our ray tracing simulation and thermal conductivity model against previous works of Si nanomeshes [7,85] and bulk Si [81]. The details are presented in section 2.3.

2.3 Validation of Ray Tracing Technique

We first validate our BTE model against the previously reported experimental data of bulk Si [81]. We use the same phonon scattering parameters reported in the literature [7] and a good agreement between the calculation results and experimental data can be found, as seen in Figure 2.1(a). This demonstrates that the model we develop to compute the thermal conductivity in this work is valid.

We also validate our ray tracing code by reproducing a previous work of Si nanomeshes [85]. The nanomeshes have a neck size of 23 nm, periodicity in the direction of heat flow of 34 nm, and a thickness of 22 nm. To have a fair comparison, we apply the same phonon dispersion relation and phonon scattering rates for Umklapp and phonon-impurity scatterings. We calculate the temperature-dependent thermal conductivity of Si nanomeshes using our ray tracing algorithm and thermal conductivity model, the results agree well with those predicted by reducing variance Monte-Carlo method, as seen in Figure 2.1(b). This indicates that our ray tracing algorithm can successfully capture the thermal transport in complex Si nanoporous structures.

When modeling the thermal rectification, we assume ballistic phonon transport which requires phonon mean free path to be comparable or larger than the critical dimension of the nanostructure. This requirement may be violated when the rectifiers involve large base angle triangles (e.g., 85 º - 80 º design presented in section 3.2) allowing longer distance for phonons to travel before reaching any of the surrounding pore interfaces. In this case, for thermal conductivity or conductance to be calculated, we use relaxation time approximation, where Matthiessen's rule is needed to compute the effective phonon mean free path due to different scattering mechanisms. Although all simulation results in the following sections only consider boundary scattering, which is the dominant scattering mechanism at low temperatures, we validate that the phonon effective phonon mean free path predicted by ray tracing considering only boundary scattering is compatible

with explicitly including both boundary and Umklapp scatterings in the ray tracing simulations. The Umklapp scattering is incorporated by randomly drawing a phonon free path associated with each scattering event by the equation $-\Lambda_U \ln(\zeta)$, where ζ is a random number between 0 and 1. We simulate three designs with base angles being: 60º - 30º, 75º - 60º, and 85º - 80º. The value of Λ/Λ_B is computed for Λ_U/Λ_B ranging from 0.01 to 10, which covers ballistic to diffusive phonon transport regimes, by ray tracing (points) and by Matthiessen's rule (dashed line). The good agreement between data points and the dashed curve as seen in Figure 2.1(c) proves that combining ray tracing with Matthiessen's rule is valid. Figure 2.1(d) illustrates representative phonon trajectories when the phonon is undergoing ballistic, quasi-ballistic, and diffusive transport.

Finally, we also compare our ray tracing results with a recent study of Si nanomeshes [7]. The comparisons between reproduced and reported backscattering fraction, thermal conductance ratio, and long length limit diffuse boundary scattering mean free path are shown in Figure 2.2 We use the same phonon dispersion relation and scattering rates and our results agree very well with theirs. The small discrepancies can be attributed to statistical uncertainties.

In TABLE 2.1, we summarize the pore-shape-dependent porosity correction factor calculated by FEM simulations. These results are developed for the porosity of 25%, matching up with the porosity set throughout all the ray tracing simulations.

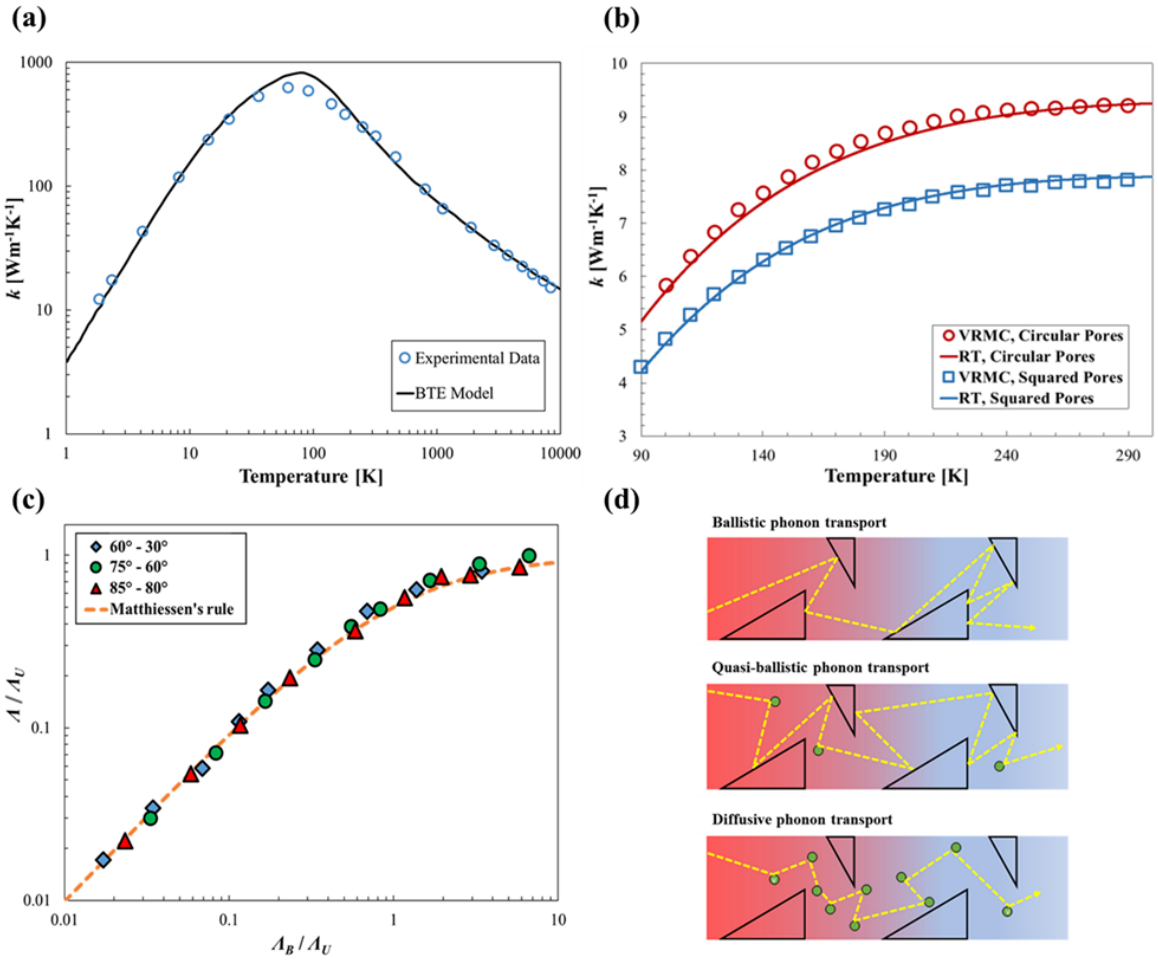

Figure 2.1 (a) The thermal conductivity of bulk Si calculated by our thermal conductivity model as compared with the experimental data [81]. The good agreement indicates the validity of our model. (b) Thermal conductivities calculated by using the variance-reduced Monte-Carlo simulation [85] and ray tracing simulation for Si nanoporous structures with squared and circular pores of aligned distributions. The periodicity is 34 nm, the neck size is 23 nm, and the thickness is 22 nm. We find a good agreement between thermal conductivities predicted by both methods, validating our ray tracing simulations. (c) The ratio of total phonon mean free path to boundary scattering mean free path determined by combining the ray tracing simulation and the Matthiessen's rule is compared with that including boundary scattering and intrinsic scattering in ray tracing simultaneously. The good agreement between the curve and points demonstrated that combining ray tracing boundary scattering with frequency-dependent intrinsic scattering via Matthiessen's rule is valid. (d) Schematics showing the representative phonon paths for ballistic, quasi-ballistic, and diffusive phonon transport regimes.

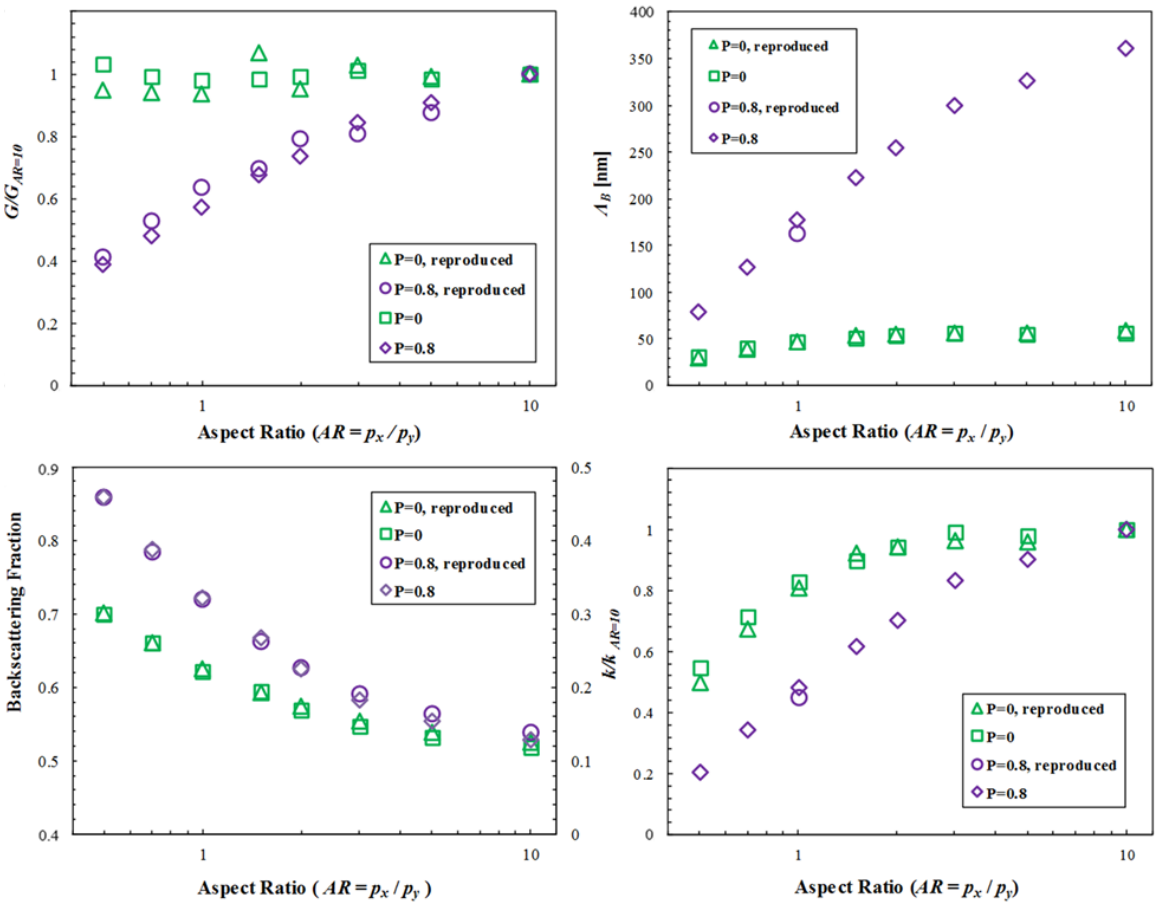

Figure 2.2 The reproduction of a recent work of Si nanomeshes [7]. (a)Thermal conductance ratio, (b) Phonon boundary scattering mean free path, (3) Phonon backscattering fraction, and (4) Thermal conductivity ratio. The three-dimensional nanomeshes have a neck size of 45 nm, a thickness of 60 nm, a y-pitch of 100 nm, and a varying *x*-pitch with an aspect ratio ranging from 0.5 to 10. The good agreement between the reproduced results and the results from the previous study validates both our ray tracing simulation and thermal conductivity model.

Table 2.1. Porosity correction factors $f(\phi)$ for each nanopore shape determined by ANSYS^{TM} [115]. The values are for porosity equals 25%, corresponding to the porosity used in ray tracing simulations.

Pore Shape	$f\,(\phi = 25\%)$
Circular	0.623
Hexagonal	0.554
Squared	0.577
Diamond	0.582
Triangular	0.543

2.4 Asymmetric Nanoporous Structures in Reducing Thermal Conductivity

In this section, we discuss transport mechanisms in Si nanoporous structures of varying pore shapes. We simulate squared, circular, triangular, hexagonal, and diamond pores with aligned distributions of the periodicity of 1 μm when the porosity is kept constant at 25%. We take all pore interfaces to be fully diffuse, which may underestimate the pore-shape-dependence, giving a lower bound of the thermal conductivity reduction. Experimentally, the specularity coefficient of the pore interface will depend on the surface quality during the fabrication process. Figure 2.3(a) shows the thermal conductivity predicted from 10 K to 1000 K, with a zoom-in box focusing around room temperature in the inset. While the neck size of porous structures is generally defined as the pitch (p) minus the diameter (d), i.e. $n = p - d$ [7,11–13] we are using the equivalent neck size for pores of varying shapes, which is still the smallest distance between nearest pores. The neck size defines the smallest phonon transport channel size in the direction of heat flow and is the key parameter in describing the thermal conductivity of nanoporous structures of varying pore shapes when the porosity is kept the same (Figure 2.3(a)). As expected, the thermal conductivity decreases as the neck size becomes smaller. Remarkably at 300 K, compared with bulk Si, we see thermal conductivity reductions between 25% and 50 %, depending on the pore shape. These results are consistent with recent studies in the literature [116] describing the phonon bottleneck effect and explaining thermal conductivity reductions by aligned and disordered circular pores. The effect of pore shape reduces with increasing temperatures because the Umklapp scattering starts to dominate, leading to diffusive phonon transport, as seen in Figure 2.3(c). Notice that even though the diamond and triangular pores have the same neck size, the triangular pores present a greater thermal conductivity reduction, which indicates that the neck size is not the sole mechanism driving the thermal conductivity reduction. We attribute the greater reduction when having

triangular pores to the increased heat flux localization. We solve the heat conduction equation for the heat flux distribution, $\boldsymbol{q}" = -k\nabla T$, by using finite-element-analysis method. As shown in Figure 2.3(b), the heat flux becomes extremely localized at the tip of triangular pores, hindering phonon transport; whereas such effect is less significant at the diamond pore tips. Hence, both neck size and pore shape play key roles in the thermal conductivity reduction in Si nanoporous structures.

While the precise calculation of Λ_b from Monte-Carlo ray tracing simulations enables the thermal conductivity predictions presented above, we can also estimate Λ_b following the idea of mean beam length (MBL). It is a geometric parameter widely used in radiation studies and has recently been employed to evaluate the thermal transport in nanoporous structures [90,91]. In 2D nanoporous structures, MBL is defined as $C\frac{A}{p}$, where A is the surface-area of the unit cell excluding the pores, p is the pore perimeter, and C is a fitting parameter extracted from ray tracing simulations. If we compute the MBL for each pore shape without including fitting parameter we will obtain 423 nm, 375 nm, 403 nm, 328 nm, and 375 nm, respectively for circular, squared, hexagonal, triangular, and diamonds nanopores. Notice that these values can capture the neck size dependence, but not the shape dependence. By comparing them with Λ_b extracted from the ray tracing method, we obtain the fitting parameter C for the above pore shapes as 3.8, 4.5, 3.5, 2.5, and 3.1. The value of 3.8 for circular pores agrees well with that of 3.4 found in the previous work [91]. Notice that MBL can work as a metric for comparing thermal transport in nanoporous structures with varying pore shapes, yet it requires comparison with ray tracing simulations to reflect the shape-dependency. Hence, despite the computational cost which can be reduced by program optimization, the Monte-Carlo ray tracing simulation is more accurate in modeling phonon transport due to its unique capability of precisely tracking individual particle trajectories,

which becomes especially imperative for studying thermal transport in complex nanoporous structures.

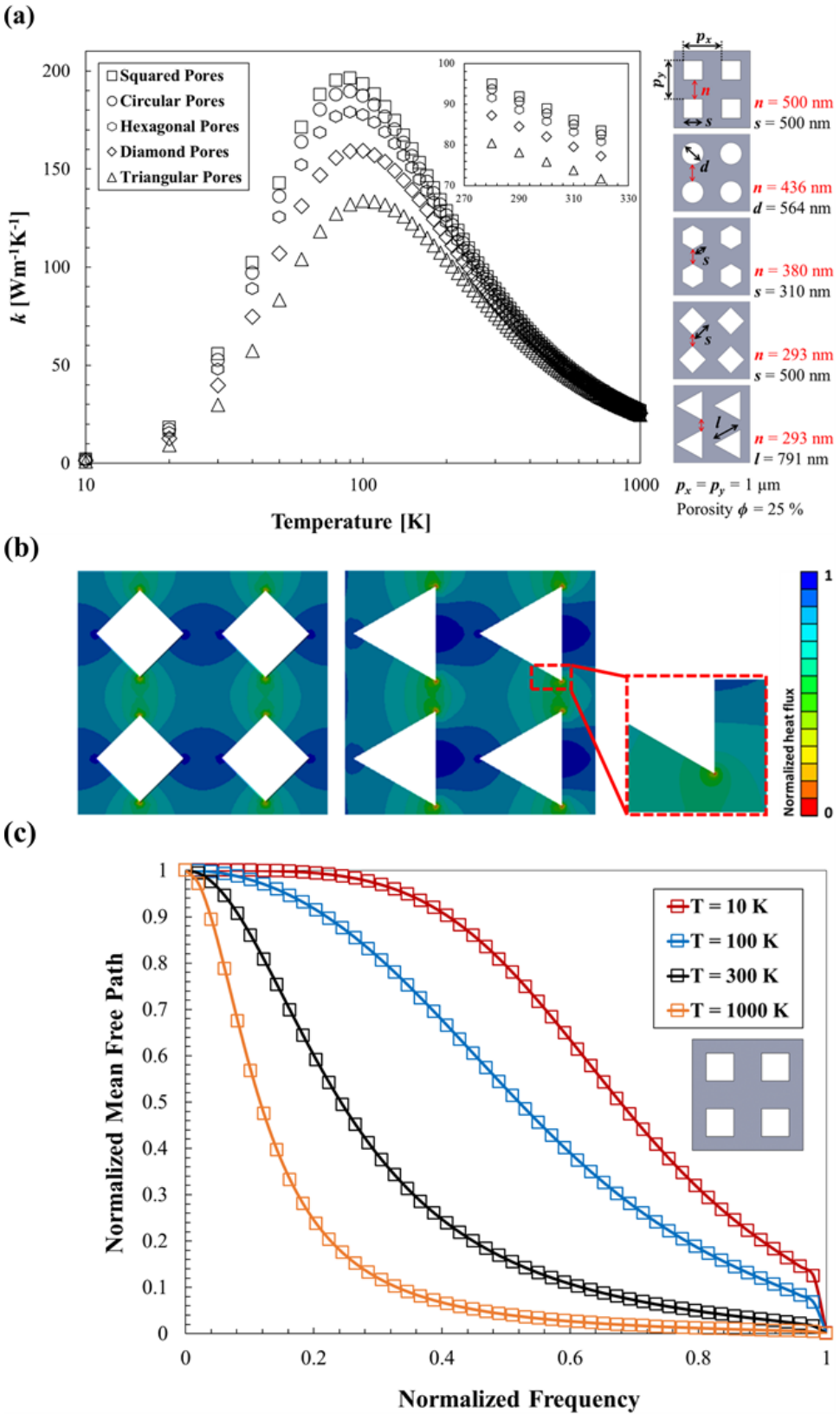
(a)
Squared Pores
Circular Pores
Hexagonal Pores
Diamond Pores
Triangular Pores
k [Wm-1K-1]
Temperature [K]
n = 500 nm
s = 500 nm
n = 436 nm
d = 564 nm
n = 380 nm
s = 310 nm
n = 293 nm
s = 500 nm
n = 293 nm
l = 791 nm
px = py = 1 μm
Porosity ϕ = 25 %
(b)
Normalized heat flux
(c)
T = 10 K
T = 100 K
T = 300 K
T = 1000 K
Normalized Mean Free Path
Normalized Frequency

Figure 2.3 Thermal transport in Si nanoporous structures of varying pore shapes. (a) Temperature-dependent thermal conductivity based on the calculations of Si nanoporous structures of pore shapes including squared, circular, hexagonal, diamond, and triangular from 10 K to 1000 K. The phonon boundary scattering mean free path is extracted from the ray tracing simulation and combined with other scattering mechanisms via Matthiessen's rule; the inset shows the data from 270 K to 330 K. The porosity is fixed at 25% and the periodicity is fixed at 1 μm, resulting in different neck sizes in nanoporous structures with different pore shapes. Notice that smaller neck size translates into greater thermal conductivity reductions. The temperature trend responds to the scattering mechanisms that dominate at different temperatures. (b) Finite-element-methods simulations of the heat flux distribution in diamond and triangular nanopores with the same neck size. The necks between adjacent rows of triangular pores present localized heat fluxes that are leading to a further reduction in the thermal conductivity. (c) Phonon mean free path as a function of frequency for the Si nanoporous structure with squared pores of aligned distribution at 10 K, 100 K, 300 K, and 1000 K. We consider the phonon-boundary, -impurity, and Umklapp scattering mechanisms. At high temperature, Umklapp scattering starts to dominate causing reduced phonon mean free path even at low frequencies, whereas at low temperature, phonon boundary scattering dominates and phonon mean free path plateaus at low frequencies.

2.5 Squared-lattice Pore Alignment vs. Hexagonal-lattice Pore Alignment

In this section, we investigate the effect of pore alignment by comparing squared-lattice aligned) to the hexagonal lattice (staggered) pore designs. Previous experimental work [14] of Si mesoporous structures showed similar thermal conductivities between aligned and staggered pore alignments at room temperature, but a recent study on 1D Si phononic crystals demonstrated nonnegligible differences between squared and triangular pore alignments at 4 K and room temperature [80]. In particular, the rotational symmetry between squared and diamond pores eliminates the pore shape dependence making them suitable for the pore alignment study. Changing the pore alignment from aligned to staggered, the neck size between squared pores reduces from 500 to 293 nm while that between diamond pores increases from 293 to 500 nm. For staggered pores, the neck size is defined as the smallest distance between the nearest pores perpendicular to the local heat flow direction, which is assumed diagonal to the global heat flow direction. For staggered diamond pores and aligned squared pores of the same neck size at 500 nm, the thermal conductivities are nearly identical (Figure 2.4(a)). Again, for aligned diamond

pores and staggered squared pores of the same neck size at 293 nm, the thermal conductivities are nearly identical (Figure 2.4(a)). These results show that the neck size is the key parameter in understanding thermal transport in nanoporous structures.

We further study circular nanoporous structures of squared-lattice and hexagonal-lattice pore alignments when having the same neck size varying from 100 to 800 nm and a fixed periodicity of 1 μm (see Table 2.2 for detailed dimensions). For circular pores, we define the neck size (n) as the smallest distance between nearest pores given by the pitch (p) minus the diameter (d), i.e., $n = p - d$, which is consistent with previous studies regarding nanoporous Si films of circular pores [7,11–13]. Results in Figure 2.4(b) show that the pore alignment greatly affects the thermal transport, especially at low temperatures where boundary scattering dominates. Particularly, the hexagonal-lattice pore alignment is more effective in reducing the thermal conductivity, which we attribute to the blocking of free paths in the direction of the heat flow. Recent work has utilized the line of sight (LOS) to interpret phonon propagation in nanobeam with slits [117]. The LOS is the direct path along which phonons can propagate from the heat source to the heat sink. Comparing the squared-lattice to the hexagonal-lattice pore alignment, the latter blocks the LOS paths between adjacent rows of pores, especially as the porosity goes higher. Shorter LOS leads to the shortened phonon mean free path, which effectively reduces the thermal conductivity. The thermal conductivity difference between two alignments becomes more evident for higher porosity structures. These results are consistent with recent studies in the literature [118], in which the low thermal conductivity of hexagonal lattice pores is attributed to the blocking of phonon pathways. In the inset of Figure 2.4(b), we show that at 300 K, in the limit of large neck sizes, boundary scattering is negligible as compared with Umklapp scattering as both thermal conductivities converge; in the limit of small neck sizes, boundary scattering becomes much more important and

results in different thermal conductivities. Moreover we notice that at 300 K, even with only around 3% porosity, nanoporous patterns can lead to a 30% lower thermal conductivity than bulk Si handbook value. These results highlight the importance of optimizing pore alignments in nanoporous structures for better thermoelectric performances.

Table 2.2 Dimensions of circular nanoporous structures of squared-lattice and hexagonal-lattice pore alignments.

Alignment	Neck Size $\boldsymbol{n}$ (nm)	Diameter $\boldsymbol{D}$ (nm)	Porosity $\boldsymbol{\phi}$
Squared-lattice	800	200	0.031
	200	800	0.503
Hexagonal-lattice	800	200	0.036
	200	800	0.580

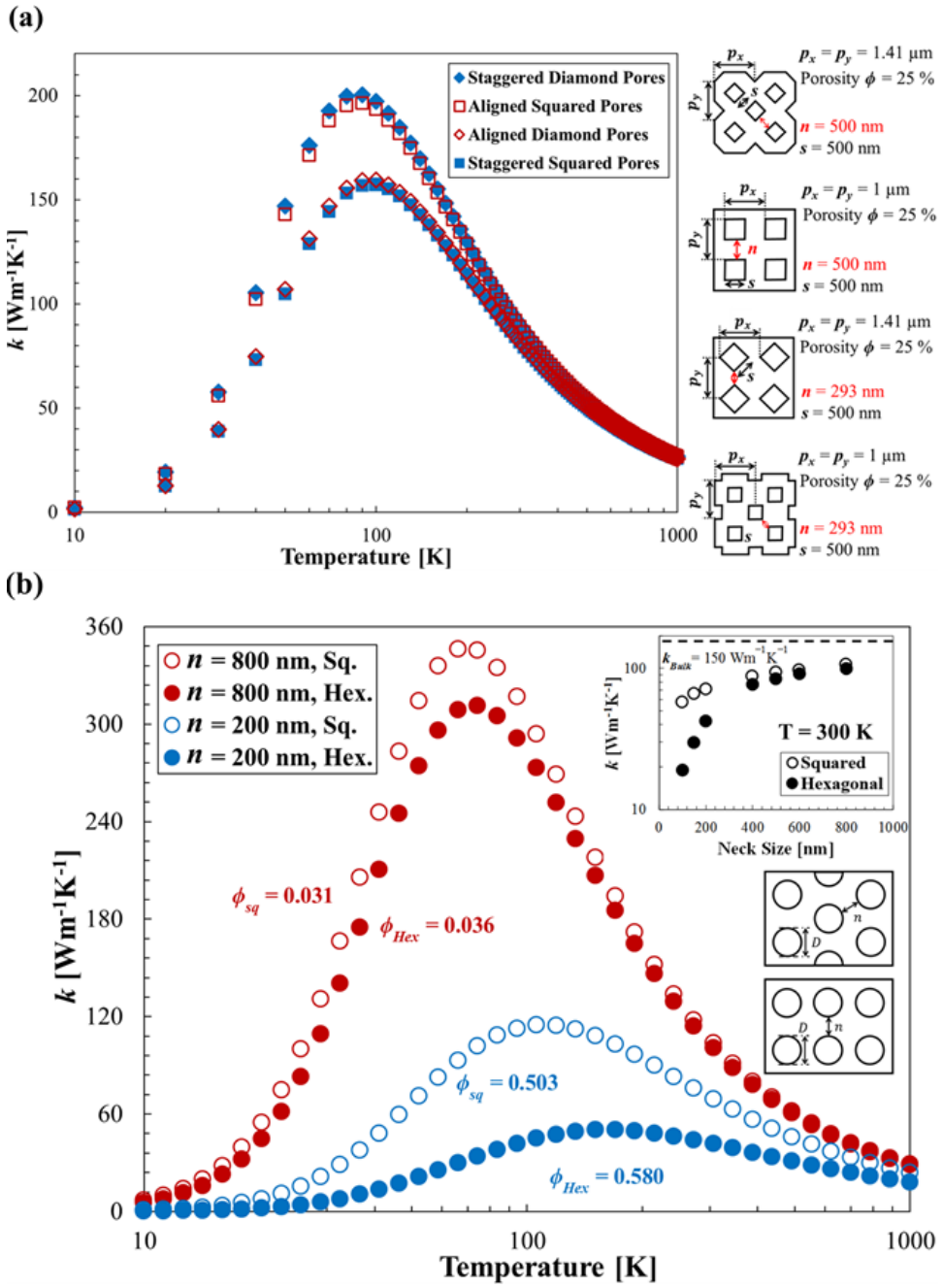

Figure 2.4 The effect of pore alignment on the thermal conductivity. (a) Thermal conductivities of nanoporous structures with squared and diamond pores of aligned and staggered pore alignments. The results show stronger neck-size dependency than pore shape and alignment dependencies, giving lower thermal conductivities when the neck size is 293 nm. (b) Thermal conductivities of circular nanoporous structures of the squared-lattice and hexagonal-lattice pore alignments with similar porosities. Both pore alignments have the same periodicity of 1 μm. The pore diameter and the neck size are kept the same when comparing. An evident disparity between thermal conductivities is observed in the low-temperature regime where ballistic phonon transport plays a key role. The impact of varying the pore alignment is stronger at higher porosities where the neck size becomes smaller.

2.6 Alternating Pore Size Distributions vs. Uniform Pore Size Distributions

Section 2.5 reveals the significance of shortening LOS paths by optimizing pore alignments in effectively reducing the thermal conductivity. In this section, we inspect the impact of varying pore size distributions. Starting with aligned homogeneous circular pores, we increase the diameter of pores in the even columns by $\sqrt{2}$ while reducing the number of pores by half to keep the porosity the same. We compare alternating to uniform pore size distributions, where the former separate smaller and larger pores on each side while the latter alternate them column by column. We compute thermal conductivities for these two pore size distributions from 10 K to 1000 K with fully diffuse pore interfaces when the porosity is kept the same. We study porosities of 0.1 and 0.3 and, as seen in Figure 2.5(a), in both cases, we see that nanoporous structure of alternating pore size distributions is more effective in reducing thermal conductivity than those of uniform pore size distributions and the difference between the two becomes more distinct at higher porosities. We attribute this effect to the increasingly complex boundary scattering phenomena by alternating from large to small neck sizes and obstructed LOS for phonon propagation. We also present in Figure 2.5(b) the distribution of total heat fluxes obtained by FEM simulations, which shows greater heat localization between small pores in alternating pore size distributions that may constraint the phonon transport. From the LOS point of view, the uniform pore size distributions show longitudinal free paths while the alternating pore size distributions completely block these pathways. This is easily seen in Figure 2.5(b), where no connected LOS path appears in the alternating pore size distributions, which is indicative of a more impeded phonon propagation. These findings further validate the relative contributions of limiting LOS in the thermal conductivity reductions and more complex phonon boundary scattering due to alternating the pore size and the neck size.

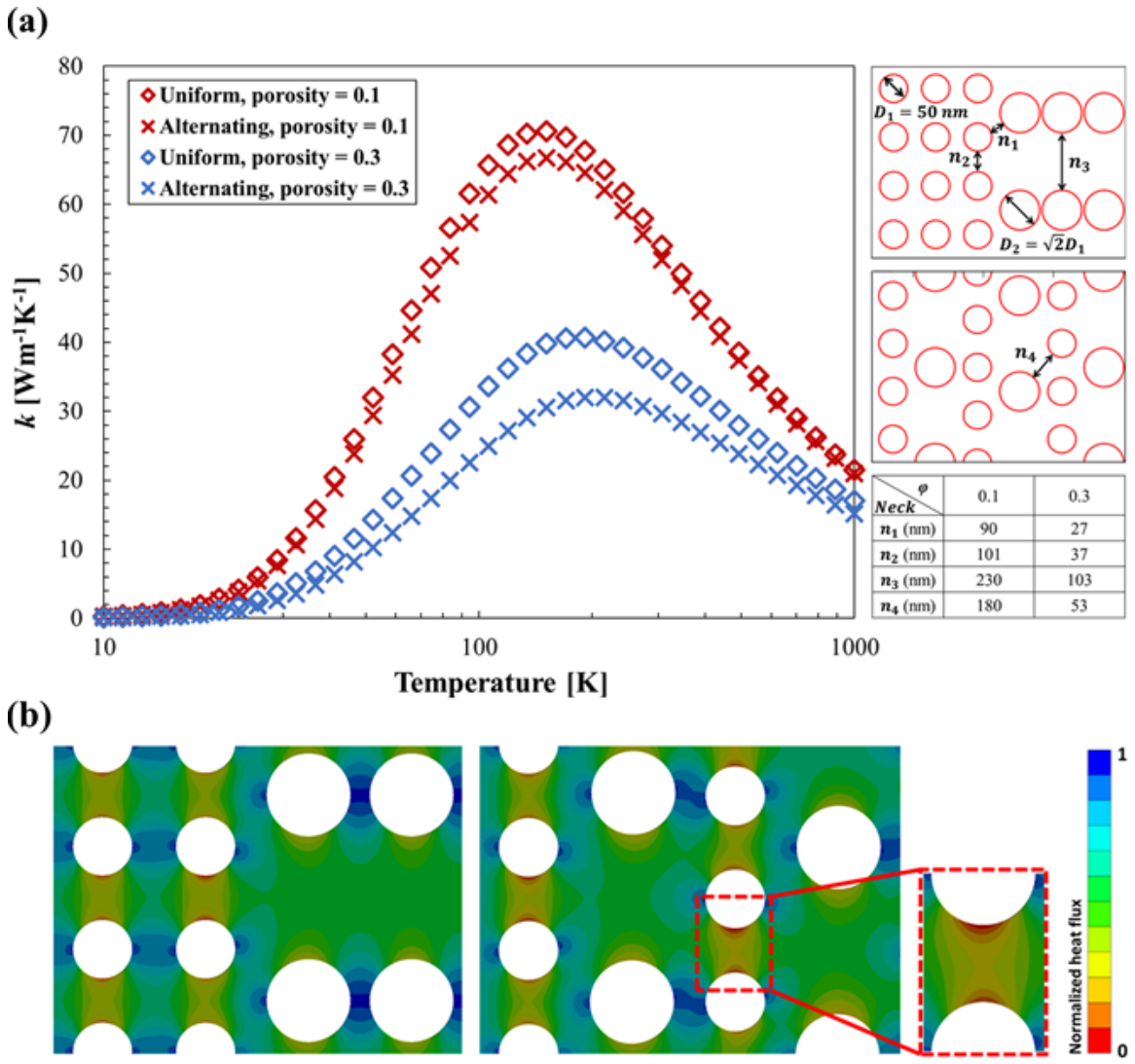

Neck \ φ	0.1	0.3
n_1 (nm)	90	27
n_2 (nm)	101	37
n_3 (nm)	230	103
n_4 (nm)	180	53

Figure 2.5 The effects of pore size distributions on the thermal conductivity. (a) The thermal conductivity for nanoporous structures of alternating and uniform pore size distributions as a function of temperature for porosities of 0.1 and 0.3. The former is more effective in reducing the thermal conductivity due to blocked LOS and more complex phonon boundary scattering by alternating pore sizes and neck sizes. (b) FEM simulations of total heat flux distribution in nanoporous structures of alternating and uniform pore size distributions. Notice the greater heat flux localization between small pores when a big pore blocks the LOS of the adjacent neck. The shortened LOS drives phonons through more complex paths which may result in exaggerated phonon backscattering.

2.7 Conclusions

We use a ray tracing technique to explain phonon boundary scattering phenomena in Si nanoporous structures of varying pore shapes, pore alignments, and pore size distributions over a wide range of temperatures. We find that the neck size is the key parameter determining the thermal conductivity when the porosity is kept the same. However, with the same neck size and porosity, asymmetric pore shapes such as triangular pores will achieve lower thermal conductivity than symmetric pore shapes. For symmetric nanopores, a hexagonal-lattice pore alignment is more effective in reducing the thermal conductivity than a squared-lattice pore arrangement and alternating distributions of large and small pores are more effective in reducing the thermal conductivity than nanopores with uniform size distributions due to the limited line of sight for phonons and localized heat fluxes. The key factors that govern phonon boundary scattering identified in this work provide new insights into understanding the fundamental mechanisms of thermal transport in complex nanoporous structures. These findings will enable optimal designs of artificial nanostructures for thermoelectric energy harvesting and solid-state cooling systems.

CHAPTER 3: REALIZING THERMAL RECTIFICATION USING ASYMMETRIC NANOPOROUS STRUCTURES

Thermal rectification is a phenomenon where heat prefers flowing in one direction than another, which could open opportunities for directional thermal management. This work investigates the possibilities of realizing thermal rectification using asymmetric Si nanoporous structures even with surface boundaries being fully diffuse. Using the ray tracing technique discussed in Chapter 2, we optimize the placement of triangular pores and obtain strikingly different thermal conductivity in the forward and reverse direction. The optimal arrangements of triangular pores show a rectification up to 13 when the phonon injection angle is optimally controlled. The significant rectification ratio is attributed to different ballistic phonon-boundary scattering events induced by the geometrical asymmetry. The design principle is readily extendable to other materials, other than Si considered here if the phonon mean free path is larger than the critical distance in the designed asymmetric structures.

3.1 Introduction

Thermal rectification is a phenomenon where heat prefers flowing in one direction than another, which has potential applications in directional thermal management [119–121] and phononic information [122]. Several mechanisms [123–133] have been studied to induce thermal rectification. Asymmetric pristine and defect-engineered monolayer graphene nanostructures have been reported experimentally to achieve thermal rectification of 10% and 26%. A thermal rectification ratio up to 8.3% ± 0.5% has been demonstrated experimentally using Y-junction carbon nanotube bundles at a temperature difference of 4 K. Recent work reported a very large thermal rectification up to 5×10^4% in ferromagnetic insulator-based superconducting tunnel junctions based on the combination of spin splitting and spin filtering, which leads to self-amplification of the electronic heat diode effect due to breaking of the electron-hole symmetry.

Asymmetric nanoporous structures [130,134,135] showed the potential of realizing thermal rectification, but the experimental and theoretical evidence is still limited. One study found no significant thermal rectification in phononic crystals with Pacman-shaped holes at room temperature and only signature of thermal rectification at a cryogenic temperature of 4.2 K within the instrumental uncertainty.

3.2 Results and Discussion

Here we demonstrate triangular nanopores can induce thermal rectification by incorporating a phononic collimator and assuming ballistic phonon transport at the low temperature. From the Landauer formalism, we model a thermal rectifier between two blackbody-like [134] reservoirs from which phonons are emitted. Miller et al. emphasized the importance of the phonon emission distortion to inducing the thermal rectification, which is fulfilled in this work by a phononic collimator that can manipulate the phonon injection direction [134]. Our ray tracing simulations construct a single unit cell with specular boundary conditions at the top and bottom surfaces and periodic boundary conditions at the left and right surfaces to periodically repeat itself to tile the entire geometry. Assuming the use of imaginary collimators [132], we fix the injection angles of phonons entering the unit cell when the ray tracing begins. Before the simulation terminates, a phonon exiting the unit cell form either left or right boundary will re-enter from the opposite boundary and its injection angle will depend on its previous collision event. Our thermal conductivity calculations use the Matthiessen's rule to obtain the total mean free path of phonons in nanoporous structures, in which the mean free path limited by phonon-boundary scattering is obtained through ray tracing simulations and the mean free path limited by Umklapp and phonon-impurity scattering are obtained by $\Lambda_{imp}(\omega) = v_g(\omega)\tau_{imp}(\omega)$ and $\Lambda_U(\omega) = v_g(\omega)\tau_U(\omega)$, where v_g is the phonon group velocity, $\tau_{imp}(\omega)$ and $\tau_U(\omega)$ are relaxation times detailed in Chapter 2.

We define the rectification ratio as $R = \frac{k_{fwd} - k_{rev}}{k_{rev}}$, where k_{fwd} and k_{rev} denote thermal conductivities in the forward (hot to cold) and reverse directions; hence, we need to enhance k_{fwd} while limiting k_{rev}. As shown in Fig. 3.1.1, we place isosceles triangle with a base length of 80 nm and base angles θ_1 (θ_1-triangles) and θ_2 (θ_2-triangles) in adjacent columns. We set the base sides of the triangles to be fully diffuse ($p_B = 0$), which corresponds to the worst case-scenario thermal rectification because it increases the phonon transmission in the reverse direction ($\mathcal{T}_{rev}$) even though no gap exists between adjacent rows. Notice that if we set the legs of the triangles as specular ($p_L = 1$), a staggered pore alignment with $\theta_2 = 2\theta_1 - \frac{\pi}{2}$ and $g_L = \frac{B}{2}\tan\theta_2$ will enhance the phonon transmission in the forward direction ($\mathcal{T}_{fwd}$) by letting phonon reflected by θ_1-triangles pass through the spaces between θ_2-triangles without touching them. Ballistic phonon transport will not be violated because the average phonon mean free path is larger than distances between neighboring triangles. To find an optimal design, we examine the thermal rectification when the phonons are injected in the direction of the heat flow (90°) in the nanoporous structure at 100 K by fixing $\theta_1 = 60°$ and varying θ_2. Fig. 3(b) shows the rectification ratio R when $p_L = 0, 0.8$, and 1. For diffuse boundaries, we find a non-impressive R plateauing as θ_2 increases until $50°$ and then starting to drop, reaching nearly 0 at $80°$. This reduction is due to the increased phonon backscattering caused by the diffuse legs of θ_2-triangles which deteriorates k_{fwd} and reduces R. If we assume specular triangle legs ($p_L = 1$), we notice extremely low values of R at specific geometries resulted from phonon trajectories perpendicular to triangle legs. For other θ_2, rectification ratios are greatly enhanced. Particularly, the highest R is achieved at $70°$ since both θ_1- and θ_2-triangles will reflect phonons forwardly, while the specular legs of the θ_2-triangles are not long enough to induce phonon backscattering. Since a perfectly specular surface is not possible in nanofabrication, we compute R with $p_L = 0.8$. In this case, θ_2 of $30°$ achieves the best design

with an improved $\mathcal{T}_{fwd}$ yielding greater R than those of $p_L = 1$, which validates the effectiveness of the proposed θ_1, θ_1, and g_L relations ($\theta_2 = 2\theta_1 - \frac{\pi}{2}$ and $g_L = \frac{B}{2}\tan\theta_2$). We extend the proposed design with fully diffuse boundaries and different θ_1. Besides studying the rectification when the phonons are injected at 90°, we also study the effect of using the optimal phonon injection angles which give the highest $\mathcal{T}_{fwd}$ and are detailed in TABLE II. Using these optimal injection angles in the forward direction while keeping a 90° injection angle in the reverse direction, we find significantly boosted rectification ratios. We can achieve the highest R of 13 when having $\theta_1 = 50°$ and $\theta_2 = 70$. We have further studied the reverse-direction phonon transmissions as a function of injection angle and find that there can be special injection angles providing minimum transmissions depending on the pore arrangement. For the presented triangular pores, the reverse-direction injection angles around 16°, 90°, and 174° give the lowest transmissions, and the differences are considered negligible. Our simulations results are based on the reverse-direction injection angle of 90°, which is generally assumed to provide lowest phonon transmissions for various pore arrangements, due to phonon scattering mostly perpendicular to the backside of triangular pores. Our results imply that optimizing the phonon injection angle using a collimator will enable significant thermal rectification in nanoporous structures.

TABLE 3.1.1. Optimal phonon injection angles that maximize the phonon transmission in the forward direction of heat flow for different triangular pore designs (θ_1 - θ_2).

Thermal Rectifier Design	Optimal Phonon Injection Angle [º]
50 º - 10 º	26
55 º - 20 º	32
60 º - 30 º	42
65 º - 40 º	50
70 º - 50 º	58
75 º - 60 º	66
80 º - 70 º	74
85 º - 80 º	82

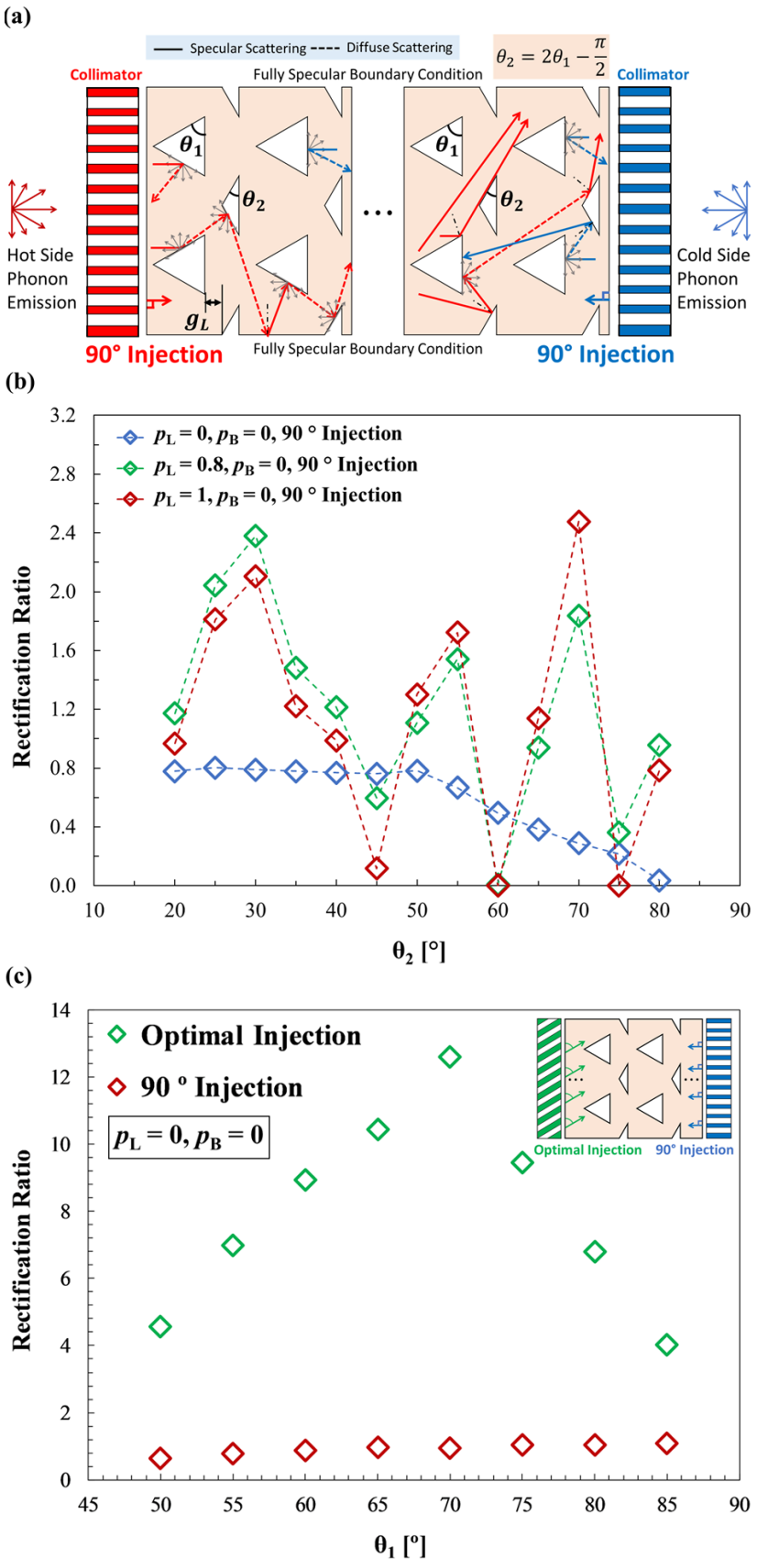
(a)
Specular Scattering
Diffuse Scattering
$\theta_2 = 2\theta_1 - \frac{\pi}{2}$
Collimator
Fully Specular Boundary Condition
Collimator
θ_1
θ_2
Hot Side Phonon Emission
g_L
Cold Side Phonon Emission
90° Injection
Fully Specular Boundary Condition
90° Injection
(b)
$p_L = 0, p_B = 0$, 90 ° Injection
$p_L = 0.8, p_B = 0$, 90 ° Injection
$p_L = 1, p_B = 0$, 90 ° Injection
Rectification Ratio
θ_2 [°]
(c)
Optimal Injection
90 ° Injection
$p_L = 0, p_B = 0$
Optimal Injection
90° Injection
Rectification Ratio
θ_1 [°]

Figure 3.1 (a) Schematics of thermal rectifier consisting of staggered triangular nanopores with a base length of 80 nm, gap of zero between the rows, and base angles θ_1 and θ_2. The phonons at the hot and the cold sides are injected through the phononic collimators. (b) Rectification ratio as a function of θ_2 when θ_1 is fixed at 60° and phonons are injected at 90° for triangle legs specularities of 0, 0.8, and 1. The best design with a realistic specularity of 0.8 is realized when $\theta_2 = 30°$ which corresponds to $\theta_2 = 2\theta_1-\pi/2$. (c) Rectification ratio as a function of θ_1 when θ_2 follows the relationship $\theta_2 = 2\theta_1-\pi/2$ with all surface boundaries set to fully diffuse. Injecting the phonons in an optimal angle dramatically increases the rectification of the nanoporous structures up to 13 with a θ_1 of 50° and a θ_2 of 70°.

3.3 Further Discussions

We chose 90° as the injection angle in the reverse direction based on the intuition that phonons directed perpendicular to the backsides of triangles would be scattered right back. In response to the reviewer's comment, here we have run ray tracing simulations as a function of the injection angle from 0° to 180° in the reverse direction as shown below. The simulation considers all diffuse boundaries and θ_1 fixed at 60° and we varied θ_2 from 30° to 45°. Figure 3.2 (a) shows the phonon transmission can be minimized by multiple conditions depending on the specific pore arrangement. As expected, the wide range of angles near 90° show very low transmissions (0.3 %~0.5 % from 80° to 120°). It is interesting to note that there are two other transmission dips at the injection angles of approximately 16° and 174°. These special conditions are due to the unique pore arrangement and the geometric details can be explained in Figure 3.2 (b) and (c). For thermal rectifiers with various geometries, a 90° injection angle in the reverse direction would generally lead to minimal phonon transmissions, while there would be other special injection angles giving transmission dips depending on the pore arrangement. Since phonon transmissions corresponding to these injection angles are very small, changing phonon injection angle from 90°to those geometry-dependent injection angles would not vary the rectification ratio significantly.

(a)

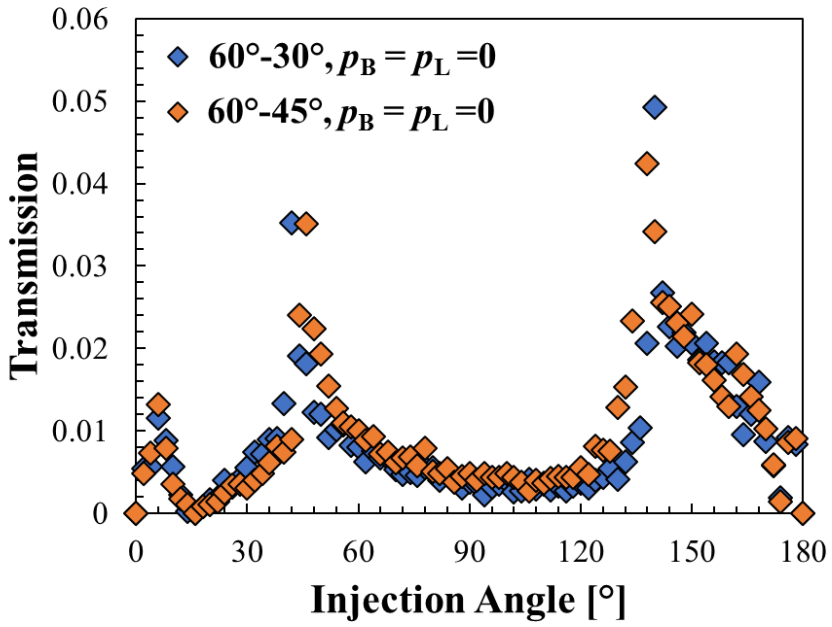
0.06
0.05
0.04
0.03
0.02
0.01
0
Transmission
60°-30°, $p_B = p_L = 0$
60°-45°, $p_B = p_L = 0$
0
30
60
90
120
150
180
Injection Angle [°]

(b)

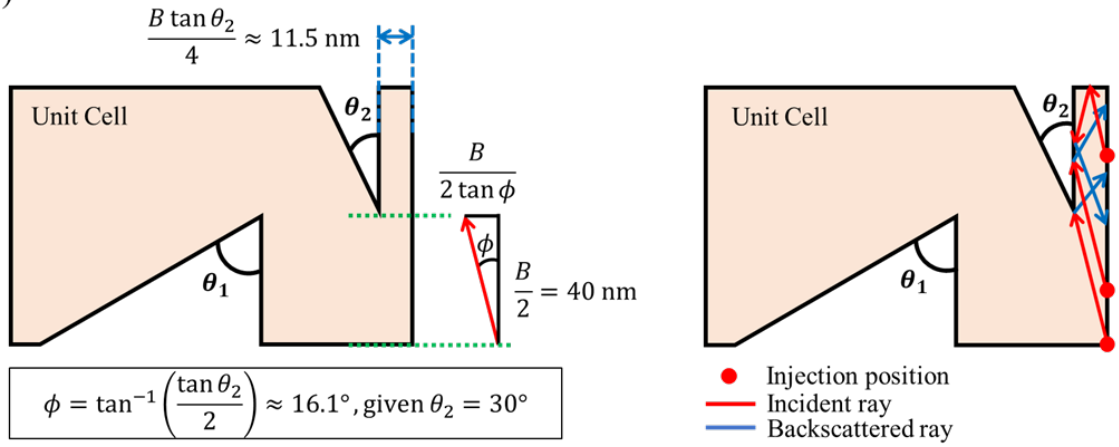
$\frac{B \tan\theta_2}{4} \approx 11.5$ nm
Unit Cell
θ_2
$\frac{B}{2\tan\phi}$
ϕ
$\frac{B}{2} = 40$ nm
θ_1
$\phi = \tan^{-1}\left(\frac{\tan\theta_2}{2}\right) \approx 16.1°$, given $\theta_2 = 30°$
Unit Cell
θ_2
θ_1
Injection position
Incident ray
Backscattered ray

(c)

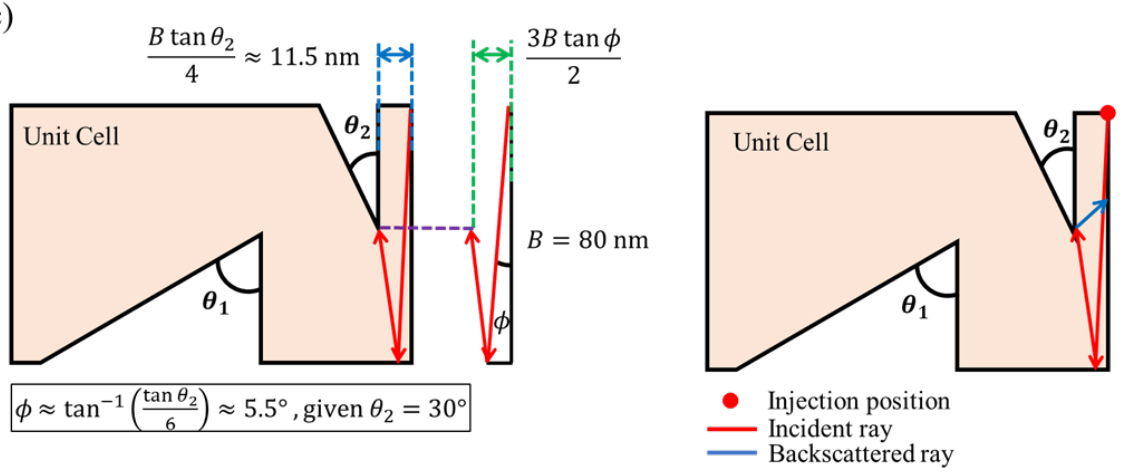
$\frac{B \tan\theta_2}{4} \approx 11.5$ nm
$\frac{3B \tan\phi}{2}$
Unit Cell
θ_2
$B = 80$ nm
θ_1
ϕ
$\phi \approx \tan^{-1}\left(\frac{\tan\theta_2}{6}\right) \approx 5.5°$, given $\theta_2 = 30°$
Unit Cell
θ_2
θ_1
Injection position
Incident ray
Backscattered ray

Figure 3.2 (a) Phonon transmission coefficient as a function of the phonon injection angle for two thermal rectifier geometries. All the boundaries are fully diffuse. (b) Schematics and representative phonon paths for the injection angle of 16°. (c) Schematics and representative phonon paths for the injection angle of 174°.

For symmetric geometries such as aligned circular pores, the phonon transmission follows the same injection angle dependency for the forward and reverse heat flow directions, as shown in Figure 3.3. We simulated 10 layers of circular pores with the specularity of pore interfaces p_C being 0 and 0.8. We choose these two specularity values to explore any potential influences from surface roughness, namely fully diffuse and partially specular surfaces. Instead of calculating the thermal conductivity, the phonon transmission is enough to demonstrate the identical phonon transport dependency on the injection angle in both heat flow directions regardless of the specularity when we have symmetric geometries. We can see a peak at 90° due to the horizontal free path for phonons between circular pores in adjacent rows directly going from the hot to the cold reservoir. This indicates that injecting phonons randomly (between 0 and 180°) or using the same injection angle for both heat flow directions will not induce any thermal rectification. Some sorts of asymmetry are always needed. Therefore, by simply having two injection angles that lead to different phonon transmissions in the forward and reverse heat flow directions, the thermal rectification could be achieved.

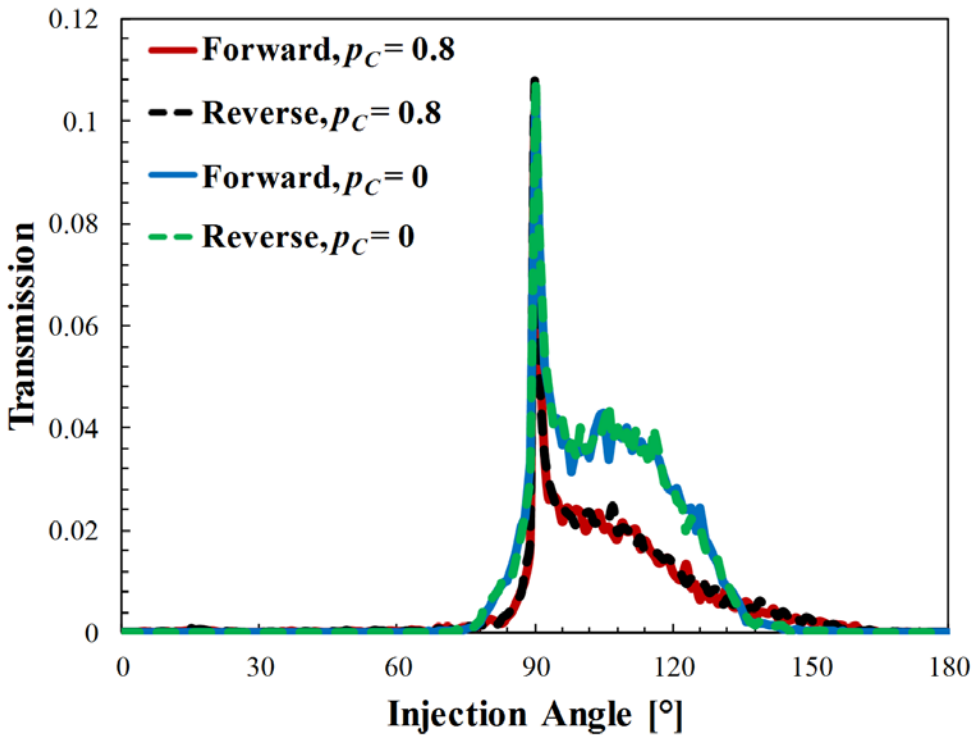

Figure 3.3 Phonon transmission coefficient as a function of the phonon injection angle for aligned distributed circular pores. Due to the geometric symmetry, the phonon transmissions in the forward and reverse heat flow directions collapse into the same curve (small discrepancies are due to numerical uncertainties arising from a limited number of phonons launched for each injection angle to lessen computational loads).

3.4 Conclusions

In this work, we use a ray tracing technique to investigate the potential thermal rectification phenomenon in Si nanoporous structures. Our simulation results show the possibilities of realizing thermal rectification using asymmetric nanopores, where optimal arrangements of triangular pores achieve a thermal rectification ratio up to 13 even for fully diffuse surface boundaries when the phonon injection angles are optimally controlled by an imaginary collimator. These findings will guide future optimal designs of the nanoporous structure-based thermal rectification system.

CHAPTER 4: PHONONIC TOPOLOGICAL INSULATORS BASED ON SIX-PETAL HOLEY SILICON STRUCTURES

Since the discovery of the Quantum Spin Hall Effect, electronic and photonic topological insulators have made substantial progress, but the phononic analog in solids has received relatively little attention due to challenges in realizing topological states without the spin-like degree of freedom and with transverse phonon polarizations. Here we present a holey Si-based topological insulator design, in which simple geometric control enables topologically protected in-plane elastic wave propagation up to GHz ranges with a submicron periodicity. By integrating a hexagonal lattice of six small holes with one central hole and by creating a hexagonal lattice by themselves, our design induces zone folding to form a double Dirac cone. Based on the hole dimensions, breaking the discrete translational symmetry allows the six-petal holey Si to achieve the topological phase transition, yielding two topologically distinct phononic crystals. Our numerical simulations confirm inverted band structures and demonstrate backscattering-immune elastic wave transmission through defects including a cavity, a disorder, and sharp bends. Our design also offers robustness against geometric errors and potential fabrication issues, which shows up to 90% transmission of elastic waves even with 6% under-sized or 11% over-sized holes.

4.1 Introduction

The concept of topology [31,136], or conserved properties under continuous deformation, has attracted much interest in recent years of condensed matter physics since the discoveries of the Quantum Hall effect and Quantum Spin Hall effect [50–52]. The topological states have been first studied in electronic systems, and topological insulators are characterized by unique attributes of insulating bulk bands and conducting edge bands. These conducting bands are robust and protected by non-trivial topological states to support unidirectional propagation at the boundary with no backscattering even in the presence of defects, offering unmatched tolerance and unprecedented

transport capabilities. While most of the interest and efforts have been in topological electronics [31,136], and photonics [40,137] due to the intrinsic spinning nature of the particles and the ease of breaking the time-reversal symmetry by the external magnetic field. Topological insulators based on bosonic systems have not been explored as much because of the lack of spin-like states. Moreover, the low group velocity, high density of states, and significantly dissimilar acoustic impedance between common materials induce backscattering, resulting in difficulties in achieving defect-immune wave propagations. Recently, investigations of topological insulators in mechanical [53,138], acoustic [44,139–141], and elastic [63,142–148] systems have shown promising progress in tackling the challenges. The breaking of time-reversal symmetry was done by circulating fluid flow in the background [44,46], external optomechanical excitation [149], and periodically arranged local resonators [143]. Most success made on phononic systems has targeted on realizing symmetry protected edge states for acoustic waves possessing only one longitudinal polarization. Realizing helical edge states in elastic waves remains outstandingly challenging because its three available polarizations (one longitudinal and two transverse) can easily be mixed at most solid interfaces precluding the formation of two degenerate states characterized by Dirac dispersions [64,150]. And most passive elastic materials generally conserve time-reversal symmetry, further impeding the fulfillment of chiral edge states in elastic systems [64,150,151]. Recent studies overcame these problems by utilizing chiral interlayer coupling to break the inversion symmetry [140] or by emulating the Quantum Valley Hall effect to support edge states in artificially engineered elastic structures. The latter concept allows reduced geometrical complexities and can be extended to photonic [152], acoustic [153], and elastic systems [154]. The elastic analog of the Quantum Valley Hall effect [154], has been numerically demonstrated by periodic structures with edge states within the bulk band gaps. Similar to the acoustic topological

system realized by a double Dirac cone [54], a recent theoretical study has demonstrated an elastic topological system with a double Dirac-cone by using subwavelength meta-structures [64]. Two recent studies demonstrated a snowflake porous structure to topologically guide the elastic wave at GHz ranges making it favorable for applications of phononic circuits [142,155]. Other studies show the possibility of realizing topological insulator by using perforated holes to enable elastic pseudospin transport [63] and spiral-shaped pores to guide the flexural waves [156]. While there have been notable achievements in theoretical ends, there have been limited studies for elastic topological insulators especially in phonon frequency regimes of GHz and beyond and using a platform of silicon, which offers significant compatibility to semiconductor devices and fabrication feasibility. In this paper, we develop a novel design of elastic wave topological insulator based on six-petal holey silicon nanostructures that support topologically protected wave propagation at frequencies up to GHz ranges when the unit cell periodicity reaches submicron scales even in the presence of geometric defects and potential fabrication issues. The circular pore shape provides higher tolerance to rounding effect in fabrication processes, making it competitive and desirable for the application of monolithic phononic circuits for information processing. The design also offers scalability from low- to high-frequency based on the periodicity, yielding the smallest neck size of ~20 nm in our current simulations and has been experimentally achieved in previous holey silicon nanostructure for thermal characterization [12], opening up possibilities of feasible fabrication and experimental exploration.

4.2 Methodology

Throughout this paper, the numerical simulations are performed by using the commercial Finite Element Analysis software COMSOL Multiphysics. The phononic band structure of unit cells is computed using the eigenfrequency study in the solid mechanics module. The Bloch

periodic boundary conditions are imposed on the boundaries of the unit cell. The backscattering-immune elastic wave transmissions are computed by using the frequency-domain study in the solid mechanics module. Low-reflection boundary conditions are imposed on the boundaries of the simulation domain to avoid undesired elastic wave leakage.

Refer to Appendices 3 for details of calculating band structures in COMSOL Multiphysics.

4.3 Design of Six-petal Holey Si Topological Insulators

4.3.1 Designing Parameters

The designed structure is a planar quasi-two-dimensional phononic crystal with a hexagonal lattice of vacuum six-petal-shaped pores perforated in a silicon slab [Fig. 4.1(a), left]. Each pore consists of a larger circle in the center surrounded equidistantly by six smaller circles [Fig. 4.1(a), right]. The radii of the central and corner circles are r_i and r_o, respectively, and their center-to-center distance d_{io} follows $d_{io} < r_i + r_o$. Previous studies on snowflake-hole-based phononic waveguides had reported the edge-rounding effect and sizing errors in the fabrication process [157,158]. The rounding of sharp corners may dramatically change the mechanical response leading to discrepancies between numerical simulations and experimental data [159]. Our design of six-petal pore significantly mitigates the negative effect of such fabrication imperfection by incorporating circles as the building block. Porous structures with circular features have been widely employed in various photonic and electronic systems. While noncircular or nonconventional geometries may provide better topological properties when fabrication inaccuracy is precisely controlled, our six-petal design offers excellent solutions against a wide range of uncertainties and high transmission via robust optimization, which is a unique approach fundamentally different from deterministic optimization. Our design opens up new pathways of achieving phononic topological insulators based on conventional platform having circular holes.

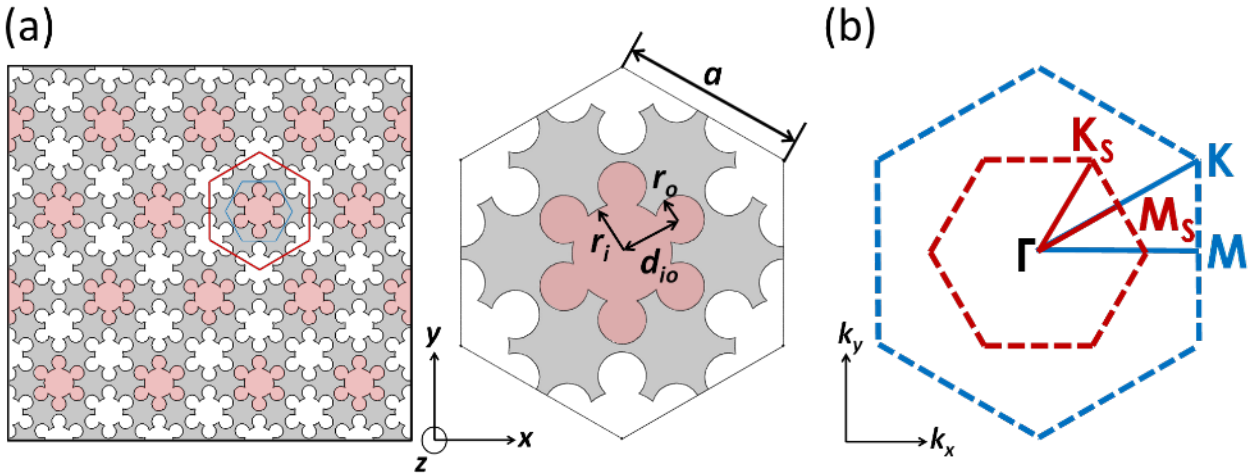

Figure 4.1 (a) Left: Schematics of the six-petal holey silicon in a hexagonal lattice. Right: The original unit cell containing a single six-petal pore (light-red filled) and the enlarged unit cell (gray filled) with the original one surrounded by one-third of each its six neighboring pores in real space. Each six-petal pore is defined by dimensional parameters ($\boldsymbol{r_i}$, $\boldsymbol{r_o}$, $\boldsymbol{d_{io}}$). The thickness of the film is kept at 100 nm and the periodicity $\boldsymbol{a}$ is 866 nm. The close and open of the bandgap is realized by manipulating $\boldsymbol{r_o}$ and $\boldsymbol{d_{io}}$, namely, modifying $\boldsymbol{\Delta r_o}$ and $\boldsymbol{\Delta d_{io}}$. When $\boldsymbol{\Delta r_o}$ and $\boldsymbol{\Delta d_{io}}$ are zeros, the original hexagonal lattice has a discrete translational symmetry and we expect a double Dirac cone in the dispersion curve. When they are not zeros, the translational symmetry will be broken, and we expect the double Dirac cone to be replaced by band gaps in the dispersion curves. (b) Schematic of the first Brillouin zone for the original and enlarged unit cells in reciprocal space. The symmetry line for the original unit cell is Γ-M-K-Γ whereas the folded symmetry line for the enlarged unit cell is Γ-M_S-K_S- Γ.

4.3.2 Comparison with the Design in the Literature

The snowflake crystal structures, which have been realized experimentally for the photonic topological insulators, have also been turned into a phononic topological insulator by geometrical modifications. The structure consists of three concentric rectangular strips with a length 2$\boldsymbol{r}$ and a width $\boldsymbol{w}$ that rotate 60° apart between every two neighbors. Triangular-lattice arrangement of snowflake phononic holes form a phononic crystal that exhibits D_{6h} symmetry, which is a six-fold rotational symmetry with in-plane and out-of-plane reflections). The phononic crystal possesses Dirac cones at high-symmetry points K and K' in the reciprocal space and by changing $\boldsymbol{r}$ of every third snowflake results in the breaking of the original translational symmetry. While, at first

glance, our six-petal holey structure shares some similarities with the snowflake structure, there are novel aspects to be pointed out. In particular, the holey design based on circular features compared to the snowflake design based on noncircular features holds significant values. Our work implies that elastic topological insulators that do not have to have noncircular features or nonconventional geometries, and this opens up possibilities of developing topological insulator devices on conventional platforms; similar hole patterns exist in various photonic and electronic systems. Another important aspect we would point out is that our study addresses a fundamentally different optimization procedure; the six-petal holey structure provides the best solution against uncertainty via robust optimization, as opposed to deterministic optimization. Due to this novel approach, the six-petal holey structure offers robustness as topological insulators against wide ranges of geometric variations, which have not been offered or explored by previous studies yet.

To further support the above claims, we compare the topological properties of the six-petal holey structure and the snowflake structure in the same geometric scale. Figure 4.2 shows that if the snowflake structure of periodicity of 500 nm is under-sized by 2%, which is simulated by multiplying the snowflake arm length $\boldsymbol{r}$ by and width $\boldsymbol{w}$ by 0.98 and applying the identical periodic boundary conditions, the frequency of the double Dirac cone (red line, Figure 4.2(b)) shifts below the lower edge of the bandgap (marked by the light-purple box); the topologically protected edge states cannot form anymore. While the snowflake structure is unable to resist even 2% under-sizing, our six-petal holey structure can maintain matched bandgaps and double Dirac cone even when the under-sizing reaches 2% (Figure 4.2 (d)-(f), where the double Dirac cone sits inside the overlapped bandgaps).

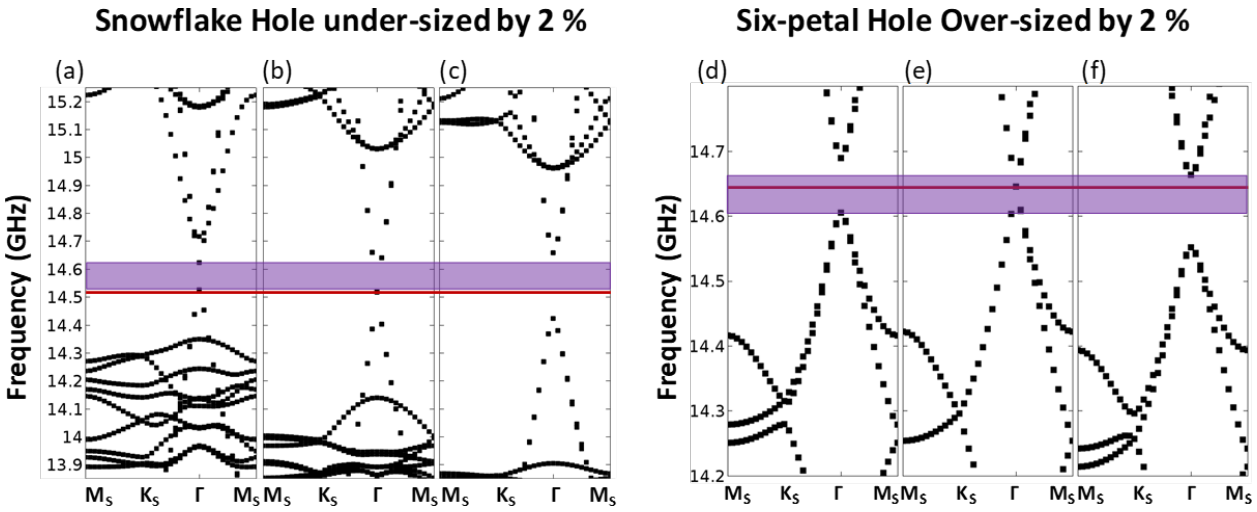

Figure 4.2 (a) – (c) The band structure of the snowflake structure with a periodicity of 500 nm suffering to 2 % under-sizing. Comparing the frequency of the double Dirac cone with the frequency ranges of bandgaps, we can see the double (b) Dirac cone is already below the lower bound of the bandgap of the structure with a snowflake radius of 156.8 nm, which is given by multiplying the width 160 nm by 0.98. This fails to achieve topologically protected edge states inside an insulating bulk bandgap. Therefore, the topological properties are not supported when the snowflake structure is under-sized even by 2 %. (d) – (f) The band structure of the six-petal holey structure of the same geometric scale with the periodicity of 500 nm and with 2 % under-sizing. The double Dirac cone locates within the overlapped bandgaps, indicating topologically protected edge states exist due to the design robustness.

Another key benefit our six-petal holey structure provides is the robustness to the rounding effect that is commonly seen in the micro/nanofabrication process. Such rounding effects can pose serious limitations on theoretical designs in practice, and the rounded corners of the snowflake arms may significantly degrade topological properties. To support this claim, we have tested simulations of the snowflake structure using the periodicity of 5000 nm and the dimensions described in the previous work. The schematics of the snowflake structures with snowflake ***r*** of 1600 nm (left), 1800 nm (middle), and 2000 nm (right) together with the rounding from 0 to 350 nm (0 to 50% of the snowflake ***w***) are depicted below each band structure plot, as shown in Figure 4.3. By adding 50 nm (7% of the snowflake ***w***) rounding to the sharp corners at the end of rectangular strips, we can observe an extra band falling under the upper edge of the bandgap which

makes it incomplete. As we increase the rounding further, we can see not only the existence of extra band inside the bandgap but also the shifting of the double Dirac cone and mismatching of bandgaps. When the rounding goes up to 350 nm (Figure 4.3(h)), the extra band completely traverses the bandgap in the band structure of the snowflake structure having an ***r*** of 1600 nm (left); its bandgap shifts up which creates a misalignment with the frequency of the double Dirac cone (middle) and the bandgap of the structure having a snowflake ***r*** of 2000 nm (right). For the six-petal holey silicon structure, the circular holes do not suffer from the rounding of sharp corners as in rectangular snowflake arms, and we see that the complete bandgaps, within which the double Dirac cone resides, match in frequency. In the scale of 5000 nm periodicity, the rounding effect may not reach up to 350 nm for the snowflake cavity, however, when the periodicity scales down to 500 nm where the ten-fold higher frequency can be achieved, the impact of rounding effect will be more significant, and the subsequently impaired topological performance should be considered.

As demonstrated in Figures 4.2 and 4.3, the snowflake structure significantly suffers from small geometric variations and the rounding effect, while our six-petal holey silicon design addresses these issues by considering circular hole shapes and enables robust topological properties.

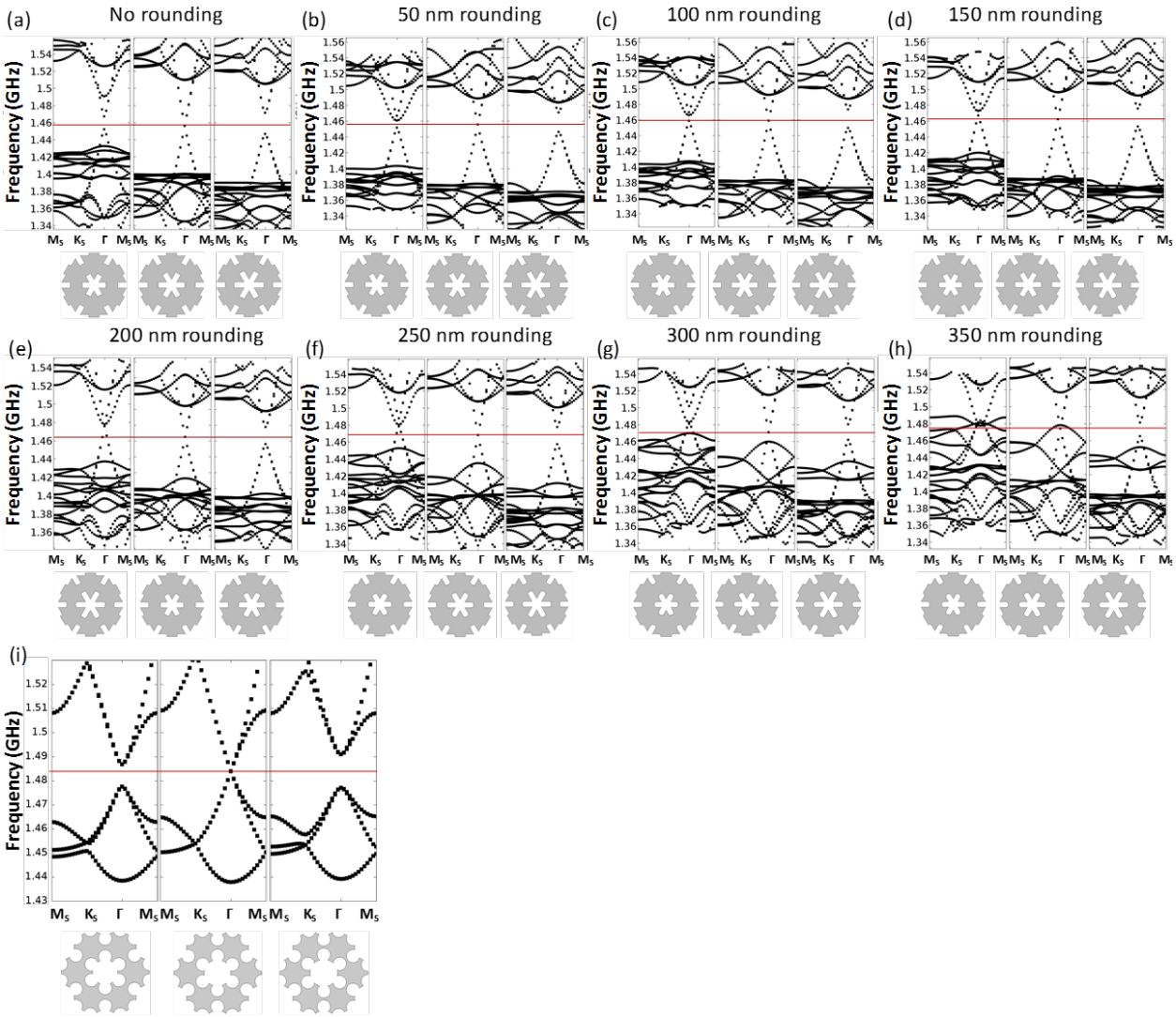

Figure 4.3 Phononic band structures for snowflake structures with a periodicity of 5000 nm (a) without any rounding effect and (b) – (h) suffering from the rounding of 50 nm, 100 nm, 150 nm, 200 nm, 250 nm, 300 nm, and 350 nm. We can see that with 50 nm rounding considered, the simulation results already show an incomplete bandgap for the structure having a snowflake radius of 1600 nm. With the rounding deteriorates, the frequency supporting the double Dirac cone begins to misalign with the frequency ranges of bandgaps, in which a helical edge state supporting topologically protected elastic wave transport cannot be formed. (i) The band structure of six-petal holey silicon with the periodicity of 5000 nm.

4.4 Zone Folding and Band Inversion

As the first step to designing a topological insulator, we create a single Dirac cone for in-plane elastic waves, whose existence has been demonstrated previously for the graphene-like hexagonal-lattice [150,156]. We choose a hexagonal unit cell containing a single six-petal pore, exhibiting a C_6 symmetry [blue in Figure 4.1(a)]. To compute the dispersion properties of the unit cell, we solve the elastic wave equation for six-petal holey silicon using the finite element method in COMSOL Multiphysics with Floquet periodic boundary conditions. By optimizing the geometrical parameters to be ($\boldsymbol{r_o}$, $\boldsymbol{r_i}$, $\boldsymbol{d_{io}}$) = (65, 130, 169) nm, we can obtain a Dirac cone at f = 14.83 GHz [Figure 4.4(a)]. A thickness of 100 nm for the unit cell is selected to achieve a complete bandgap for in-plane waves around the frequency f. To construct a double Dirac cone, we now consider an enlarged unit cell [red in Figure 4.1(a)] with the original unit cell encircled by one-third of each of its six neighbors. This folds the original first Brillouin zone (1BZ) [blue in Figure 4.1(b)] by a factor of $1/\sqrt{3}$ and forms a two-fold degenerate Dirac cone [Figure 4.4(c)] at the $\boldsymbol{\Gamma}$ point by mapping the Dirac cone at $\boldsymbol{K}$ in the original 1BZ to the new one. To realize the band inversion, we remain the radii of all the one-third pores ($\boldsymbol{r_o}$) in the enlarged unit cell as they are and modify $\boldsymbol{r_i}$ and $\boldsymbol{d_{io}}$. The breaking of the discrete translational symmetry, originally characterized by the lattice constant $\boldsymbol{a}$ = 500 nm, makes the enlarged unit cell be the smallest repeating cell with a pair of lattice vectors $\overrightarrow{\boldsymbol{a_1}}$ and $\overrightarrow{\boldsymbol{a_2}}$ and a larger lattice constant of $500\sqrt{3}$ nm (866 nm). Based on the geometrical parameters shown in Figure 4.4(e) for the enlarged unit cell, we obtain two topologically protected band gaps at the $\boldsymbol{\Gamma}$ point in the dispersion curves for two phononic crystals (PnCs) [Figure 4.4(b) and (d)], with inverted degenerate modes at both gap edges illustrated by mechanical displacement [Figure 4.4(e)]. The quadruples ($d_{x^2-y^2}$ and d_{xy}) appear at the high frequency in the trivial PnC [Figure 4.4(b)], whereas they move to the low frequency in the non-

trivial PnC [Fig. 2(d)]. We notice that the neck size, which is the smallest channel size between adjacent pores, reaches ~20 nm in the trivial PnC, which may pose challenges to potential experimental demonstrations requiring high-frequency (i.e., GHz ranges) mechanical response with high-fidelity. The novel design of six-petal holey silicon allows the topologically protected edge state to scale from low to high frequencies via geometric control, which enables topological insulators to operate over a wide range, which is illustrated in Figure 4.5. The frequency of the double Dirac cone and the frequency range of the topologically protected band gaps shown in Figure 4.4 can be scaled proportionally with the size of the geometry. In Figure 4.5, if we increase the periodicity $\boldsymbol{a}$ from 866 (500 √ 3) nm to 8660 (5000 √ 3) nm, we can observe a 10-time decrease in the frequency from 14.83 GHz to 1.483 GHz, at which the phononic band structure shows the band inversion. This linear relationship between the frequency and size of the geometry offers us great flexibility of matching with the required experimental condition. Additionally, this property offers a quick estimation of the frequency range of edge states of the geometry of topological insulators of interest. Experiment-wise, piezo-electric transducers have been used to excite MHz-range elastic waves in out-of-plane[38,39]. For in-plane elastic waves considered in our simulation, interdigital transducer could be a practical candidate. The simulation results presented in the current work would still be applicable when experimental conditions are met and realized in the future.

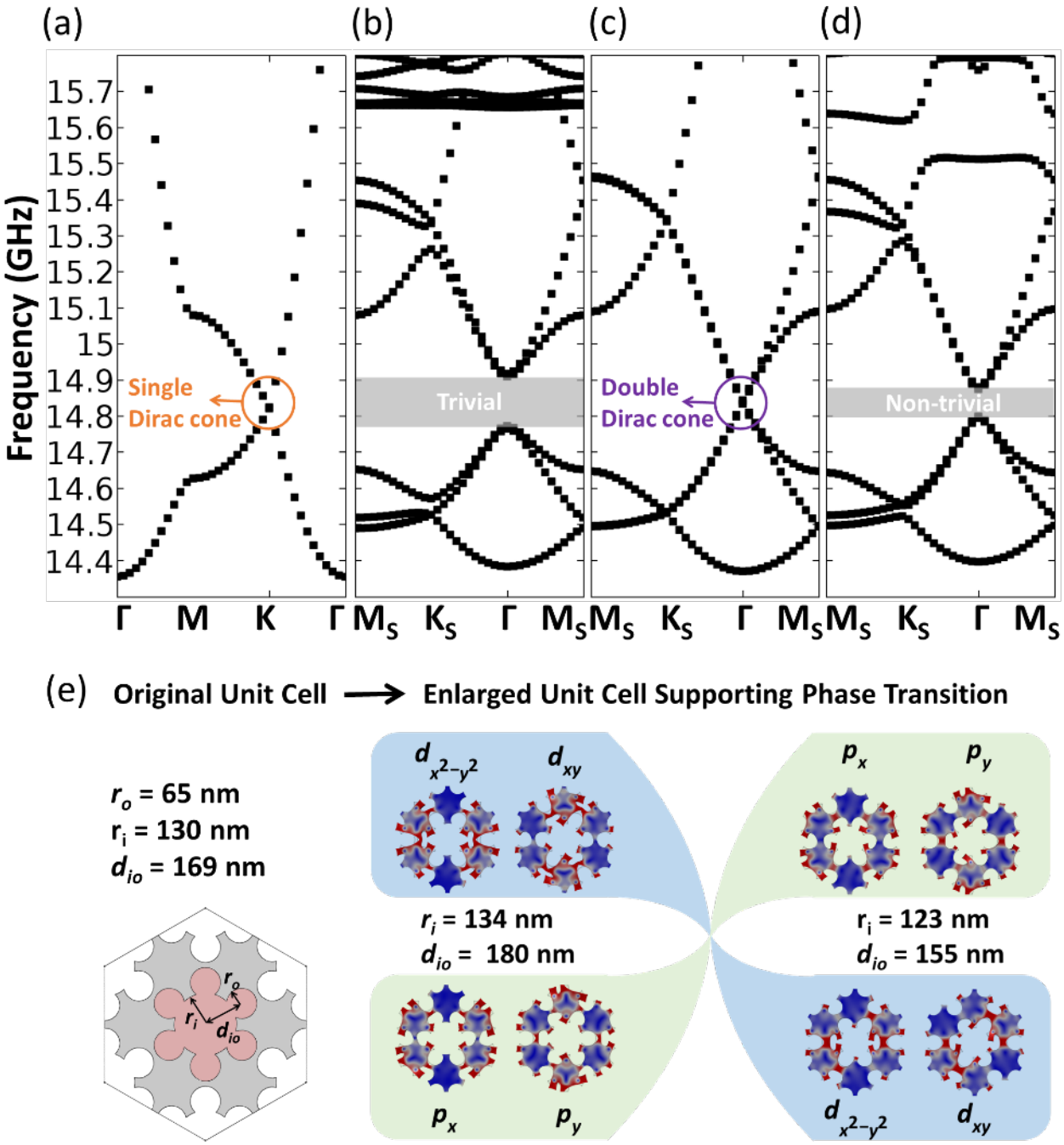

Figure 4.4 Elastic topological insulator design based on six-petal holey silicon nanostructures, which supports the required band inversion process at GHz ranges and offers high tolerance to processing defects. The dimensions of the enlarged unit cell are shown where we keep $\boldsymbol{r_o}$ the same and change $\boldsymbol{r_i}$ and $\boldsymbol{d_{io}}$. (a) Band structure of the original unit cell and the corresponding single Dirac cone at the point $\boldsymbol{K}$. (b)-(d) Band structures of the enlarged unit cell and the corresponding topological phase transition from the zone-folding-induced double Dirac cone to bandgaps by modifying the geometry. (e) The quadruples (d_{x2-y2} and d_{xy}) are found at higher frequencies whereas dipoles (p_x and p_y) are found at lower frequencies, which are trivial. When the band inversion occurs, the quadruples move to lower frequencies while the dipoles move to higher frequencies, which are considered non-trivial. The lattice constant $\boldsymbol{a}$ is kept at 866 nm. In the simulation, we

consider the silicon with Young's modulus of 170 GPa, mass density of 2329 kg-m^{-3}, and Poisson's ratio of 0.28.

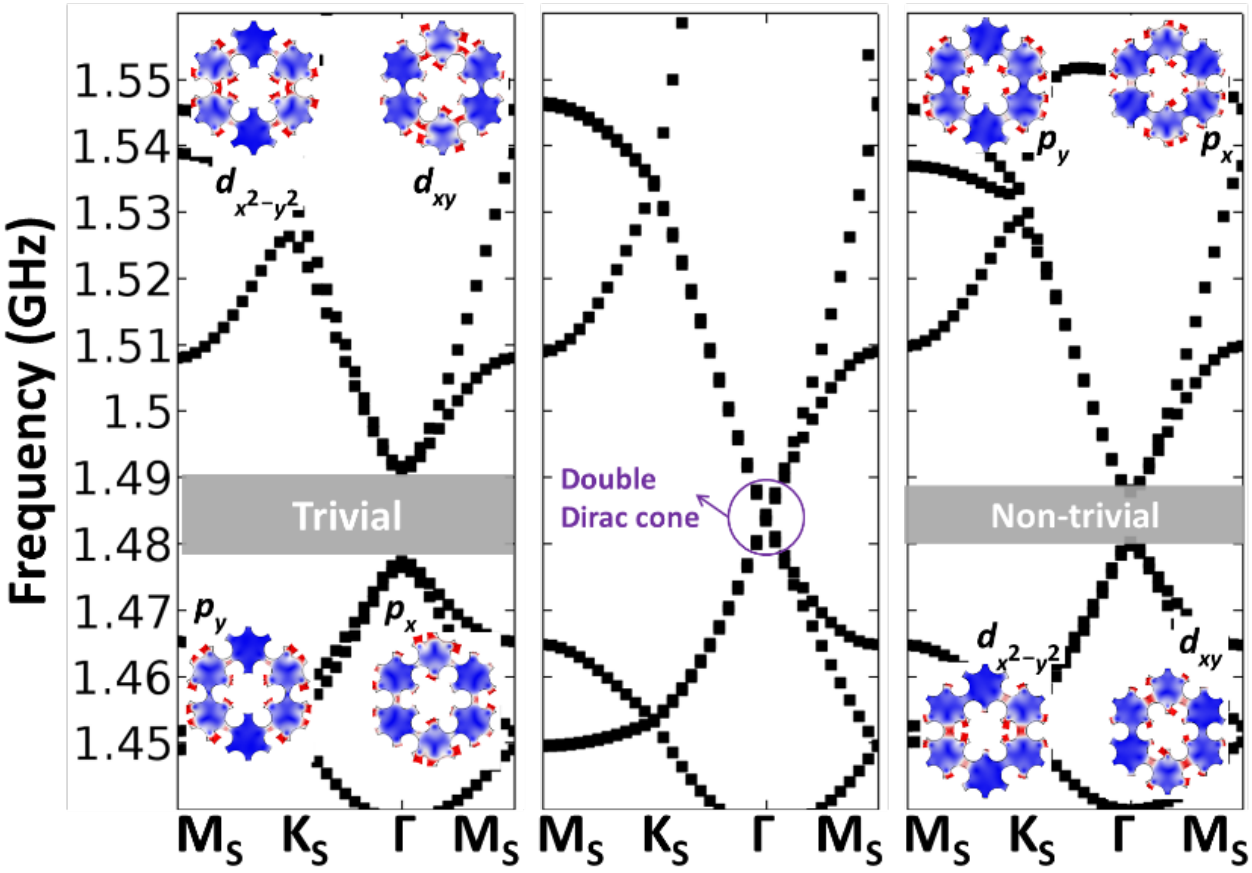

Figure 4.5 The band structure calculated for the geometries scaled up by 10-time compared with the ones shown in Fig. 2 in the main texts. A double Dirac cone is formed at a frequency of *f*' = 1.483 GHz, which is 10-time smaller. By modifying the geometrical parameters, we demonstrate the opening of topologically protected band gaps around *f*'. The inverted degenerate bands at both edges of the band gaps indicate the band inversion, with the mode shapes labeled as quadruples and dipoles shown in the insets.

4.5 Emergence of Topological States

At the interface between two topologically distinct domains, we expect to find the topologically protected edge states [31,142,148]. By connecting the trivial and non-trivial PnCs discussed above to form an interface, we demonstrate the existence of a topological state. We consider a supercell that is periodic along the *x*-direction and finite in the *y*-direction [Figure 4.6(a)]. We first calculate the dispersion curves for the supercells where the topologically identical PnCs are present on both sides of the interface. In Figure 4.6(b) and 4.6(c), we can see the complete band gaps appearing in the bulk band structure except for bands (light-gray) confined at physical boundaries partially traversing the band gaps. They emerge due to the broken symmetry at the boundaries of the finite domain, which are neither related to the topological state at the interface nor protected by any symmetry [142]. When we have trivial and non-trivial PnCs on each side, the above band gaps are replaced by two crossing straight lines [Figure 4.6(d)], indicating the emerge of topologically protected edge states highly localized at the interface [Figure 4.6(e)]. The bands confined at physical boundaries can also be observed, as displayed in Figure 4.6(f). We further calculate the root-mean-square (RMS) displacement of a system comprising of 6 abovementioned supercells placed adjacent to each other horizontally, which is shown in Figure 4.6(g). The elastic wave excited at a frequency of 14.83 GHz, which is within the range of the bulk bandgap (Figure 4.6(d)), propagates robustly from the left to the right demonstrating the topological protection. We notice that the elastic wave also penetrates the bulk region but decays quickly, and the similar penetration has been observed in the previous study [142].

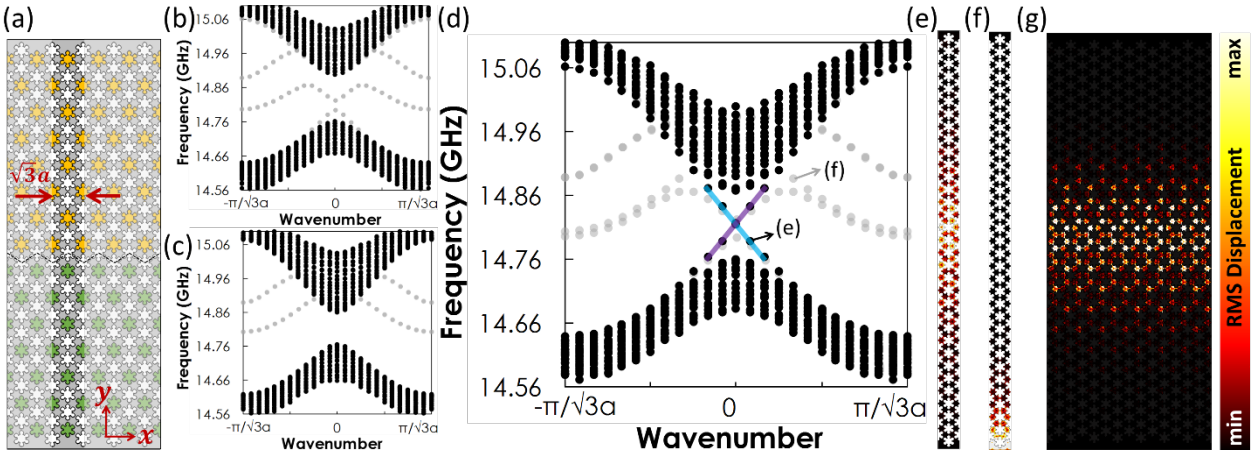

Figure 4.6 (a) The supercell used for computing the bulk band structure which comprises trivial (yellow) and non-trivial (green) PnCs separated by an interface represented by the black dashed line. The depicted supercell contains 11 enlarged unit cells in total with 5 non-trivial ones on top of and 6 trivial ones on the bottom of the interface. (b) Projected bulk band structure of the trivial PnC. The extra bands (light-gray) inside the bulk bandgap are localized on top and bottom boundaries (Fig. 3(f)). (c) Projected bulk band structure of the non-trivial PnC. (d) Projected bulk band structure of a supercell. Edge bands supporting the topologically protected elastic wave transport and their crossing at the point $\boldsymbol{\Gamma}$ is shown by the blue and purple lines. Two representative mode shapes associated with (e) the edge bands and (f) bands at physical boundaries. The latter bands arise from the breakage of symmetry on top and bottom physical boundaries due to the truncated simulation domain and they are not symmetry-protected. (g) Topologically protected edge state.

4.6 Robust Transmission against Geometrical Defects

As the most striking characteristic of topological insulators, the interface between trivial and non-trivial PnCs supports robust elastic wave propagation even in the presence of non-spin-mixing defects [54,64,160]. As the first case, we introduce a zigzag domain wall functioning as a waveguide with two sharp bends of the angles of 60 °, and then we evaluate cases including a lattice disorder formed by exchanging trivial and non-trivial unit cells across the interface and a cavity formed by filling several six-petal pores [63], schematics of all three cases are depicted in Figure 4.7 (lower panel). To avoid any leakage of elastic energy through physical boundaries, we apply low-reflection boundary conditions surrounding the simulation domain. We apply point harmonic excitations on three points in a unit cell separated by a length of *a* and having a phase

delay of $\frac{2\pi}{3}$ between each two at the frequency of 14.83 GHz [144,148,149,155]. Similar multi-point excitation with carefully engineered amplitudes and phases can launch one-way elastic waves, which may favor applications that directional control is desired (See section 4.8 for details). We then calculate the elastic energy density and show its distribution. The transmission of the elastic wave is quantified by taking the ratio of elastic energy densities at the source and the output. For the zig-zag waveguide case in Figure 4.7(a), the elastic wave excited at the source can circumvent the sharp bends and arrive at the output with a transmission of 90 % with no obvious backscattering. For the cases of lattice disorder and cavity [Figure 4.7(b) and 4.7(c)], the elastic wave incident from the source maintains high transmission values of 88 % and 90 %, respectively, against these defects. The elastic wave propagation in all three cases localized closely in the vicinity of the interface and decays quickly into the bulk, indicating the insulating nature of the bulk region. In contrast, the results for the ordinary phononic waveguides with similar defects are drastically different. As a support to this claim, we also simulate ordinary phononic waveguides which are constructed by involving only the trivial phononic crystals (PnCs) discussed in Figure 4.4 and by removing the holes along the domain wall. Displayed in Figure 4.8, we can observe the occurrence of strong elastic resonances when the elastic wave runs into the cavity and lattice disorder, whereas the sharp bends along the zigzag domain wall inhibit significantly the elastic wave propagation by backscattering, resulting in a dramatic decrease of transmission down to less than 10 %. The elastic transmission supported by the topologically protected edge state at the domain wall should theoretically equal to 100 %, while our simulation results show some losses. This might be due to the limited simulation domain size we used to keep the computational effort manageable.

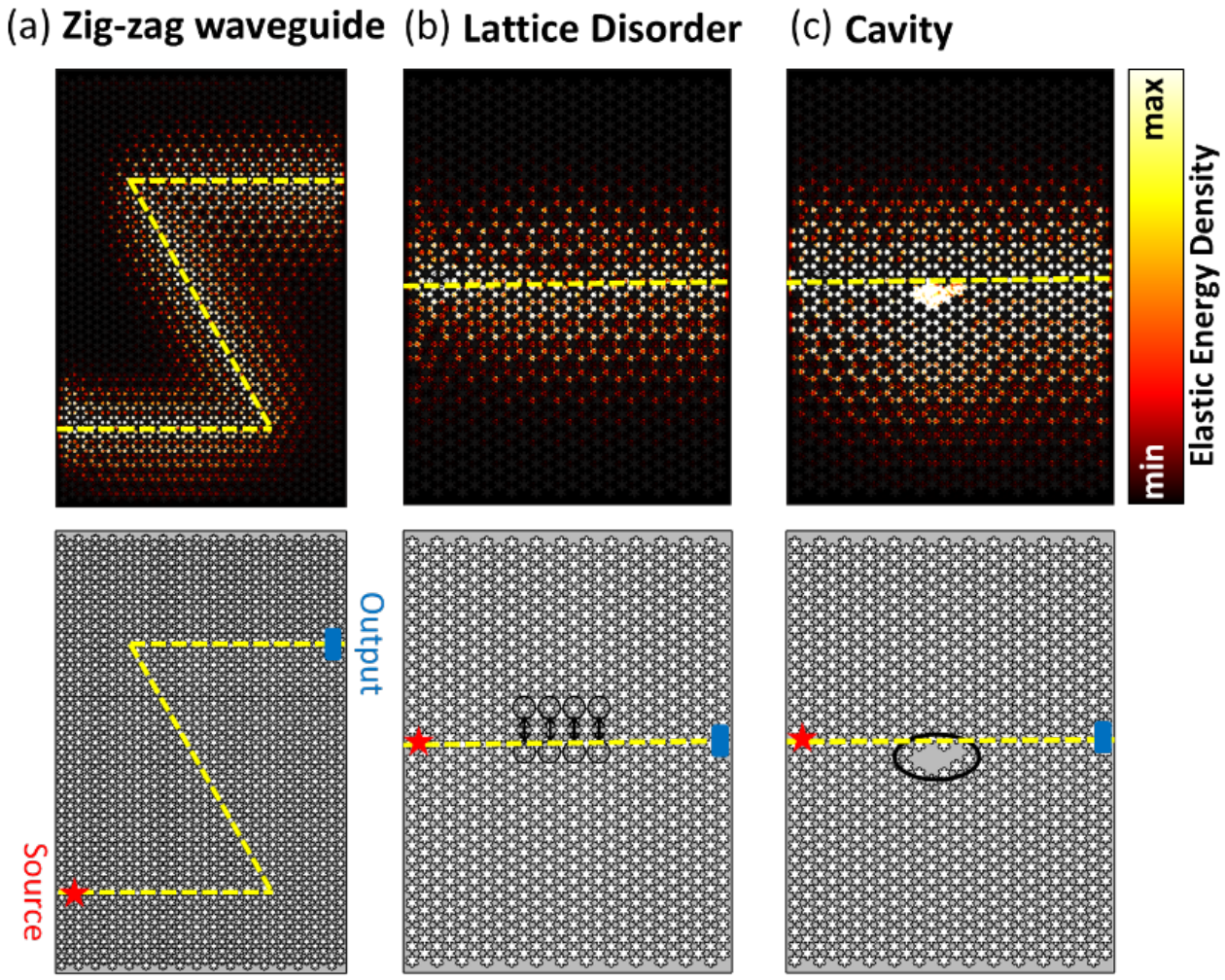

Figure 4.7 Topologically protected elastic wave transmission in (a) a zigzag waveguide, (b) near the interface with a lattice disorder, and (c) a cavity. The normalized elastic energy density shows high elastic wave transmission from left to right of the domain in all three cases (upper panel). We compute the transmission as the ratio between the elastic energy density at the source and the output. The quantified transmissions read 90 %, 88%, and 90 % for the zig-zag domain wall, lattice disorder, and cavity cases. As a comparison, we also simulate ordinary phononic waveguides with similar defects and the results indicate dramatically inhibited elastic wave propagation (transmission values are all less than 10 %), which is in distinct contrast to the high transmissions achieved by the topological insulators, due to the elastic resonance at the cavity and lattice disorder and backscattering at the sharp bends. The schematics depicting the zigzag interface in the waveguide, lattice disorders, and the cavity are displayed in the lower panel.

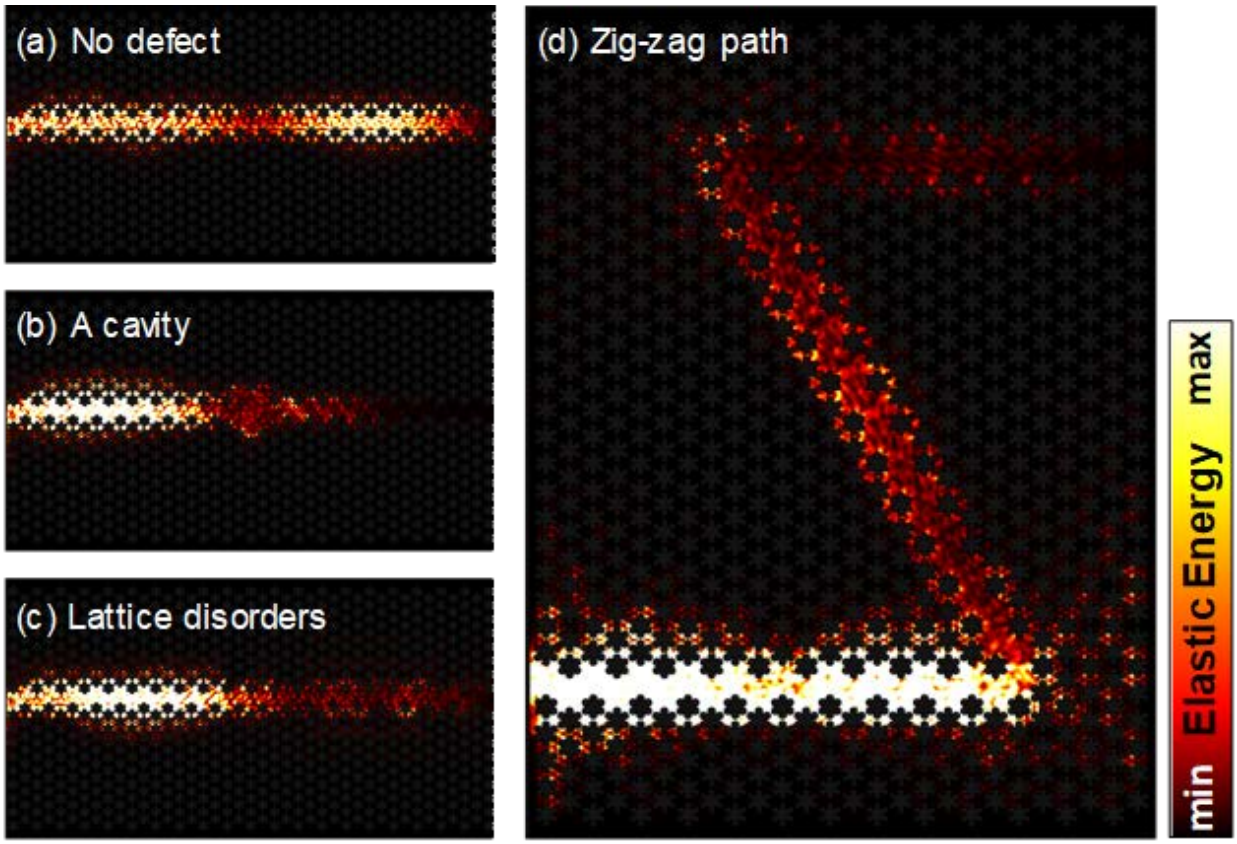

Figure 4.8 Ordinary elastic waveguide constructed by having trivial phononic crystals (PnCs) in the main text and removing the holes along the domain wall. Simulated distribution of elastic energy density for the ordinary waveguide (a) without any geometrical defect, (b) with a cavity formed by filling several holes, (c) with lattice disorder by swapping holes on the edge of two domains, (d) with a zigzag domain wall having two sharp bends. We can observe large backscattering in all four cases with ordinary insulators, which is fundamentally different from what we see from topological insulators with the low-loss transmission in the main text.

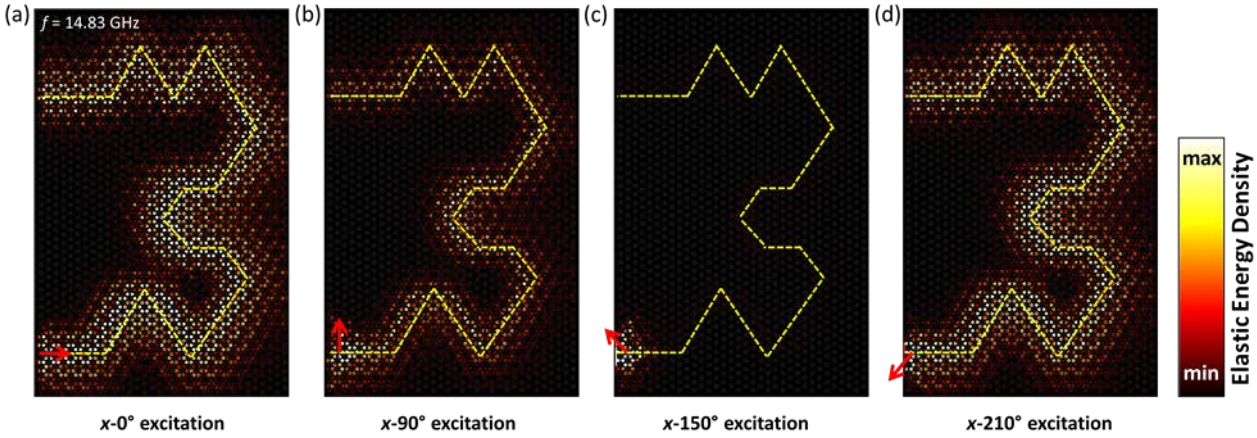

Figure 4.9 Topologically-protected elastic wave transmission in the in-plane that detours 14-bends and shows a dependence on the direction of excitation when the frequency is kept the same at 14.83 GHz. The excitation angles of 0° and 210° show comparably strong elastic energy density along the domain wall, whereas that of the excitation angle of 90° significantly reduces and is even completed confined at the source when the excitation angle is 150°. Note that the excitation angle is measured from the positive ***x***-direction. Such a relationship between the elastic wave propagation and the excitation angle may imply the unique pseudospin nature of the excited waves in comparison to the domain wall topology.

4.7 Robust Transmission against Potential Fabrication Errors

To demonstrate the robustness of six-petal holey silicon to geometric variations and potential fabrication imperfections, we study the possibility of sustaining the topologically protected elastic wave transmission against sizing errors of holes, and the analysis shows that the six-petal structure offers high transmission for sizing errors up to 11 % and -6 %, respectively. The over-/under-sizing is simulated by increasing or decreasing the diameters of central ($\boldsymbol{r_i}$) and corner circles ($\boldsymbol{r_o}$) by the same thicknesses while maintaining the distance ($\boldsymbol{d_{io}}$) untouched based on the precisely-sized hole dimensions (Figure 4.4). The simulation results of supercells in Figure 4.9 (a) and (b) show that the six-petal structure allows an over-sizing up to 7.2 nm or an under-sizing down to 4 nm, which are equivalent to an 11 % increase or a 6 % decrease of hole sizes with respect to $\boldsymbol{r_o}$. Previous work regarding silicon nanoporous structures has achieved high-precision control on the fabrication inaccuracy down to ±2 nm [161], which is well within the allowed range of sizing errors for the six-petal design. The topological edge states, indicated by two linear dispersion curves crossing at k_x of 0, can be observed inside bulk bandgaps (marked by light-purple boxes). We notice that the frequency corresponding to the double Dirac cones in both over- and under-sizing cases deviate from that of the precisely-sizing case (Figure 4.4). And we could attribute these frequency shifts to the excessive or inadequate removal of materials resulted from potential fabrication-induced errors such as those in etchings or lithographical expose. The full-field simulations in Figure 4.9(b)

and (d) demonstrate robust elastic wave transmissions up to 96.1 % for over-sizing of 11 % and under-sizing of 6 % assuming the sizing errors are uniformly distributed. The high elastic energy density confined in the vicinity of the interface, which quickly decays into the bulk regions, implies the elastic wave propagation is topologically protected. Although our simulation results in Figure 4.9 (b) and (d) consider the uniform distribution of sizing errors over the entire domain, in practical fabrication, the errors of varying percentages could randomly locate. For example, majority holes in a domain might be over-sized by 2 % while a few holes might be over-sized by 6 %. The 6 % over-sized holes could distribute randomly either near the interface or in the bulk regions. While the topological edge states and hence topologically protected elastic wave propagation could still be supported even when the randomness is present, the transmission would be impacted and further investigation would be desired (See section 4.9 for details). To provide additional insights into the evolution of phononic band structure as a result of varying the extent of over- and under-sizing, we document the band structures of six-petal holes over-sized by 1% to 10% and under-sized by 1% to 5%, respectively, in Figure 4.10 and 4.11. In all cases, the double Dirac cones stay within overlapped bandgaps (marked by light-purple boxes). The frequency of double Dirac cone shifts from that of the precisely-sized case and this could be attributed to the excessive or inadequate removal of materials associated with over- or under-sizing errors.

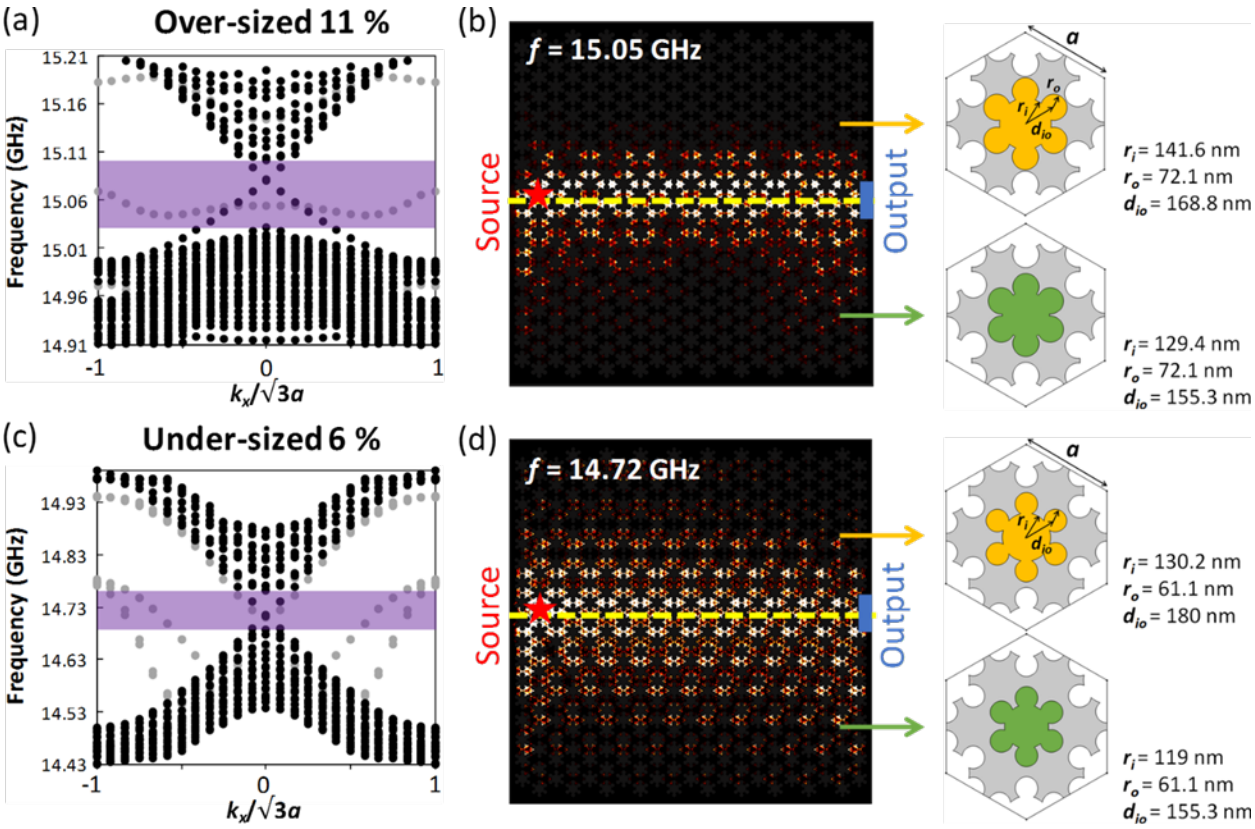

Figure 4.9 (a) Projected bulk band structure calculated for a supercell (11 unit cells with 6 trivial ones on top and 5 non-trivial ones on the bottom of the interface) consisting of six-petal holes over-sized by 7.2 nm (an 11 % increase of hole diameters with respect to r_o). (b) Full-field simulation of elastic wave transmission excited at 15.05 GHz with six-petal holes over-sized by 11 %. The over-sizing errors are assumed to be uniformly distributed over the entire simulation domain. (c) Projected bulk band structure for a supercell consisting of six-petal holes under-sized by 4 nm (a 6 % decrease of hole diameters with respect to r_o). (d) Full-field simulation of elastic wave transmission excited at 14.72 GHz with six-petal holes under-sized by 6 %. Again, the under-sizing error is assumed to be uniformly distributed. The hole dimensions suffering sizing errors are given in the schematics. The yellow and green correspond to trivial and non-trivial unit cells.

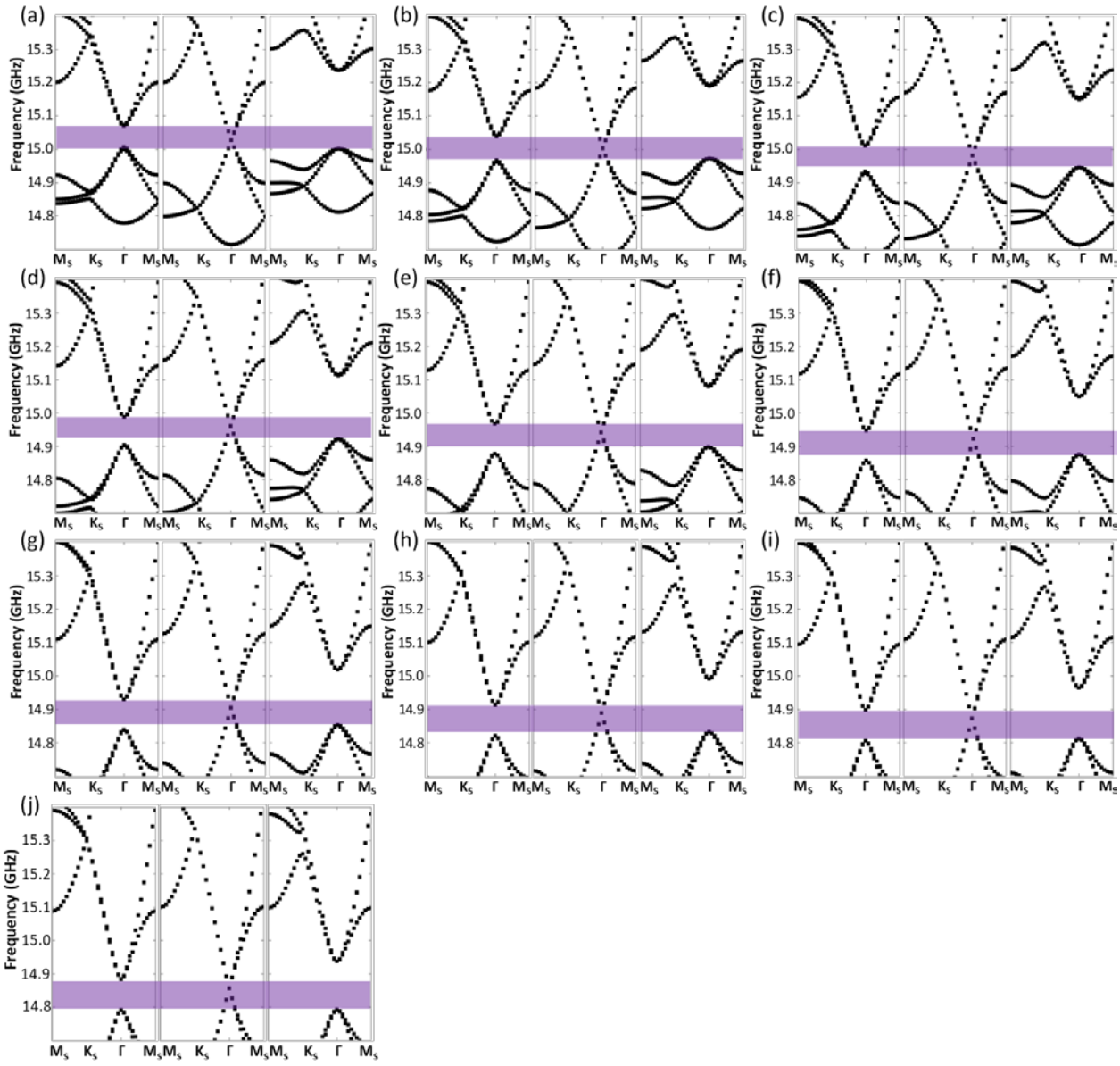

Figure 4.10 (a) – (i) The phononic band structure for the six-petal holes over-sized by 10 % to 1 %, where over-sizing is considered by enlarging all circles in each six-petal hole by 6.5 nm to 0.65 nm. As the over-sizing increases, the band inversion remains whereas the double Dirac cone and the overlapped bandgaps (light purple boxes) shift up with increasing material loss (i.e., less mass of the structure).

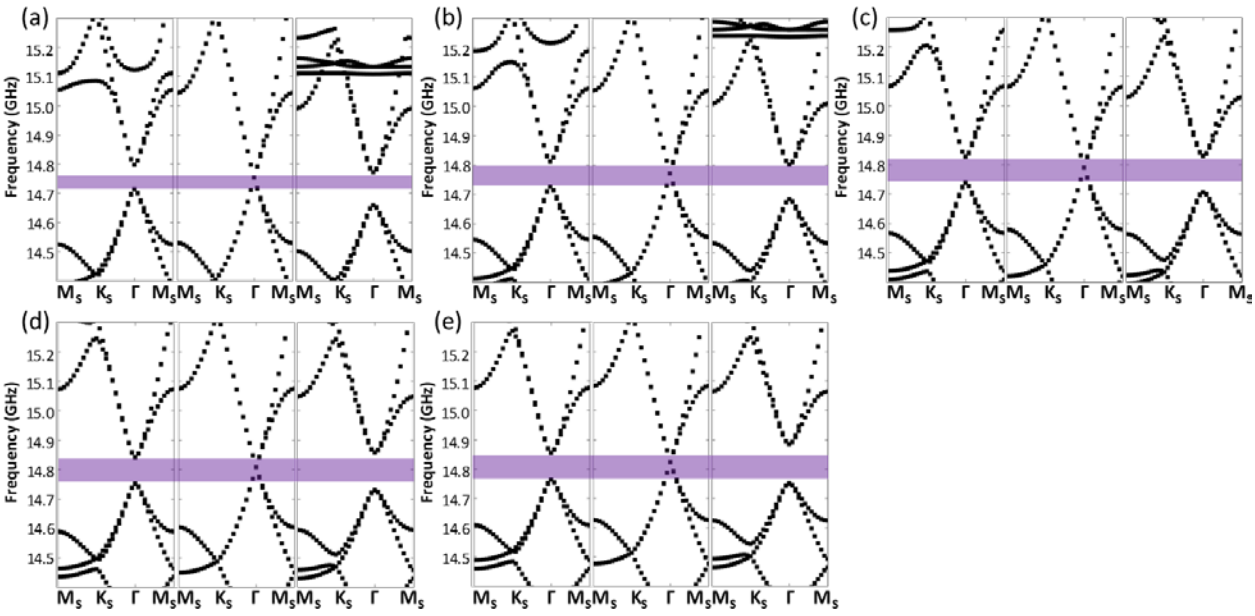

Figure 4.11 (a) – (e) The phononic band structure for the six-petal holes under-sized by 1 % to 5 %, where under-sizing is considered by shrinking all circles in each six-petal hole by 0.65 nm to 3.9 nm. As the under-sizing increases, the band inversion remains whereas the double Dirac cone and the overlapped bandgaps (light purple boxes) shift down with decreasing material loss (i.e., less mass of the structure).

4.8 Multi-point excitations and one-way elastic wave propagation

Regarding the excitation we used in this work, apart from launching the wave traveling along the interface with geometric defects as shown in Figure 4.7 and 4.9, it is also significantly useful for exciting one-way elastic wave. In Figure 4.12 (a) and (b), we show that by carefully engineering the amplitudes and phases of point sources, we can selectively excite left- or right-moving waves. The amplitudes and phases are based on the supercell analysis of the same hole dimensions. In Figure 4.12(c), we show that the wave will go in both directions if we use the same amplitudes and phases as in the manuscript, which is not configured for one-way wave transport. Though waves in two directions are excited simultaneously, the transmission will not be affected because the sources locate close to the left boundary of the simulation domain so that the low-reflection boundary condition ensures the absorption of the left-moving wave.

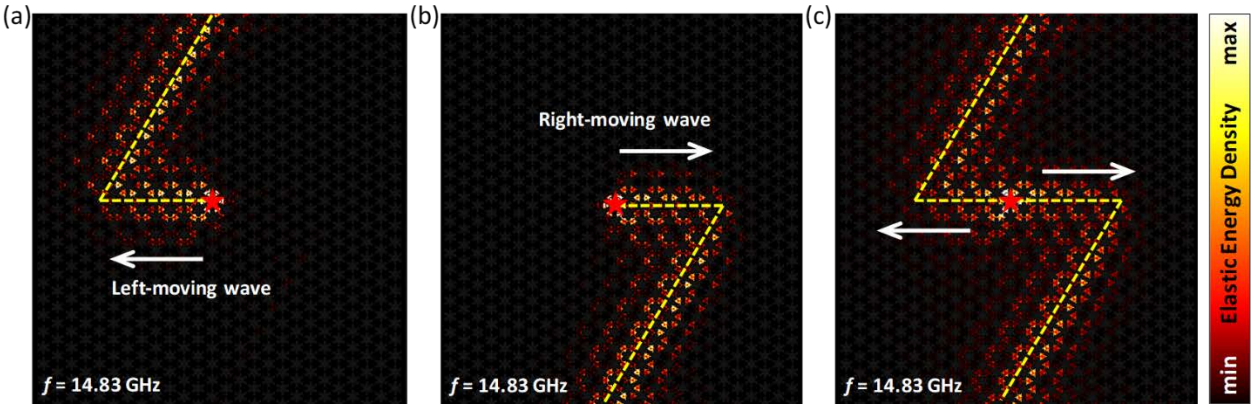

Figure 4.12 Full-field simulations of (a) Left-moving elastic wave excited by applying multi-point excitations with carefully configured amplitudes and phases at the position marked by the red star. (b) Right-moving elastic wave launched by applying multi-point excitations with the same amplitudes as in (a) but opposite phases. (c) Elastic waves excited to propagate in both directions by using the same three-point excitation scheme (same force amplitudes and phases) as in the manuscript. The holes are precisely-sized.

4.9 Discussions

4.9.1 The Effects of Random Sizing Errors

We have assumed uniform size errors of a certain percentage in the previous sections of this chapter, to show that the helical edge state can still be supported even when randomly distributed etching errors are present, we run full-field simulations containing 367 holes with 2 % over-sized holes being as the majority and 6 % over-sized holes being randomly located along the interface or in the bulk domains. Since the helical edge state is confined in the vicinity of the interface, we expect the 6 % over-sized holes placed at/near the interface to impact more the transmission of the elastic wave. As we can see in Figure 4.13(a), when 2 % over-sizing errors are uniformly distributed over the entire domain, we observe 92 % elastic wave transmission from the source to the output. When four 6 % over-sized six-petal holes are randomly distributed at the interface, we can see in Figure 4.13 (b) that the elastic wave propagation weakens when encountering the 6 %

over-sized holes, but a fraction of the wave can still circumvent and reach the output, leading to a decreased transmission of 37.8 %. If we add another four 6 % over-sized holes base on the four in Figure 4.13(b) and place them randomly in the bulk regions, we can observe in Figure 4.13(c) that the transmission further deteriorates, and much less elastic wave can detour the 6 % over-sized holes to arrive at the output, resulting in transmission only of 34 %. We notice that the effect of adding random 6 % over-sized holes in the bulk regions does not affect the transmission at the interface significantly (a 3.8 % difference in transmission). This indicates that the robustness of our design against randomly distributed etching errors is more sensitive to the randomness induced near the interface. Finally, if we gather the eight 6 % over-sized holes in Figure 4.13(c) at the interface, as shown in Figure 4.13(d), we find that the transmission of elastic wave significantly decreases when encountering the randomly distributed 6 % over-sized holes at the interface with only a small fraction detouring those holes and reaching the output. The corresponding transmission drops to 11.3 %. The reason why the random distribution of 6 % over-sized holes inside the matrix of 2 % over-sized holes is the mismatched bandgaps in the band structure. As shown in Figure 4.14, both over-sized holes support the band inversion. However, the bandgap which will allow the existence of helical edge states for these hole dimensions does not overlap, with the lower bound of the bandgap for the 2 % over-sized hole being above 14.9 GHz while the upper bound of the bandgap for the 6 % over-sized hole being below 14.9 GHz. Therefore, when 6 % over-sized holes and 2 % over-sized holes co-exist at the interface and wave is excited at 14.86 GHz, which should allow propagation in the 2 % over-sized holes, the elastic wave cannot propagate in the 6 % over-sized holes at this frequency. A hypothesis we made is that if the different over-sized holes share a frequency range over which the edge state is supported, the transmission of elastic wave, compared with the above case, could be improved. To test this, we

replace the 2 % and 6 % over-sized holes with 11 % and 10 % over-sized holes and keep all other geometries untouched. In Figure 4.15, we first show the band structures of supercells consisting of six-petal holes over-sized by 11 % and 10 %, respectively. The edge states, indicated by straight lines crossing at k_x of 0, embeds inside the bulk bandgaps; the extra bands inside the bulk bandgaps are due to the breakage of symmetry at the physical boundaries of the simulation domain, which is irrelevant to the topological edge states. To calculate the elastic wave transmission, we do full-field simulations with 2 % and 6 % over-sized holes in Figure 4.13 replaced by 11 % and 10 %. The positions of the 10 % over-sized holes are identical to those of 6 % over-sized holes. Exciting the elastic wave at 15.05 GHz, we can see that if the six-petal holes are uniformly over-sized by 11 %, the elastic wave transmission from the source to output reaches 96.1 % (Figure 4.15(c)). If four 10 % over-sized holes randomly replace the 11 % holes at the interface, the transmission drops to 55.6 % (Figure 4.15(d)). With four more 10 % holes randomly distributed in the bulk regions, as shown in Figure 4.15(e), the transmission is not significantly affected, similar to what has been observed in Figure 4.13(c). When all eight 10 % over-sized holes concentrate on the interface, the reduction of transmission becomes significant, decreasing to 46.1 %. All transmission values enhance compared with the cases where 2 % and 6 % over-sized holes present.

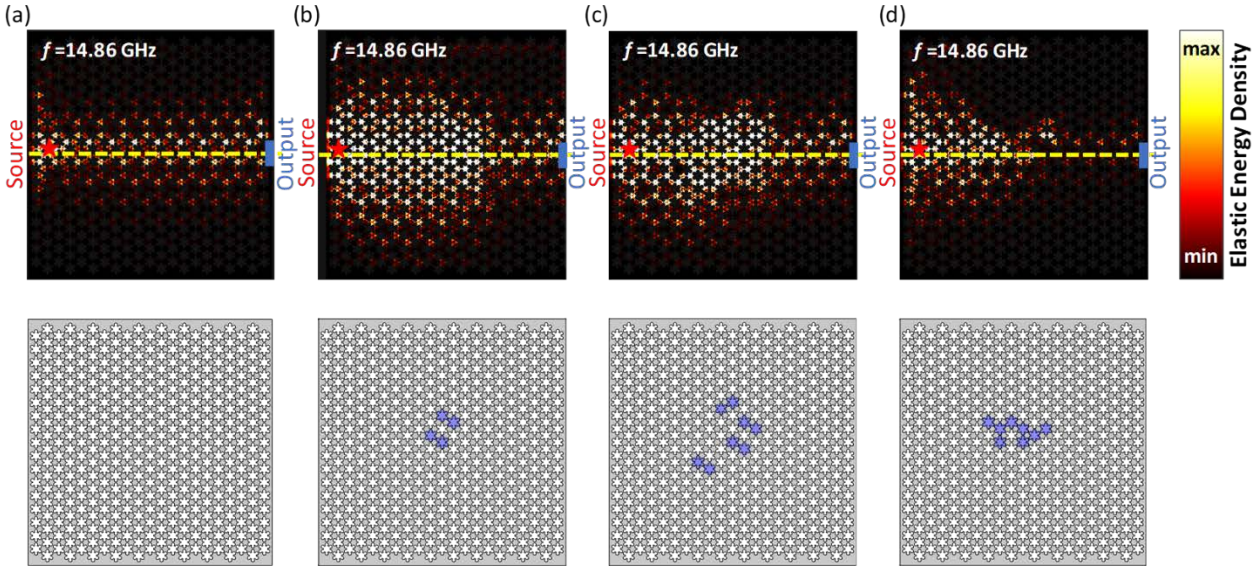

Figure 4.13 Full-field simulations of the elastic wave transmission in phononic topological insulators with (a) all six-petal holes over-sized uniformly by 2 %, (b) 363 of six-petal holes over-sized by 2 % and 4 holes at the interface over-size by 6 %, (c) 359 of six-petal holes over-sized by 2 % and 8 holes over-sized by 6 % randomly distributed at the interface and into the bulk region, and (d) 359 of six-petal holes over-sized by 2 % and 8 holes randomly distributed at the interface over-sized by 6 %. The transmission for the 2 % uniformly over-sized case is 92 %. When 4 holes are over-sized by 6 %, the transmission decreases to 37.8 %. When 8 holes with 6 % over-sizing are randomly located at the interface and in the bulk region, the transmission further reduces to 34 %. When 8 holes with 6 % over-sizing are randomly distributed at the interface, the elastic wave propagation transmission drops to 11.3 %.

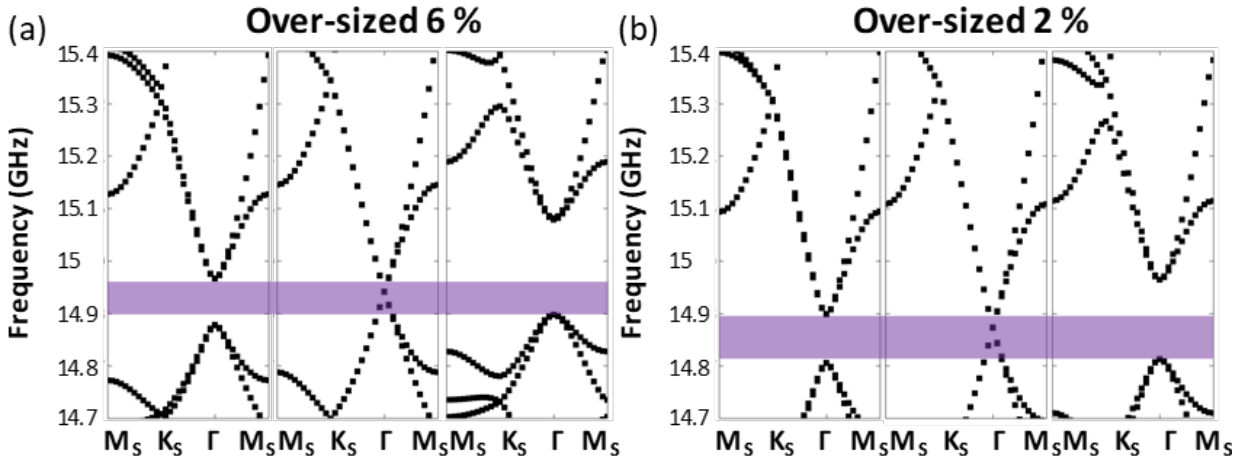

Figure 4.14 The phononic band structures of the six-petal holey silicon over-sized by (a) 6 % and (b) 2 %. The frequencies of bandgaps mismatch and thus the helical edge states for these cases do not have a shared frequency range.

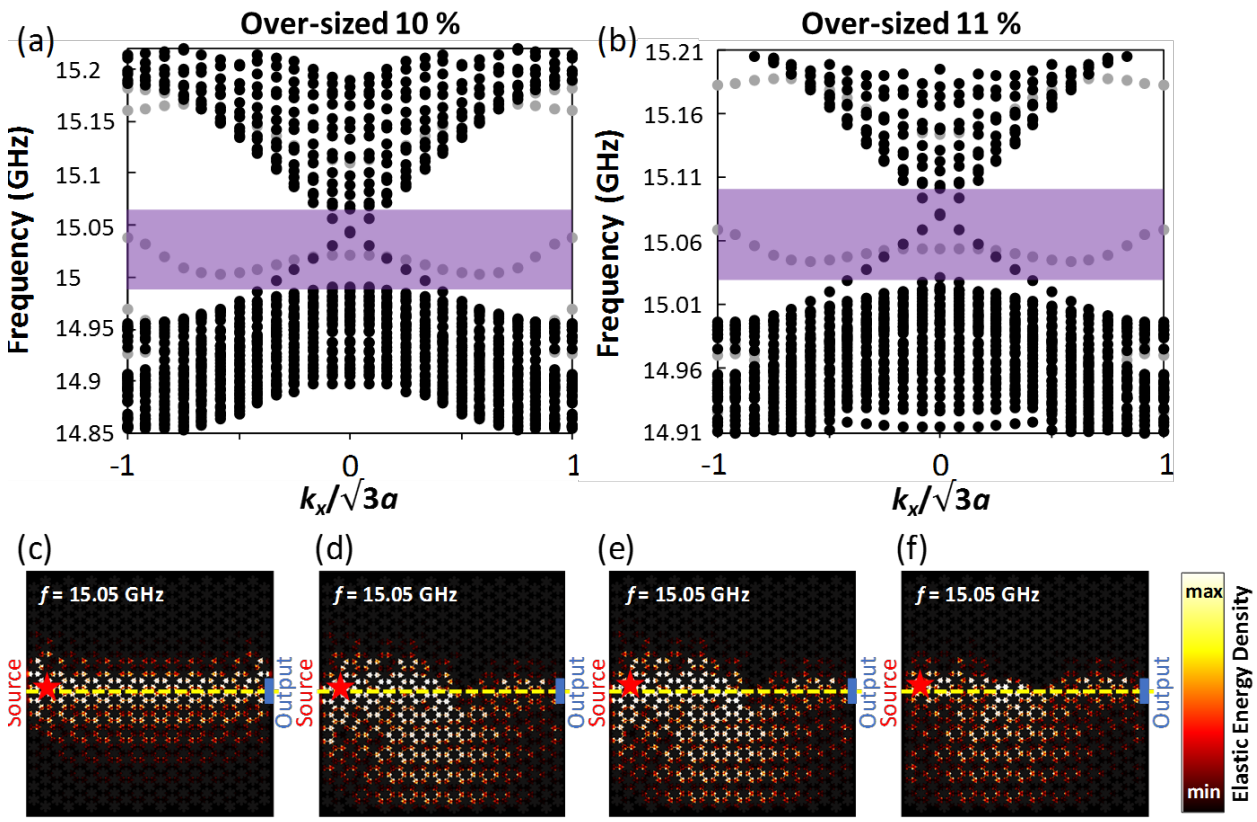

Figure 4.15 The band structure of supercells with six-petal holes over-sized by (a) 10 % and (b) 11 %. The bulk bandgaps are marked by light-purple boxes. The topologically protected edge states are shown by two straight lines crossing at k_x of 0. The light-grey bands are confined at the physical boundaries due to the breakage of symmetry and are irrelevant to the topological edge states. The full-field simulation of elastic wave propagation shows that (c) when the six-petal holes are uniformly over-sized by 11 %, the elastic wave transmission from the source to the output reaches 96.1 %. However, when (d) four 11 % over-sized holes are replaced by 10 % over-sized holes at the interface, the transmission drops to 55.6 %. If (e) four more 10 % over-sized holes are randomly added to the bulk regions, the transmission is not significantly affected, slightly decreasing to 54 %. When (f) eight 10 % over-sized holes concentrate at along the interface, the transmission is reduced much significantly than in (d) and (e), arriving at 46.1 %. Comparing with the cases with 2 % and 6 % over-sized holes, the transmission of the field with 11 % and 10 % over-sized holes enhances.

4.9.2 Realization of Topological States for Out-of-plane Elastic Waves

The six-petal holey Si structure can induce topological phase transition and hence the topologically-protected edge states for both in-plane and out-of-plane elastic waves. In Figure

4.16(a), a band inversion similar to that in Figure 4.4(b)-(d) demonstrates the topological phase transition and the formation of two topologically distinct phononic crystals with their unit cell geometries shown in Figure 4.4(b) on the left and right. Note that dimensions in the middle correspond to the unit cell that forms the double Dirac cone at a frequency of ~11.8 GHz. The out-of-plane elastic vibration is immediately obvious by the inset, where the displacement is along the ***z***-axis. The backscattering-immune propagation for out-of-plane elastic waves against geometric defects is illustrated in Figure 4.17 for a disorder (left), a cavity (middle), and a zig-zag path formed by two sharp bends of 60°. The elastic wave displacements are highly localized to the domain wall, which demonstrates the topologically-protected edge states immune to defects, whereas quickly fade away into the bulk near the vicinity of the domain wall, which evidence the insulating nature of bulk regions. Again, we show, in the inset, the displacement is in the ***z***-axis.

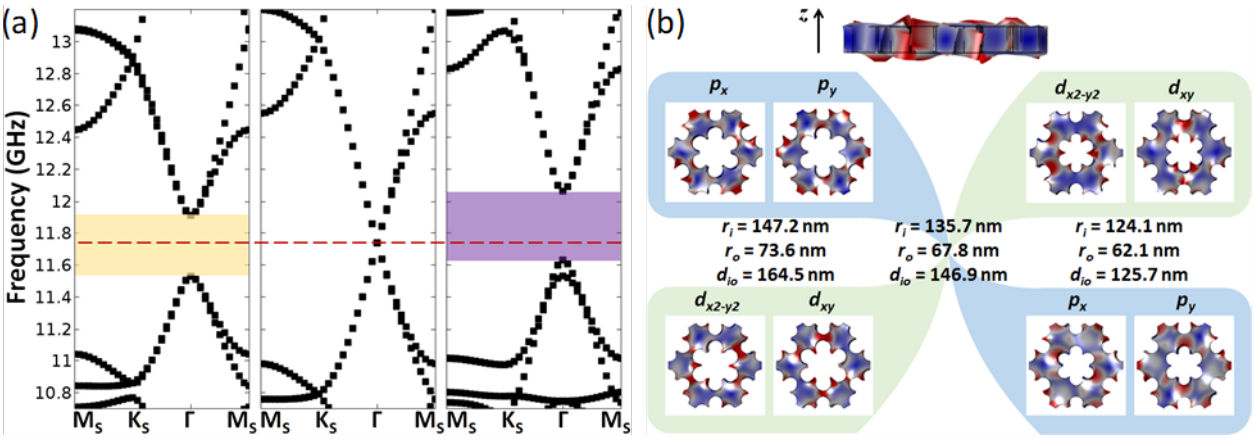

Figure 4.16 Topological phase transition for out-of-plane elastic waves. (a) The double Dirac cone forms at a frequency of 11.7 GHz for the out-of-plane elastic wave. Breaking the translational symmetry induces band inversion that forms two PnCs, one being trivial while the other one being non-trivial. (b) The geometric parameters of the unit cells for six-petal holey structures that support the trivial PnC, double Dirac cone, and the non-trivial PnC, respectively. The inset shows the displacement is in the z-direction, which is the out-of-plane direction.

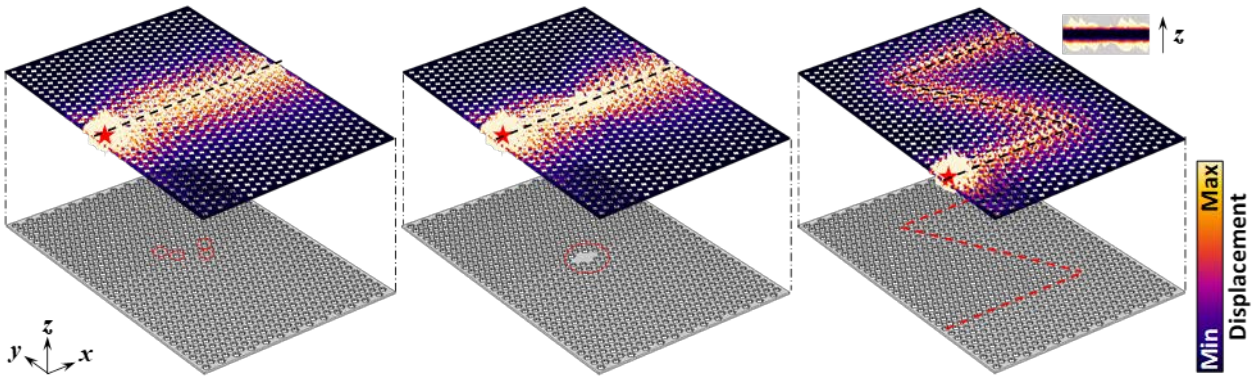

Figure 4.17 Backscattering-immune out-of-plane elastic wave transmission against geometric defects including (a) a disorder, (b) a cavity, and (c) a zig-zag path formed by two sharp bends of 60°. The schematic of each defect is depicted by red-dashed circles in the bottom-panel. The transmissions in (a)-(c) are all above 96.1%. The excitation is in the *z*-direction, which is marked by a red star, while the domain wall separating the trivial and non-trivial PnCs is illustrated by black-dashed curves. The inset in the up-right corner shows the displacement is in the *z*-direction, which again is in the out-of-plane direction. Note that the light-grey background in the inset is to enhance the contrast for better visualization.

4.10 Conclusions

This work presents a holey silicon-based phononic topological insulator design that can demonstrate the topological states and the directional control of in-plane elastic waves up to 14.83 GHz when the periodicity of the unit cell is scaled to 866 nm. The six-petal design allows the C_6 symmetry to form a double Dirac cone based on zone-folding and simple geometric control to break the discrete translational symmetry to achieve topological phase transition. This phase transmission can be easily shifted to low- and high-frequency by scaling up and down the periodicity. The simulations show robust elastic wave propagation with a transmission ratio up to 90 % even in the presence of geometrical defects including a cavity, a disorder, and a zigzag domain wall with sharp bends. The six-petal design intrinsically avoids the potential rounding effect of sharp geometric features in fabrication which may deteriorate the performance of topological insulators. The design is also robust against the potential fabrication-induced errors

such as under-sizing and over-sizing up to 6 % and 11 %, respectively; in both cases, we observe a shift of bandgap compared with that of the precisely-sized geometry and low-loss elastic transmission (up to 90 %). These findings are promising for developing high-frequency phononic topological insulators and phononic waveguides and realizing large-scale phononic circuits for information processing.

CHAPTER 5: REFLECTIVITY OF SOLID AND HOLLOW MICROSPHERE COMPOSITES AND THE EFFECT OF UNIFORM AND VARYING DIAMETERS

While solid and hollow microsphere composites have received significant attention as solar reflectors or selective emitters, the driving mechanisms for their optical properties remain relatively unclear. Here we study the solar reflectivity in the 0.4-2.4 μm wavelength range of solid and hollow microspheres with the diameter varying from 0.125 μm to 8 μm. SiO_2 and TiO_2 are considered as low- and high-refractive-index microsphere materials, respectively, and polydimethylsiloxane is considered as a polymer matrix. Based on Mie theory and finite-difference time-domain simulations, our analysis shows that hollow microspheres with a thinner shell are more effective in scattering the light, compared solid microspheres, and lead to a higher solar reflectivity. The high scattering efficiency, owing to the large interface density, in hollow microspheres allows low-refractive-index materials to have high solar reflectivity. When the diameter is uniform, 0.75 μm hollow microspheres provide the largest solar reflectivity of 0.81. When the diameter is varying, the randomly-distributed 0.5-1 μm SiO_2 hollow microspheres provide the largest solar reflectivity of 0.84. The effect of varying diameter is characterized by strong backscattering in the electric field.

5.1 Introduction

Passive radiative cooling using outer space as the heat sink has revolutionized the thermal management of the building [67,162], human body [163,164], and deep space applications [165]. Among these materials [76,162,163,166–171], particle-polymer composites are promising due to simple and scalable processing [76,172]. Numerous studies have shown effective radiative cooling

using polymers with dielectric particle embedment with/without metal reflectors [76–78]. Alternative designs incorporating hollow particles achieve higher solar reflectivity due to increased interface density [173]. Additionally, such a core-shell structure enables tunable material properties. Successful demonstrations of colored pigments [174–176], spectrally-selective photonic film [177], climate-control building coatings [178,179], thermal insulation [180], and super hydrophobicity [176] have been realized. Recently, structural hierarchy, which already exists in nature [181], has been employed as an additional knob to configure the optical properties of artificial materials. The size-dependent optical response of hierarchical building blocks provides broadband high reflectivity or absorptivity in the solar spectrum, enabling far-reaching applications in novel radiative cooling films [67], solar energy harvesting [182], structural coloration [183], and photocatalysis [184]. A noteworthy hierarchical cooling film developed by Peoples et al. (2019) lately demonstrated broadband-enhanced solar reflectivity by tuning the size composition of low-concentration TiO_2 nanoparticles of 104 ± 37 nm [79]. The efficacy of size hierarchy was supported by Monte Carlo and Mie theory calculations assuming individual scattering. The composite with the optimized particle size constitution yields reflectivity higher than that of each building block, yet precise control on the particle size could be practically challenging. While hollow particles and structural hierarchy have individually demonstrated their effectiveness in achieving high solar reflectivity, their combined effect, to our best knowledge, has only received limited attention [185]. Our recent work demonstrated radiative cooling enabled by hollow glass microspheres with varying diameters but the effect of diameter variation was not studied in detail [66]. In this letter, we performed a systematic investigation on randomly close-packed hollow SiO_2 microspheres in poly(dimethylsiloxane) (PDMS) with uniform and varying diameters ranging in 0.125 to 8 μm using Mie theory and finite-difference time-domain (FDTD)

calculations. By conducting single-particle Mie theory calculation, we identify geometric parameters that drive high reflectivity in wavelengths of 0.4-2.4 μm. By performing 2D FDTD simulations, which is valid and more computationally-affordable [186] than previous approaches [196–198], we investigate the effect of the shell thickness and material. Finally, the effect of diameter variation is studied, guiding future optimal designs of radiative cooling composites [199].

5.2 Mie theory

The scattering coefficients of individual hollow microspheres are computed based on Mie theory formalism adopted for core-shell particles [190] and the open-source program developed by Matzler [191]. The scattering, extinction, and absorption efficiencies are outlined as the following

$$Q_{sca} = \frac{2}{x^2}\sum_{n=1}^{\infty}(2n+1)(|a_n|^2 + |b_n|^2) \quad [1]$$

$$Q_{ext} = \frac{2}{x^2}\sum_{n=1}^{\infty}(2n+1)\mathrm{Re}(a_n + b_n) \quad [2]$$

$$Q_{abs} = Q_{ext} - Q_{sca} \quad [3]$$

The coefficients a_n and b_n are

$$a_n = \frac{\left(\widetilde{D}_n/m_2 + n/y\right)\psi_n(y) - \psi_{n-1}(y)}{\left(\widetilde{D}_n/m_2 + n/y\right)\xi_n(y) - \xi_{n-1}(y)} \quad [4]$$

$$b_n = \frac{\left(m_2\tilde{G}_n + n/y\right)\psi_n(y) - \psi_{n-1}(y)}{\left(m_2\tilde{G}_n + n/y\right)\xi_n(y) - \xi_{n-1}(y)} \quad [5]$$

where the size parameters are defined for both core and shell as $x = \frac{2m_1\pi r_1}{\lambda}$, and $y = \frac{2m_2\pi r_2}{\lambda}$ with r_1 and r_2 being their radii, respectively. The coefficients $\widetilde{D}_n$ and $\tilde{G}_n$ are given by

$$\widetilde{D}_n = \frac{D_n(m_2x) - A_n\chi_n^{'}(m_2y)/\psi_n(m_2y)}{1 - A_n\chi_n(m_2y)/\psi_n(m_2y)} \quad [6]$$

$$\widetilde{G}_n = \frac{D_n(m_2x) - B_n\chi_n^{'}(m_2y)/\psi_n(m_2y)}{1 - B_n\chi_n(m_2y)/\psi_n(m_2y)} \quad [7]$$

where

$$A_n = \psi_n(m_2x)\frac{mD_n(m_1x) - D_n(m_2x)}{mD_n(m_1x)\chi_n(m_2x) - \chi_n^{'}(m_2x)} \quad [8]$$

$$B_n = \psi_n(m_2x)\frac{D_n(m_1x)/m - D_n(m_2x)}{D_n(m_1x)\chi_n(m_2x)/m - \chi_n^{'}(m_2x)} \quad [9]$$

with effective optical indices defined by m_1 and m_2 for the core and shell, and $m = \frac{m_2}{m_1}$.

A detailed description of the Mie theory and the related methodology used throughout this Chapter is outlined in Appendices 3.

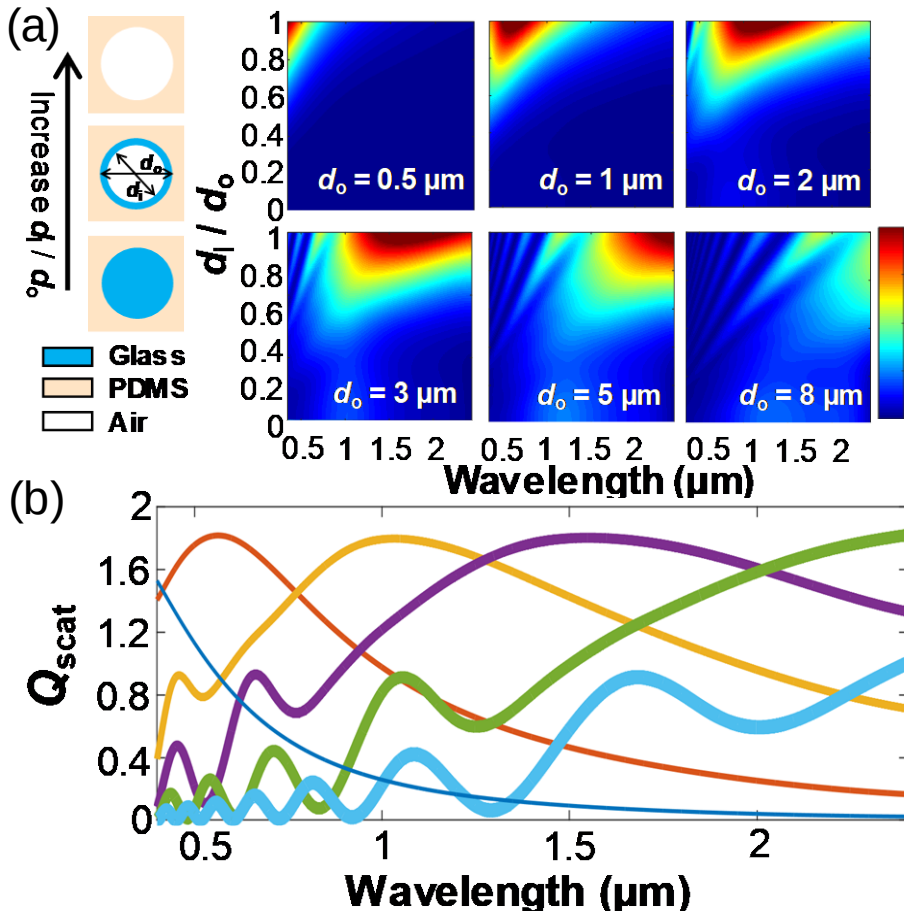

Figure 5.1 (a) The scattering efficiency (Q_{scat}) calculated using the Mie theory for individual hollow SiO_2 microspheres in PDMS background in the wavelength of 0.4-2.4 μm. The outer diameters d_o are varied from 0.5 to 8 μm, over which the scattering efficiency peaks redshift over the wavelength of interest. The shell thickness is indicated by the diameter ratio d_i / d_o, which corresponds to the diameter of the air core and SiO_2 microsphere respectively. By changing from a solid SiO_2 microsphere to porous PDMS, the scattering efficiency increases. (b) Q_{scat} as a function of wavelength for d_i / d_o = 0.9. The diameter d_o is color-labeled correspondingly. The scattering efficiency shows a peak with location and width corresponding to d_o. For d_o = 0.5 and 8 μm, the scattering efficiency does not show the peak in the wavelength from 0.4 to 2.4 μm.

5.3 Finite-difference Time-domain Simulation

Convergence tests were performed for different unit cell widths of 20 μm, 50 μm, 75 μm, and 100 μm, which further translates into width-to-thickness ratios of 0.2, 0.5, 0.75, and 1. Fixing the mesh size to 10 nm, no significant difference is observed for both reflectivity spectra and total reflectivity in the solar wavelength from 0.4 to 2.4 μm. To reduce computational costs, we chose

a unit cell size of 20×100 μm. Keeping the unit cell size to 100×100 μm and reducing the mesh size to 5 nm, again, no significant difference is seen between the spectral and total solar reflectivity. Thus, due to computational constraints, the mesh size of 10 nm was applied which works well with the minimum shell thickness down to 25 nm. Note that the mesh size was adjusted correspondingly if the minimum structure size decreases throughout this work.

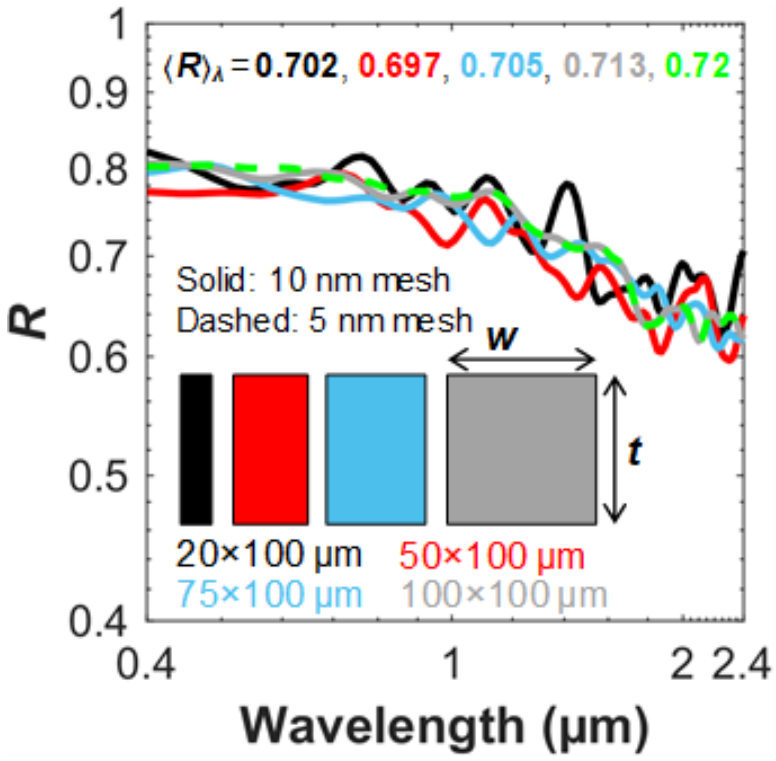

Figure 5.2 Convergence test results for 2D FDTD simulations using unit cell sizes of 20×100, 50×100, 75×100, and 100×100 μm and mesh sizes of 10 nm and 5 nm. Both spectral and total solar reflectivity change insignificantly under these different conditions.

5.4 Effects of the Shell Thickness and Material

We compute the spectral-average solar reflectivity $\langle \boldsymbol{R} \rangle_\lambda = \frac{\int \boldsymbol{R}(\lambda) d\boldsymbol{\lambda}}{\int d\boldsymbol{\lambda}}$ to compare composites with varying geometrical parameters. 2D FDTD simulations are performed in a 20 μm × 100 μm unit cell periodically repeated in $\boldsymbol{x}$ with perfectly matched layers (PML) in $\boldsymbol{y}$. Using wider unit cells or finer meshes change results insignificantly (See Fig. 5.2). We illuminate the unit cell with a

broadband (0.4-2.4 μm) unpolarized plane wave from below. Hollow microspheres are randomly generated in the unit cell [192] at the filling fraction (f.f.) of 55 vol%, which approaches the packing density of typical self-assembly structures [193,194]. The refractive indices of PDMS, SiO_2, and TiO_2 are from previous work [195,196]. To investigate the effect of shell thickness, we fix $\boldsymbol{d_o}$ of hollow SiO_2 microspheres to 1 μm (see the schematic in Figure 5.3). In Figure 5.3(a), $\langle \boldsymbol{R} \rangle_\lambda$ increases from 0.04 to 0.77 by changing $\boldsymbol{d_i} / \boldsymbol{d_o}$ from 0 to 1. When $\boldsymbol{d_i} / \boldsymbol{d_o} =$ 0.9, $\langle \boldsymbol{R} \rangle_\lambda$ peaks at 0.77, which outperforms that of solid microspheres and the porous PDMS. This could imply a significant reduction of coating thickness offered using a hollow microsphere structure. From refractive-index-contrast, $\langle \boldsymbol{R} \rangle_\lambda$ depends strongly on the air (n_{glass} - n_{air} is the largest contrast in this system) core size, $\boldsymbol{d_i}$, where larger $\boldsymbol{d_i}$ offers greater interface-to-volume ratio and thus enhanced scattering efficiency. The propagation of light is randomized due to repeated scattering by the air core which shortens photon transport mean free path [197] and hence strengthens reflection. To compare, we replace SiO_2 with TiO_2. The increased refractive-index-contrast lifts $\langle \boldsymbol{R} \rangle_\lambda$ significantly, ranging from 0.84 to 0.93 when varying $\boldsymbol{d_i} / \boldsymbol{d_o}$ from 0 to 0.9. $\langle \boldsymbol{R} \rangle_\lambda$ of 0.93 at $\boldsymbol{d_i} / \boldsymbol{d_o} =$ 0.7 is not only a 20.5% enhancement than that of hollow SiO_2 microspheres with $\boldsymbol{d_i} / \boldsymbol{d_o} =$ 0.9 but also an 21.5% increment than porous PDMS. We attribute the increased $\langle \boldsymbol{R} \rangle_\lambda$ to the additional light scattering induced by high-refractive-index shells. Interestingly, $\langle \boldsymbol{R} \rangle_\lambda$ of hollow SiO_2 microsphere with $\boldsymbol{d_i} / \boldsymbol{d_o} =$ 0.9 is only an 8.3% reduction from $\langle \boldsymbol{R} \rangle_\lambda$ of solid TiO_2 microspheres, making the former a promising low-refractive-index alternative for the latter considering its strong ultraviolet (UV) absorption and potential safety concerns [186]. Moving on to the effect of diameter variation (again see Figure 5.2 for schematics of hollow microspheres generated for FDTD simulations), we find that $\langle \boldsymbol{R} \rangle_\lambda$ increases with increasing $\boldsymbol{d_i} / \boldsymbol{d_o}$ even though $\boldsymbol{d_o}$ is not uniform (Figure 5.5). In Figure 5.3(b), for $\boldsymbol{d_i} / \boldsymbol{d_o} =$ 0.9, $\langle \boldsymbol{R} \rangle_\lambda$ generally decreases as the diameter variation extends towards larger

$\boldsymbol{d_0}$ and increases as the variation expands to the nanoscale. Notably, $\langle \boldsymbol{R} \rangle_\lambda$ drops by 8.3% from 0.84 to 0.77 as $\boldsymbol{d_0}$ varies from {0.5-1} to 0.5 μm; further increasing $\boldsymbol{d_0}$ to {0.75-1} and 0.75 μm leads to slight reflectivity reductions (to 0.825 and 0.815, respectively) while still maintaining the advantage of the varying- over uniform-diameter design. Hollow SiO_2 microspheres with the varying $\boldsymbol{d_0}$ induce scattering efficiency peaks located differently over the entire solar spectrum (Figure 5.1(a)); scattering efficiency dips associated with certain sizes are successfully compensated by others. Such a compensation mechanism is immediately obvious by comparing the solar reflectivity spectra, which is detailed in Figure 5.4. In 5.4(a), we can observe that hollow SiO_2 microspheres with varying diameters of 1-2 μm, 1-5 μm, and 1-8 μm show similar steadily decreasing solar reflectivity with increasing the wavelength, whereas the 1 μm hollow SiO_2 microsphere exhibits a higher solar reflectivity between the wavelength of 0.4 to 1.3 μm followed by a dip that is not recovered until the wavelength near 2 μm. In contrast, the 0.5-1 μm hollow SiO_2 microspheres achieve comparably high solar reflectivity between the wavelength of 0.4 to 1.3 μm compared to its 1 μm counterpart and, instead of a dip, shows a broad peak between the wavelength of 1.3 to 2.4 μm. This observation implies that solar reflectivity dip existing in uniform-diameter hollow microspheres can be compensated by employing hollow microspheres with varying diameters. Similar observation is again made in Figure 5.4(b) where the hollow microsphere material is changed to TiO_2. Notice that the reduced solar reflectivity for hollow TiO_2 microspheres near the wavelength of 0.4 μm is caused by the strong UV absorption, which is well-known for this material.

The diameter variation thus provides broadband solar reflectivity enhancement in the hollow SiO_2 microsphere composites. Note that the distribution of $\boldsymbol{d_0}$ is skewed towards smaller sizes (inset of Figure 5.3(b)), however, at the filling ratio of 55 vol%, we do not observe a significant

effect on the solar reflectivity from varying the current size distribution to a normal one. As shown in Figure 5.6, we compare the solar reflectivity for hollow SiO_2 microspheres with $\boldsymbol{d_0}$ of 0.5-1 μm, 1-2 μm, 1-5 μm, and 1-8 μm. When $\boldsymbol{d_0}$ is submicron, the normal size distribution and skewed size distribution lead to nearly identical solar reflectivity, while as $\boldsymbol{d_0}$ becomes larger, the discrepancy between the solar reflectivity of the two size distributions becomes greater (see Figure 5.6(b)). The accrued discrepancy can be readily explained by the reduced solar reflectivity in the wavelength range of 0.4 to 1 μm (see Figure 5.6(a)) for hollow microspheres following a normal size distribution. The solar reflectivity in this wavelength range is mainly contributed by the small size hollow microspheres, which is the minority in normal size distribution as the size is greater (e.g., $\boldsymbol{d_0}$ = 1-5 μm and 1-8 μm).

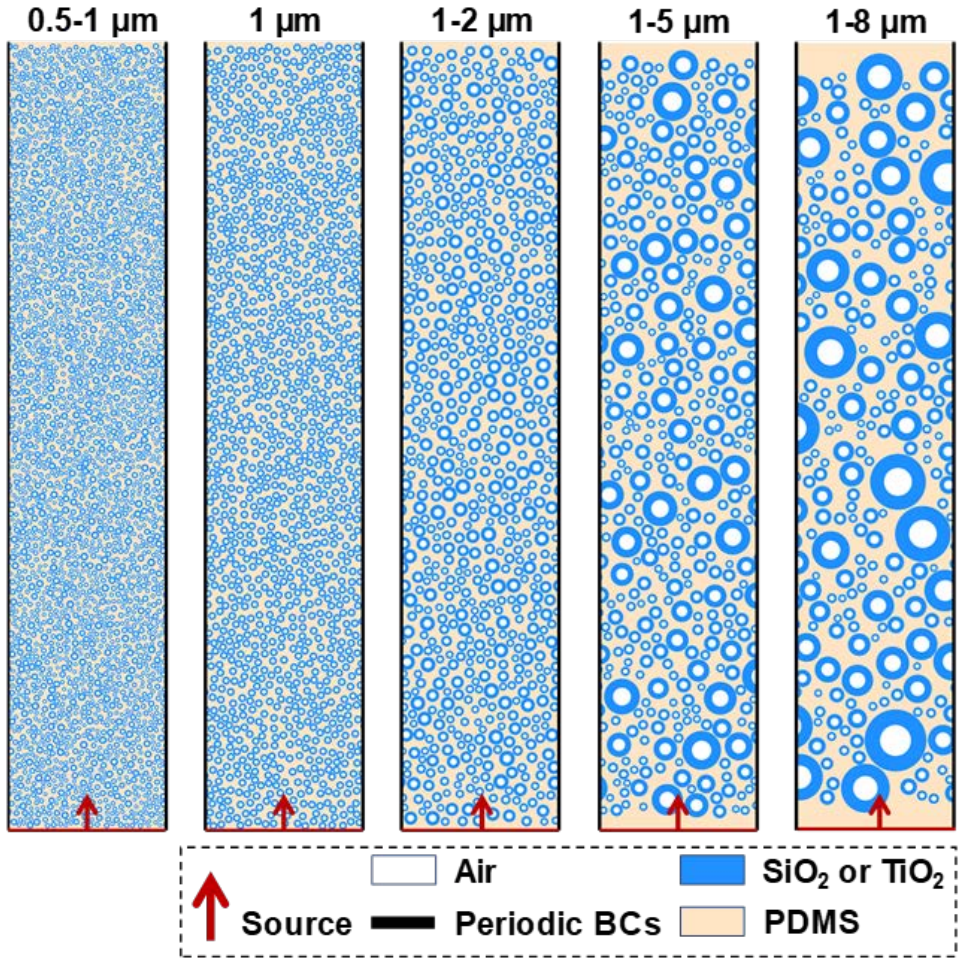

Figure 5.2 Representative schematics of hollow microsphere composites with d_o of 0.5-1 μm, 1 μm, 1-2 μm, 1-5 μm, and 1-8 μm generated for the FDTD simulation. The hollow microsphere's filling fraction is controlled to be 55 vol%. Each unit cell has a width of 20 μm and a thickness of 100 μm. The left and right boundaries are subject to periodic boundary conditions. A plane wave source (0.4-2.4 μm) illuminates the unit cell from the bottom with a reflection monitor behind it to collect the electromagnetic power that is reflected by the hollow microspheres. A transmission monitor is placed on the top boundary to collect the electromagnetic power that transmits through hollow microspheres. The microsphere materials are SiO_2 or TiO_2 (colored blue). The matrix is PDMS (colored light-orange). The hollow core is air-filled (colored white).

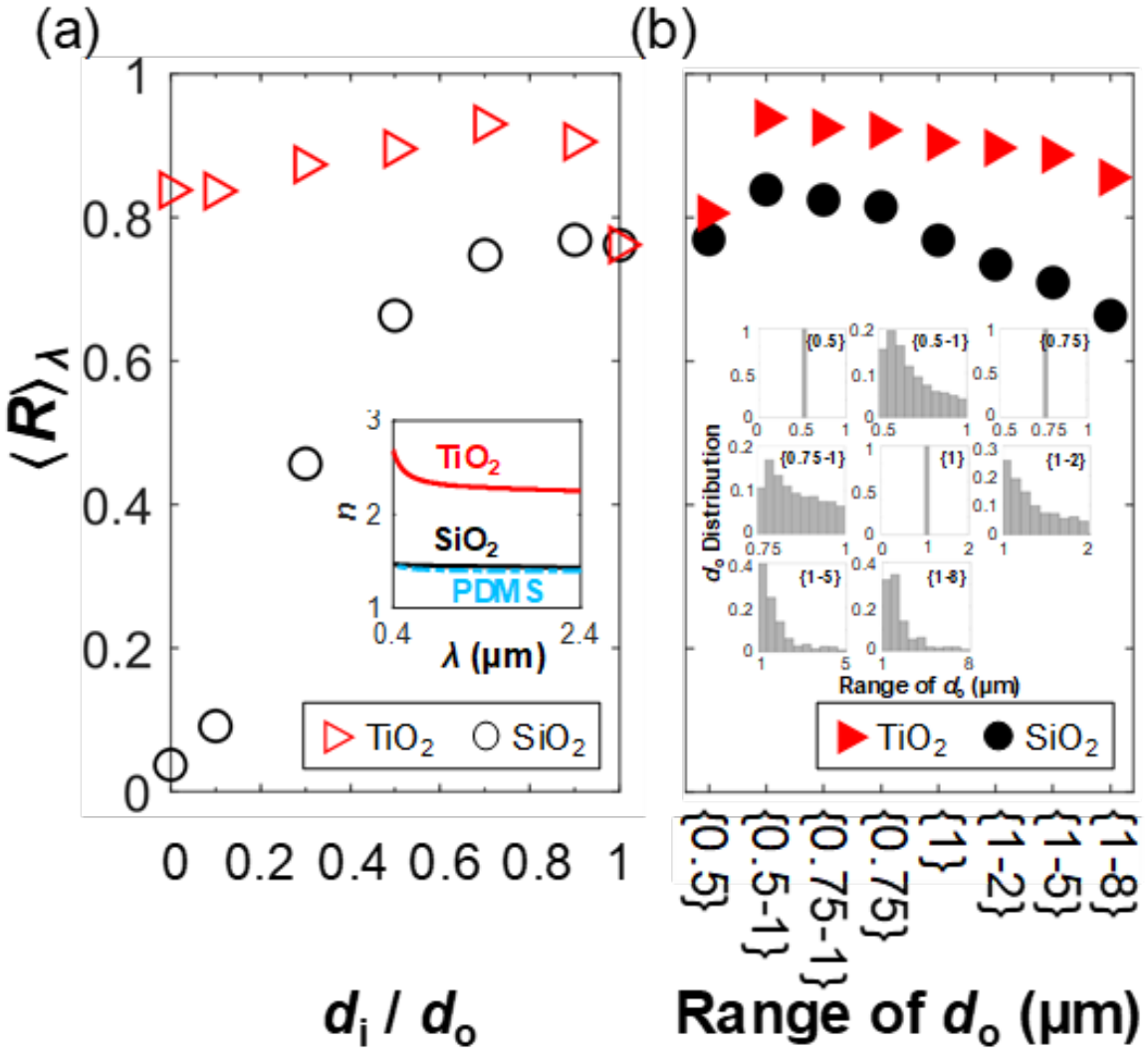

Figure 5.3 (a) Integrated reflectivity $\langle R \rangle_\lambda$ as a function of shell thickness for uniform-diameter hollow SiO_2 and TiO_2 microspheres with d_o = 1 μm in the wavelength of 0.4-2.4 μm. (b) $\langle R \rangle_\lambda$ of varying-diameter hollow SiO_2 microspheres with d_o ranges in {0.5-1}, {0.75-1}, {1-2}, {1-5}, and {1-8} μm. $\langle R \rangle_\lambda$ computed for the uniform-diameter microspheres, {0.5}, {0.75}, and {1} μm, are plotted for comparison. The shell thickness defined by d_i / d_o = 0.9 is studied.

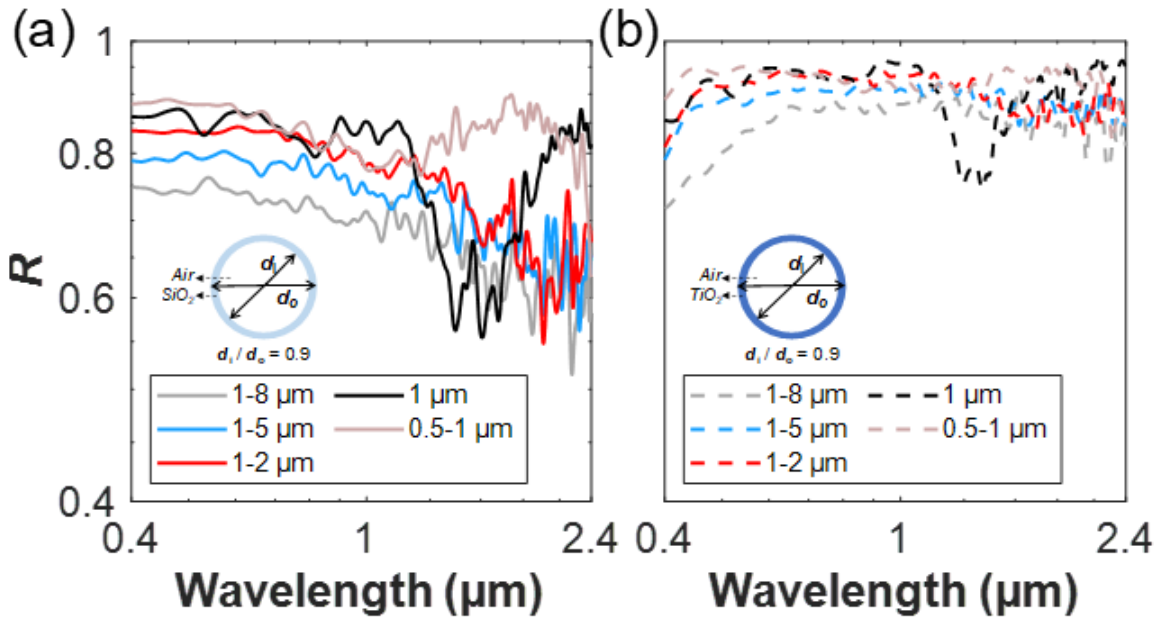

Figure 5.4 Solar reflectivity of hollow (a) SiO_2, and (b) TiO_2 microsphere composites with $\boldsymbol{d_i}$ / $\boldsymbol{d_o}$ = 0.9 with varying $\boldsymbol{d_o}$. The reflectivity spectra are smoothed using a Gaussian algorithm.

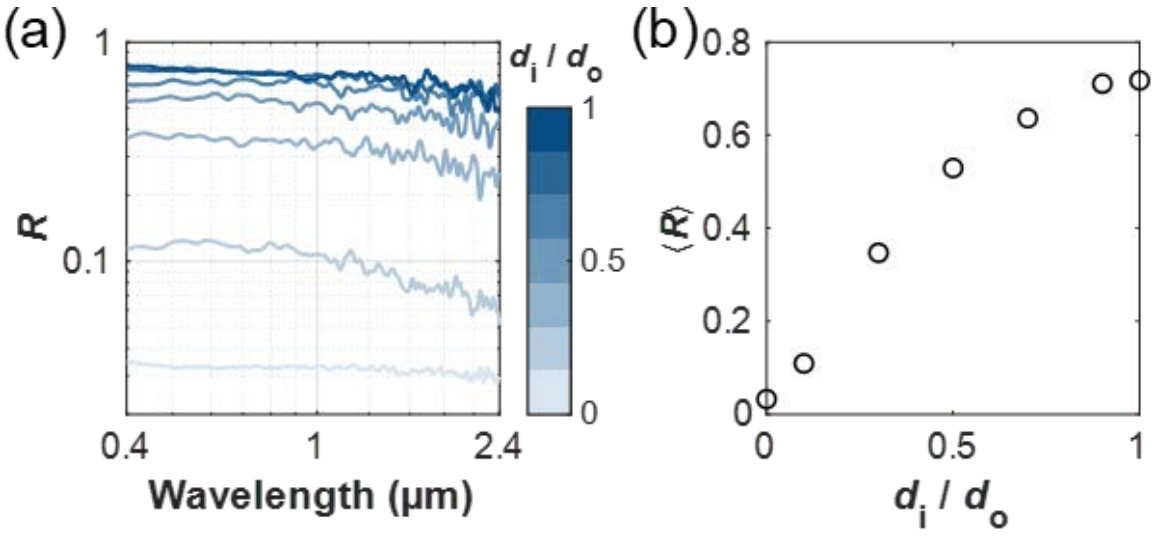

Figure 5.5 (a) Solar reflectivity of varying-diameter hollow SiO_2 microspheres-PDMS composites with $\boldsymbol{d_o}$ from 1 to 8 μm and shell thickness from 5% to 45% of $\boldsymbol{d_o}$. The reflectivity spectrum decreases in thickening the SiO_2 shell. (b) Integrated solar reflectivity of hollow SiO_2 microspheres with corresponding shell thickness in (a).

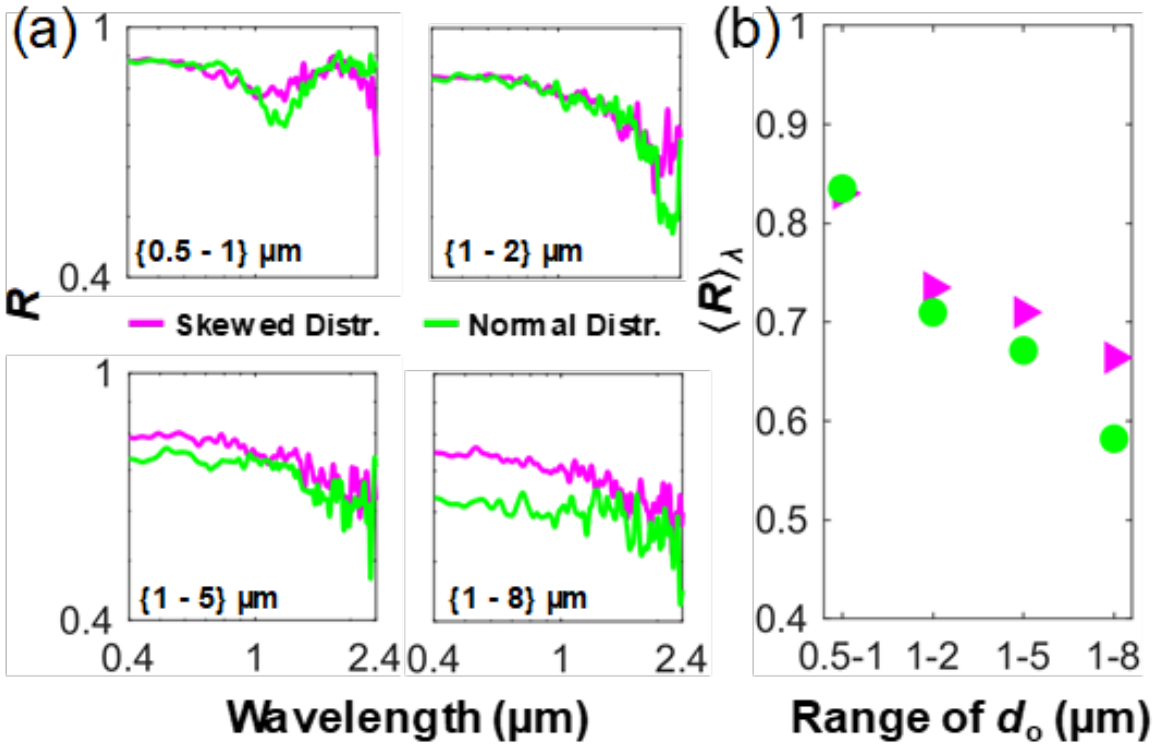

Figure 5.6 (a) Solar reflectivity spectra and (b) the total solar reflectivity for varying-diameter hollow SiO_2 microspheres whose sizes follow a normal or skewed distribution.

5.5 Effect of Diameter Variation

To explain the trend of $\langle \boldsymbol{R} \rangle_\lambda$ in Fig.2(b), we employ the total-field scattered-field source to illuminate randomly distributed hollow SiO_2 microspheres with varying $\boldsymbol{d_o}$ in a 20 μm × 20 μm unit cell (f.f. = 55 vol%) surrounded by PMLs. Statistics of $\boldsymbol{d_o}$ distribution (bottom left inset) are close to those in Fig.2(b). We compute the backscattering ratio $\boldsymbol{Q_b} / \boldsymbol{Q_f}$, where $\boldsymbol{Q_b}$ and $\boldsymbol{Q_f}$ are the scattering efficiency in the forward and backward directions defined by angular ranges [0, 180°) and [180°, 360°) from $+x$ direction (schematics in Fig.3). We selectively consider varying $\boldsymbol{d_o}$ distributions of 0.5 to 1 μm, 1 to 2 μm, 1 to 5 μm, and 1 to 8 μm, which for brevity will be referred to as {0.5-1}, {1-2}, {1-5}, and {1-8} hereafter. Uniform-diameter hollow SiO_2 microspheres with $\boldsymbol{d_o}$ of 0.5 and 1 μm (referred to as {0.5 and {1}) are included for comparison. The backscattering ratio of the composites {1-2}, {1-5}, and {1-8} with $\boldsymbol{d_i} / \boldsymbol{d_o} = 0.9$ share similar decreasing trend

while differing in magnitudes over the entire spectrum. Composites {0.5}, {0.5-1} and {1} yield comparable backscattering ratio in the visible spectrum, while in the near-IR range show similar major peaks/dips but contrasting amplitudes. Specifically, varying $\boldsymbol{d_o}$ distribution compensates the dip at $\boldsymbol{\lambda} \approx 1.2$ μm and lifts the peak near $\boldsymbol{\lambda} \approx 1.8$ μm. Notably, composites with smaller $\boldsymbol{d_o}$ achieve spectral-average backscattering ratio $\langle \boldsymbol{Q_b} / \boldsymbol{Q_f} \rangle_\lambda$ (bottom right inset), which could be due to stronger scattering by an increased number of scatterers as $\boldsymbol{d_o}$ decreases. Importantly, despite higher backscattering ratio from around 1 to 1.6 μm for the composite {0.5} than {0.5-1}, the former exhibits a significant reduction after 1.6 μm, resulting in higher $\langle \boldsymbol{Q_b} / \boldsymbol{Q_f} \rangle_\lambda$ which agrees well with the trend in Fig.2(b). We also selectively plot the electric field distribution for composites {0.5-1} and {1} at the backscattering ratio peaks and dips to reveal the optical behavior underlying the enhanced reflection. At $\boldsymbol{\lambda} = 1.81$ and 1.84 μm, greater electric field magnitude $|\boldsymbol{E}|$ in the backward direction indicates stronger backscattering, whereas at $\boldsymbol{\lambda} = 1.47$ and 2.33 μm, $|\boldsymbol{E}|$ is larger in the forward direction which indicates stronger forward scattering.

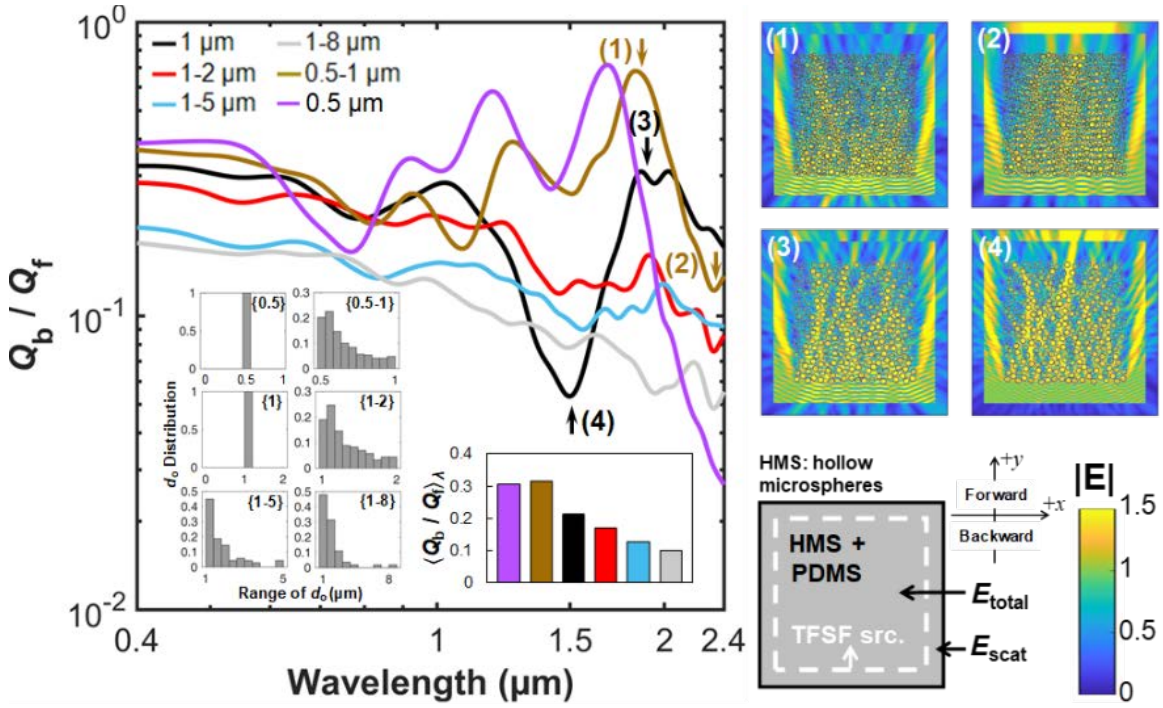

Figure 5.7 Wavelength-dependent backscattering ratio computed for varying-diameter hollow SiO_2 microspheres with d_i / d_o. The simulation is performed using 20 μm × 20 μm unit cells illuminated by the total-field scattered-field source in the wavelength of 0.4-2.4 μm. The statistical distribution of d_o is similar to those in Fig.2(b). Selected electric fields of uniform- (d_o = 1 μm) and varying-diameter (d_o = 0.5 to 1 μm) hollow SiO_2 microspheres with d_i / d_o = 0.9.

Hollow SiO_2 microspheres with thicker shells exhibit strikingly different scattering properties, as shown in Figure 5.8(a). The backscattering magnitude for the composites {0.5-1}, {1}, and {1-2} drop significantly from 0.4 to 1 μm wavelength range by almost an order of magnitude. The varying-dimeter hollow SiO_2 microspheres show a steadily decreasing backscattering ratio with increasing the wavelength, whereas the uniform-diameter hollow SiO_2 microspheres show a major dip (magnitude of the dip is on the order of 10^{-4}) in backscattering near the wavelength of 1 μm and climb back up to a peak (magnitude of the peak is on the order of 10^{-2}) near the wavelength of 1.6 μm. The backscattering magnitude greatly differs from that of the SiO_2 hollow microspheres with a thinner shell. In Figure 5.8(b), we again selectively plot the electric field distribution for the 1 μm hollow SiO_2 microspheres at the

frequencies of 1.05 μm and 1.6 μm. The electric field is mostly strong in the forward direction, indicating the backscattering strength is weak. Due to the significantly weakened backscattering, the thicker shell is not preferable for achieving a high solar reflectivity for SiO_2 hollow microspheres.

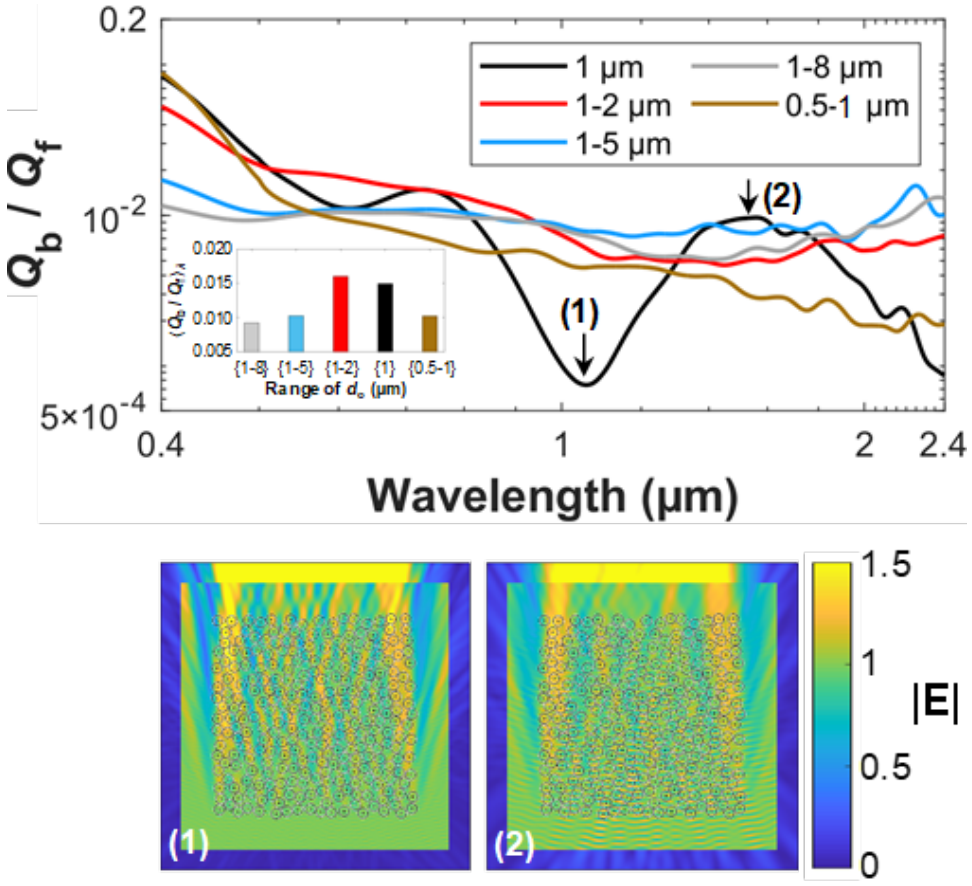

Figure 5.8 Backscattering ratio spectra smoothed by a gaussian algorithm and total backscattering ratio (inset) for varying-diameter hollow SiO_2 with $\boldsymbol{d_i}$ / $\boldsymbol{d_o}$ = 0.1 simulated using 20×20 μm unit cells illuminated by a total-field scattered-field source over the wavelength from 0.4 to 2.4 μm.

5.6 Identification of the Optimal Design

$\langle \boldsymbol{R} \rangle_\lambda$ and $\langle \boldsymbol{Q_b} / \boldsymbol{Q_f} \rangle_\lambda$ concurrently imply stronger solar reflection achieved by hollow SiO_2 microspheres with nanoscale $\boldsymbol{d_o}$. To reduce the computational cost, we compute $\langle \boldsymbol{Q_b} / \boldsymbol{Q_f} \rangle_\lambda$ for hollow SiO_2 microspheres with the varying and uniform diameter in the submicron scale while keeping $\boldsymbol{d_i} / \boldsymbol{d_o} = 0.9$. Depicted in Figure 5.9(a), $\langle \boldsymbol{Q_b} / \boldsymbol{Q_f} \rangle_\lambda$ for uniform-diameter hollow SiO_2 microspheres peaks at 0.5 μm and quickly decays towards both ends. Similarly, for varying-diameter hollow SiO_2 microspheres in (b), $\langle \boldsymbol{Q_b} / \boldsymbol{Q_f} \rangle_\lambda$ reaches comparable apexes for $\boldsymbol{d_o}$ ranging in {0.25-1} and {0.5-1} μm, whereas extending the range further towards smaller and larger sizes yields reduced backscattering. Specifically, shown in the inset, the two optimal varying-diameter designs slightly outperform the uniform-diameter design ($\boldsymbol{d_o} = 0.5$ μm) in $\langle \boldsymbol{Q_b} / \boldsymbol{Q_f} \rangle_\lambda$, which highlights the advantage of diameter variation. Yet we notice that in Figure 5.3(b), composite {0.5} has the lowest $\langle \boldsymbol{R} \rangle_\lambda$, differing from $\langle \boldsymbol{Q_b} / \boldsymbol{Q_f} \rangle_\lambda$. We could attribute this to the difference in the simulated unit cells, whereas the advantage of varying-diameter over uniform-diameter design in offering high $\langle \boldsymbol{R} \rangle_\lambda$ maintains and trends of $\langle \boldsymbol{R} \rangle_\lambda$ and $\langle \boldsymbol{Q_b} / \boldsymbol{Q_f} \rangle_\lambda$ for other diameters agree well. When $\boldsymbol{d_o}$ is uniform, the reduced $\langle \boldsymbol{Q_b} / \boldsymbol{Q_f} \rangle_\lambda$ could be due to narrowband scattering efficiency peaks at specific wavelengths, inferred by Fig.1; when $\boldsymbol{d_o}$ is varying, scattering efficiency peaks inherited to multiple sizes blend to induce a broadband enhancement. The optimal $\langle \boldsymbol{Q_b} / \boldsymbol{Q_f} \rangle_\lambda$ in (b) implies a competing effect between the increased number of scatterers due to decreased $\boldsymbol{d_o}$, which would lead to enhanced scattering, and the scattering efficiency, whose peak blueshifts with decreasing $\boldsymbol{d_o}$. Importantly, we consider only the range of $\boldsymbol{d_o}$ but not specific combinations, which relaxes the stringent requirement of precise control on size compositions that may be practically challenging.

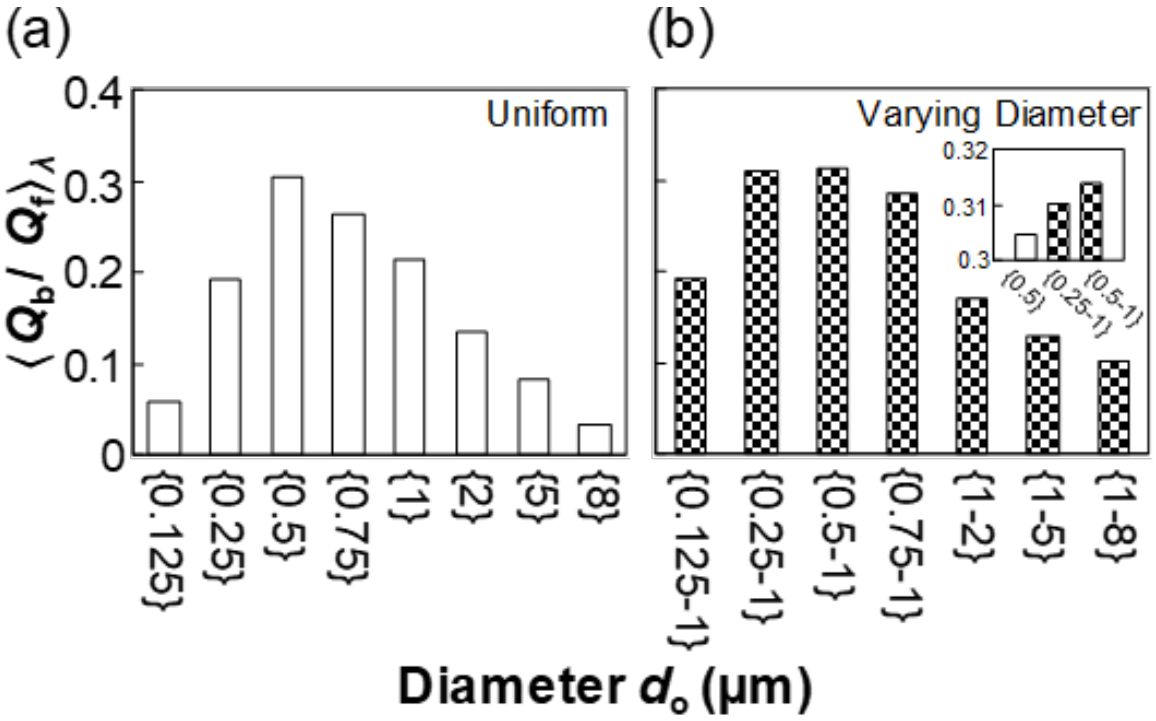

Figure 5.9 Spectral-average backscattering ratio $\langle Q_b / Q_f \rangle_\lambda$ of (a) uniform- and (b) varying-diameter hollow SiO_2 microspheres. Uniform-size hollow SiO_2 microspheres induces the highest backscattering ratio when d_o = 0.5 μm; hollow SiO_2 microspheres with varying d_o ranging in {0.25-1} and {0.5-1} μm provide comparably high backscattering ratios, which slightly outperform that of uniform-size ({0.5} μm). The inset plots $\langle Q_b / Q_f \rangle_\lambda$ for hollow SiO_2 microspheres with d_o of {0.5}, {0.25-1}, and {0.5-1} μm, respectively.

The average solar reflectivity $\langle R \rangle_\lambda$ presented in Figure 5.3 is computed based on an unweighted spectral averaging $\langle R \rangle_\lambda = \frac{\int R(\lambda) d\lambda}{\int d\lambda}$, where we focus on the wavelength range between 0.4 to 2.4 μm which accounts for 89% of the total solar irradiation power. The other 11% of the solar irradiation falls in ultraviolet wavelength smaller than 0.4 μm by 7% and near mid/long infrared wavelength greater than 2.4 μm by 4%. We next predict the weighted average solar reflectivity by assuming the solar reflectivity of the hollow SiO_2 microsphere composites in the UV and mid/long IR region to be from 0 to 1 and using the weighting coefficient of 7%, 44%, 45%, and 4% for each wavelength that the solar irradiation power spectrum covers. The prediction results are presented in Table 5.1. We can observe that the optimal designs that maximize the

weighted solar reflectivity $\langle \boldsymbol{R} \rangle_{\lambda}$ for both SiO_2 and TiO_2 microsphere materials are the varying diameter 0.5-1 μm. These results agree with the unweighted $\langle \boldsymbol{R} \rangle_{\lambda}$ reported in Figure 5.3 and validate our calculation that solely accounts for the wavelength from 0.4 to 2.4 μm, which is our main wavelength range of interest.

Table 5.1 Prediction of weighted average solar reflectivity $\langle \boldsymbol{R} \rangle_{\lambda}$ for SiO_2/TiO_2 hollow microsphere composites with uniform and varying diameters based on the solar irradiation power spectrum over the UV, NIR, IR, and mid/long IR regions. The percentage of solar irradiation power in each wavelength region is 7%, 44%, 45%, and 4%, respectively.

Average Solar Reflectivity Predictions					
Materials	Ultraviolet (0.2-0.4 μm)	Visible (0.4-2.4 μm)	Near-infrared (0.8-2.4 μm)	Infrared (2.4-4 μm)	Weighted $\langle \boldsymbol{R} \rangle_{\lambda}$
PDMS/SiO_2 HMS, $\boldsymbol{d_o}$ = 0.5 μm	0 – 1	0.84643	0.750794	0 – 1	0.710287 – 0.820287
PDMS/SiO_2 HMS, $\boldsymbol{d_o}$ = 0.5-1 μm	0 – 1	**0.867933**	**0.820803**	0 – 1	**0.751252 – 0.861252**
PDMS/SiO_2 HMS, $\boldsymbol{d_o}$ = 0.75 μm	0 – 1	0.874941	0.805485	0 – 1	0.747442 – 0.857442
PDMS/SiO_2 HMS, $\boldsymbol{d_o}$ = 0.75-1 μm	0 – 1	0.844019	0.744796	0 – 1	0.706527 – 0.816527
PDMS/SiO_2 HMS, $\boldsymbol{d_o}$ = 1 μm	0 – 1	0.850757	0.748068	0 – 1	0.710964 – 0.820964
PDMS/SiO_2 HMS, $\boldsymbol{d_o}$ = 1-2 μm	0 – 1	0.833492	0.710145	0 – 1	0.686302 – 0.796302
PDMS/SiO_2 HMS, $\boldsymbol{d_o}$ = 1-5 μm	0 – 1	0.788985	0.690024	0 – 1	0.657664 – 0.767664
PDMS/SiO_2 HMS, $\boldsymbol{d_o}$ = 1-8 μm	0 – 1	0.736486	0.645828	0 – 1	0.614676 – 0.724676
PDMS/TiO_2 HMS, $\boldsymbol{d_o}$ = 0.5 μm	0 – 1	0.910156	0.78035	0 – 1	0.751626 – 0.861612
PDMS/TiO_2 HMS, $\boldsymbol{d_o}$ = 0.5-1 μm	0 – 1	**0.936522**	**0.917099**	0 – 1	**0.824764– 0.934764**
PDMS/TiO_2 HMS, $\boldsymbol{d_o}$ = 0.75 μm	0 – 1	0.8749	0.8056	0 – 1	0.747476 – 0.857476
PDMS/TiO_2 HMS, $\boldsymbol{d_o}$ = 0.75-1 μm	0 – 1	0.905711	0.86135	0 – 1	0.786120 – 0.896120
PDMS/TiO_2 HMS, $\boldsymbol{d_o}$ = 1 μm	0 – 1	0.932751	0.897686	0 – 1	0.814369 – 0.924369
PDMS/TiO_2 HMS, $\boldsymbol{d_o}$ = 1-2 μm	0 – 1	0.91912	0.891917	0 – 1	0.805775 – 0.915775
PDMS/TiO_2 HMS, $\boldsymbol{d_o}$ = 1-5 μm	0 – 1	0.890493	0.887279	0 – 1	0.791092 – 0.902092
PDMS/TiO_2 HMS, $\boldsymbol{d_o}$ = 1-8 μm	0 – 1	0.835418	0.861358	0 – 1	0.755195 – 865195

Glass/TiO_2 HMS volume fraction is **55 vol%; PDMS/HMS composite thickness is **100** **μm***.

5.7 Discussions

To discuss, we do not consider UV or mid-infrared (mid-IR) spectra as they only account for 11% of solar irradiation [198]. Additional insight into spectral contributions is obtained by computing $\langle \boldsymbol{R} \rangle_{\lambda}$ in UV (7%), visible (44%), near-IR (45%), and mid-IR (4%) by their percentages in solar power (100%). For the optimal hollow SiO_2 microspheres with $\boldsymbol{d_o}$ of {0.5-1} μm, we

assume $\langle \boldsymbol{R} \rangle_{\lambda,\,\mathbf{UV}}$ and $\langle \boldsymbol{R} \rangle_{\lambda,\,\mathbf{mid\text{-}IR}}$ to be from 0 to 1, and yield $\langle \boldsymbol{R} \rangle_{\lambda,\,\mathbf{vis}} = 0.868$ and $\langle \boldsymbol{R} \rangle_{\lambda,\,\mathbf{near\text{-}IR}} = 0.821$, respectively, leading to a weighted $\langle \boldsymbol{R} \rangle_{\lambda}$ from UV to mid-IR ranging from 0.751 to 0.861. For $\boldsymbol{\lambda}$ from 0.4 to 2.4 μm, higher $\langle \boldsymbol{R} \rangle_{\lambda}$ is expected for composites thicker than 100 μm due to decreased transmissivity led by the addition of materials. In this regard, we simulated SiO_2 hollow microspheres with $\boldsymbol{d_0}$ ranging in 1 to 8 μm for varying unit cell thicknesses including 50, 100, 150, and 200 μm. While the simulation is performed for this specific range of $\boldsymbol{d_0}$ for reducing the computational cost, the conclusion is readily applicable to the microsphere composites with other $\boldsymbol{d_0}$ despite being uniform or varying. Shown in Figure 5.10, as the thickness increases, the spectral solar reflectivity decreases steadily with increasing the wavelength. The solar reflectivity magnitudes for each thickness are clearly separated, indicating that as more SiO_2 hollow microspheres are packed into the composite the solar reflection becomes stronger. Because neither SiO_2 nor PDMS is strongly absorptive in the wavelength range of 0.4 to 2.4 μm, the reflectivity $\boldsymbol{R}$ and transmissivity $\boldsymbol{T}$ follow $\boldsymbol{R} = 1 - \boldsymbol{T}$. Thus, as the SiO_2 hollow microsphere composite becomes thicker, the solar reflectivity would increase due to the reduced transmissivity, given none of the composite materials absorbs significantly in the solar wavelength.

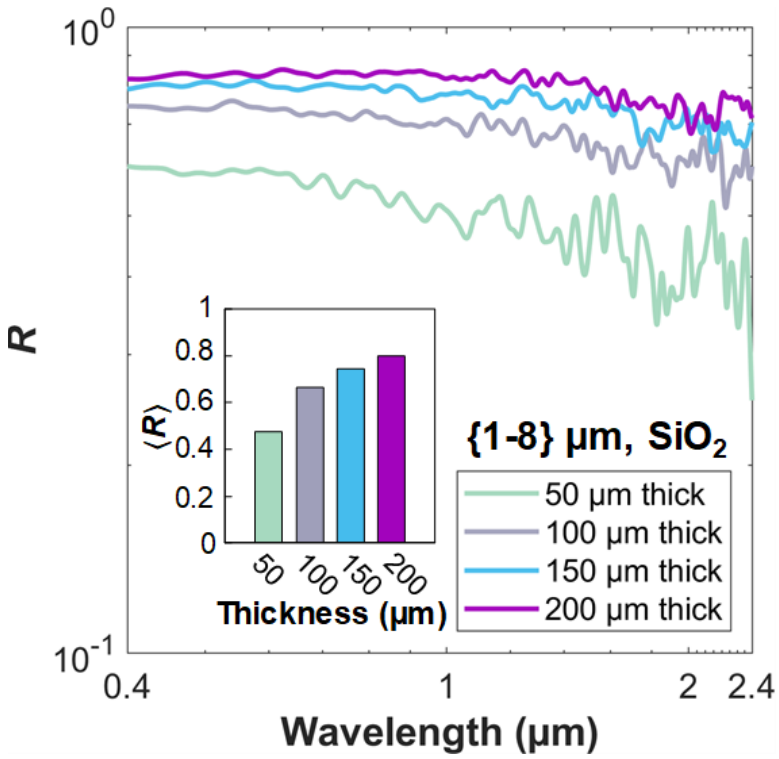

Figure 5.10 Spectral-dependent and average reflectivity from the wavelength of 0.4 to 2.4 μm for the varying-diameter composite {1-8} with the thickness of the unit cell varying from 50 to 200 μm. Both the spectral and average solar reflectivity show increased magnitude for the thicker unit cell.

For λ smaller than 0.4 μm, we expect high UV reflectivity from hollow SiO_2 microspheres thanks to the sizes comparable with λ in varying diameter distributions, whereas TiO_2 microspheres would suffer from strong UV absorption. For wavelengths greater than 2.4 μm, $\langle \boldsymbol{R} \rangle_\lambda$ for both SiO_2 or TiO_2 hollow microspheres would drop significantly due to increased absorptivity/emissivity. One could adjust the range of varying diameters to achieve solar reflectivity modulation according to the need. Generally, hollow microspheres with varying diameters defined by ranges without fine-tuning specific size compositions discussed here will benefit applications where broadband optical responses are desired.

5.8 Conclusions

We have studied the solar reflectivity in the 0.4-2.4 μm wavelength range of solid and hollow microspheres with the diameter varying from 0.125 to 8 μm using Mie theory and FDTD simulations. SiO_2 and TiO_2 are considered as low- and high-refractive-index microsphere materials while the PDMS is considered as a polymer matrix. Our analysis has shown that hollow microspheres with a thinner shell are more effective in scattering light, compared solid microspheres, and lead to a higher solar reflectivity up to 20 times. The high scattering efficiency, owing to the large interface density, in hollow microspheres allows low-refractive-index SiO_2 to have a high solar reflectivity of 0.77, which is only 8.3% less than that of solid TiO_2 microspheres. When the diameter is uniform, 0.75 μm SiO_2 hollow microspheres provide the largest solar reflectivity of 0.81. When the diameter is varying, the random-distributed 0.5-1 μm SiO_2 hollow microspheres provide the largest solar reflectivity of 0.84. The effect of varying diameter is further supported by the backscattering ratio, where hollow SiO_2 microspheres with 0.5-1 μm diameters achieve the strongest backscattering among all studied designs. These findings will guide the optimal designs of microsphere composites and hierarchical materials for optical and thermal management systems.

CHAPTER 6: CONCLUSIONS AND SUGGESTIONS

6.1 Summary

In summary, this dissertation described the transport of phonons and photons in nanoporous structures and demonstrated their potentials for thermoelectric materials, phononic topological insulators, and radiative cooling coating materials.

Regarding the particle-like phonon transport, Monte Carlo ray tracing models have been developed to understand the phonon-boundary scattering phenomena in complex multi-dimensional Si nanoporous structures with the presence of multiple geometrical parameters. Ray tracing models for both 2D and 3D have been validated against various experimental and computational results in the literature. Specifically, the experimental data for periodic and aperiodic Si nanomeshes at temperatures higher than 14 K and periodicity greater than 100 nm verified the thermal conductivity calculation performed by 3D ray tracing simulations and the assumption of phonon particle-like transport in such Si nanoporous structures under such conditions. This work highlighted 2D ray tracing simulation results for Si nanoporous structures of varying pore shapes, alignments, and pore size distributions and focused on the phonon transport in the in-plane direction. The neck size has been identified as the key mechanism for understanding thermal conductivity reduction in Si nanoporous structures with identical porosities. Specifically, asymmetric pore shapes are more effective in reducing the thermal conductivity due to localized heat fluxes at the neck. Hexagonal-lattice pore distribution is more effective in reducing the thermal conductivity than the squared-lattice pore distribution due to blocking of phonon line of sight; alternative pore size distributions are more effective in reducing the thermal conductivity than uniform pore size distributions because of the limited phonon line of sight as well (Chapter 2). Asymmetric nanopores have shown possibilities of realizing thermal rectification even with

fully diffuse pore boundaries. A rectification ratio of up to 13 could be achieved by the optimally designed structure and controlled phonon injection angle (Chapter 3). The simulation results presented in Chapters 2 and 3 improved the understanding of phonon-boundary scattering phenomena in complex Si nanoporous structures and will guide the future optimal design of thermoelectric energy harvesting systems and thermal directional control devices.

Regarding the phonon wave-like transport, the current doctoral research has developed a unique six-petal holey Si design for realizing the intriguing phononic topological insulator. Submicron periodicity enabled working frequencies up to the GHz range. By simple geometrical modifications, the six-petal holey structure induced the zone-folding effect and demonstrated the topological phase transition, evident by the inversion of bands and vibrational modes computed by the FEM simulations. The emergence of topologically-protected edge states was confirmed by computing phononic band structures of a supercell joining a trivial and non-trivial phononic crystal with optimally tuned geometries. The full-scale FEM simulations successfully demonstrated the backscattering-immune elastic wave transmission greater than 90% with even with the presence of geometrical defects including a cavity, a lattice disorder, and complicated domain walls involving up to 14 sharp bends. The six-petal design intrinsically avoids potential fabrication uncertainties including the widely-seen rounding effect in the lithographical process. The design provided robustness to uniform over- and under-sizing errors up to 11% and 6%, respectively; even with randomly distributed and mixed over-sizing errors, the design was proven to be robust unless the errors were closed to each other in geometries. The above topological properties were successfully shown for both in-plane and out-of-plane elastic waves. The experimental validation was highly challenging at the moment due to the limited nanofabrication capability and on-chip measurement capability at GHz frequencies. However, the simulation results have clearly shown

the signatures of topological edge states and the backscattering-immunity. The experimental investigation could be expected to be performed in the future as technology advances. The results presented in this dissertation offered a detailed understanding of the relationship between geometry and topological properties and will pave the way for the design of future phononic circuits (Chapter 4).

Regarding the photon transport in nanoporous composite materials, the current dissertation presented detailed theoretical and numerical computation results for the high solar reflectivity achieved by hollow dielectric microspheres embedded in a PDMS matrix. Such disordered media have far-reaching applications in the radiative thermal management and the effectiveness of the investigated system in radiative cooling had been experimentally verified in our previous work. The current doctoral research focused on offering a fundamental perspective to the experimental observation of solar reflectivity enhancement realized by combining hollow microspheres with varying diameters that form a hierarchical system. The Mie theory and FDTD simulations showed that, for SiO_2 and TiO_2 shell materials, a thin shell thickness was more effective in scattering the light, compared to solid microspheres, and the high scattering efficiency was attributed to greater interface density that allows low-refractive-index materials to have high solar reflectivity. The FDTD simulations identified optimal designs for achieving high solar reflectivity. Specifically, for uniform-diameter hollow SiO_2 microspheres, a diameter of 0.75 μm realizes the highest solar reflectivity of 0.81, whereas, for vary-diameter hollow SiO_2 microspheres, a diameter range of 0.5-1 μm yielded the highest solar reflectivity of 0.84. The solar reflectivity could be driven even higher by increasing the thickness of the composite or introducing other shell materials that induces greater refractive-index-contrast. The presented computational results identified the key mechanisms of phonon and photon transport in various nanoporous structures and provided

physical insights into the controlled thermal and wave transport phenomena. The results will guide the future optimal design of optical and thermal management systems (Chapter 5).

6.2 Suggestions for Future Works

Nanoporous structures have received great attention in controlling the thermal and wave transport and are attractive for thermoelectric materials, topological insulators, and radiative cooling coating materials. My doctoral work has improved the understanding of multi-dimensional phonon-boundary scattering phenomena in complex geometries, the relationship between geometry and the topological properties induced by phonon transport in the form of elastic waves, and the optical properties of uniform- and varying-diameter hollow microsphere composites that lead to a high scattering efficiency of light (photon) and high solar reflectivity. There are, however, challenges and unclear understanding remained to be coped with and deciphered.

6.2.1 Experimental Demonstration of Six-petal Holey Si Topological Insulators

An experimental demonstration on the six-petal holey Si-based phononic topological insulators discussed in Chapter 4 can be performed. A potential experimental setup for measuring the elastic transmission is depicted in Figure 6.1(a). The setup is consisting of a piezoelectric transducer to excite the elastic wave at the input port, and a network analyzer to record the signal at the output port. Post-processing will lead to elastic wave transmission, $T(\omega) = 20\log(\Phi_{output}(\omega)/\Phi_{input}(\omega))$, where $\Phi(\omega)$ represents the elastic power spectral density. The piezoelectric transducer can be either a disk connected to a tiny Tungsten probe whose tip will be in contact with the topological insulator sample or an on-chip integration realized by nanofabrication. To detect the displacement field caused by the elastic wave propagation along the domain way between two topologically distinct domains, a laser vibrometer can be potentially included.

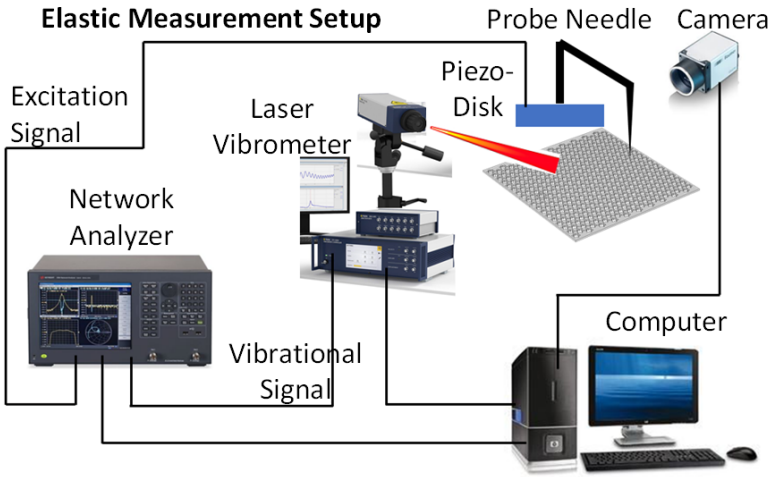

Figure 6.1 An experimental setup that can be potentially employed to characterize the phononic topological insulator. An excitation signal will be generated by a network analyzer, and the excitation will be implemented on the sample by a Tungsten probe needle. The vibrational signal that carries the information about the displacement field in the sample will be captured by a laser vibrometer and recorded by the network analyzer.

6.2.2 Topological Insulators in Three-Dimension

It is of great interest to expand the unprecedented transport capabilities and the unmatched tolerance to defects of topological insulators from two-dimensional (2D) to three-dimensional (3D) systems, where more complex transport phenomena will be involved and will open opportunities for controlling the wave propagation in higher dimensions. While in 2D systems the topological phase transition featured the formation of Dirac cones and breaking of either time-reversal (T) symmetry or parity inversion (P) by even an infinitesimal perturbation, in 3D systems the Dirac cone-based phase transition is a robust phase of Weyl points, and the Weyl points can only be created or eliminated by pair-annihilations and pair-generations of Weyl points of opposite chiralities, which usually requires strong perturbation. The existence of Weyl points in 3D photonic crystals was first shown theoretically possible by breaking both the P- and T-symmetry and then experimentally demonstrated in a 3D waveguide array structure by breaking the inversion symmetry. As preliminary work, we numerically investigate a 3D topological insulators design by

implementing a 3D hexagonal lattice structure using acoustic resonators. Figure 6.2 shows preliminary results based on polymer-air structures where each resonator is an air-filled six-petal cavity with polymer walls being an acoustic hard boundary. The geometrical parameter of each resonator is $\boldsymbol{h_t} = 0.5\boldsymbol{a}$ and $[\boldsymbol{r_i}, \boldsymbol{r_o}, \boldsymbol{d_{io}}] = [0.26\boldsymbol{a}, 0.13\boldsymbol{a}, 0.34\boldsymbol{a}]$. The coupling between each pair of nearest-neighboring resonators in the ***xy***-plane is provided by the neck while coupling along ***z***-direction is offered by a central cylindrical rod with a height $\boldsymbol{h_c} = 0.25\boldsymbol{a}$. By choosing a unit cell of two stacked identical resonators as $\boldsymbol{a}$ = 8.7 mm, the calculated phononic band structure shows that the projection of bulk bands onto ***xy***-plane is a nodal line along **K**-**H** (**K**, **H** are high-symmetry points) and that a Dirac cone formed at $\boldsymbol{f}$ = 16.7 kHz. To form a double Dirac cone, we expand the original unit cell to induce a zone-folding effect. The simulated band structure has two dispersive bands meeting at a linear band-crossing point, forming a four-fold degeneracy at the high-symmetry point **H**. To open a bandgap, we vary $\boldsymbol{r_i}$ to introduce two types of six-petal resonators obeying a glide symmetry. By increasing $\boldsymbol{r_{i1}}$ to 2.64 mm and decreasing $\boldsymbol{r_{i2}}$ to 1.88 mm when keeping all other geometrical parameters the same, we change the coupling strength in the ***xy***-plane, which leads to the original four-fold degeneracy point to break into two pairs of two-fold degenerate bands; this leaves a bulk bandgap open in-between and enables 3D topological insulators.

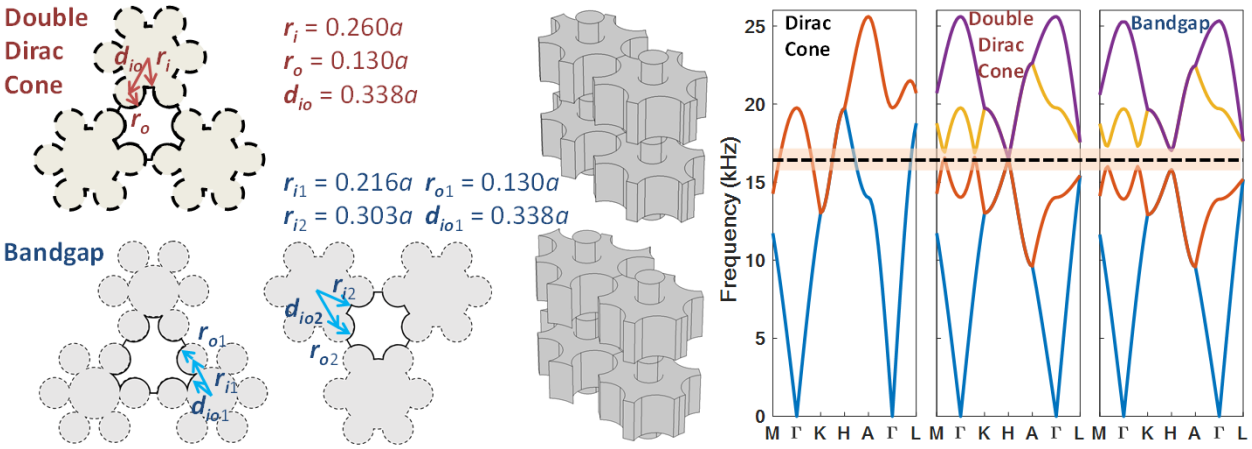

Figure 6.2 3D design of phononic topological insulators and preliminary computations of polymer-air structures that induce a double Dirac cone and open a bulk bandgap. To form a double Dirac cone, all four resonators in the expanded unit cell are designed to be the same. To open a bulk bandgap, two types of resonators are created by increasing and decreasing $\boldsymbol{r}_i$ to $\boldsymbol{r}_{i1}$ and $\boldsymbol{r}_{i2}$. For $\boldsymbol{a}$ = 8.7 mm, the phonon band structures are computed, and the band inversion process is confirmed. When there is a unit cell consisting of a monolayer of identical resonators, we observe a nodal line with two-fold degeneracy. By expanding the monolayer unit cell to a double-layer one, we induce a zone-folding effect and realize a double Dirac cone at 16.7 kHz. By modifying the expanded unit cell, a bulk bandgap forms at 16-17 kHz.

To demonstrate the emergence of topologically-protected surface states, we build a supercell and simulate its phononic band structure. Figure 6.3 shows the preliminary results with a supercell that is finite along the y-direction, containing 11 expanded unit cells with different resonators (e.g., with $\boldsymbol{r}_{i1}$ and $\boldsymbol{r}_{i2}$). We introduce a domain wall where two bulk phononic crystals on each side exhibit a mirror-like symmetry. Periodic boundary conditions are applied on the ***xz***- and ***yz***-plane. The simulated band structures show that two pairs of topological pseudospin-valley states are located between a bandgap spanning from 16 kHz to 17 kHz. We selectively plot in Figure 6.3(c) the acoustic pressure fields for two pairs of frequencies near the high-symmetry point $\tilde{\boldsymbol{\Gamma}}$. The acoustic pressure distributions are opposite in phase for the frequencies of 16.64 kHz and 16.68 kHz at $\boldsymbol{k_x a/\pi}$ = 1.25, indicating opposite group velocity of the acoustic wave and pseudospin directions. Similar opposite acoustic pressure distribution can be seen at $\boldsymbol{k_x a/\pi}$ = 5.25. To demonstrate phononic wave transmissions along topologically-protected domain walls, full-field numerical

simulations are performed. The preliminary results in Figure 6.3(d) shows that the acoustic pressure distribution is highly-localized to the domain wall (yellow-dashed curve) from the source (excitation is applied at the red-star mark) to the output (at the end of the yellow-dashed curve on the right) when an acoustic wave is excited at 17 kHz. Figure 6.3(e) shows the case where the domain wall is a zig-zag path. Again, the acoustic wave propagates in the proximity of the domain wall, detouring two sharp bends of 60° in a near backscattering-immune manner.

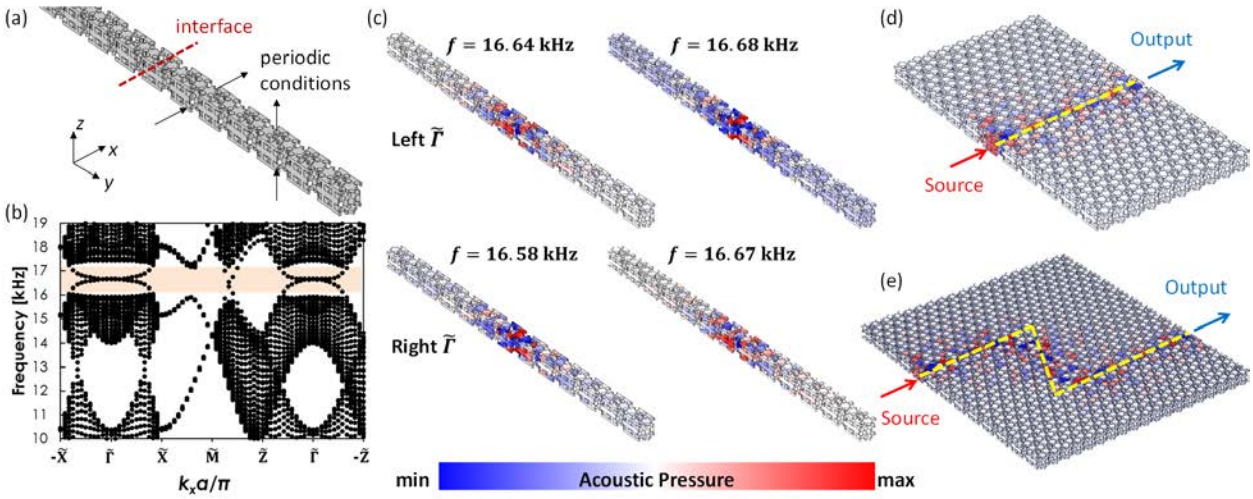

Figure 6.3 Preliminary computations of 3D topological insulators. (a) A supercell consists of 11 modified expanded unit cells forming an interface (red-dashed line). Periodic boundary conditions are applied in ***xy*** and ***yz*** planes. (b) The projected bulk band structure of the supercell. Two pairs of pseudospin-valley states can be observed in the bulk bandgap at 16-17 kHz. These two pairs of valley states are topologically-protected and have opposite pseudospin directions. (c) The acoustic pressure fields at selected reduced wavenumber $\boldsymbol{k_x a/\pi}$ of 1.25 (near the point $\tilde{\boldsymbol{\Gamma}}$ to the left of point $\tilde{\mathbf{M}}$) and 5.25 (near the point $\tilde{\boldsymbol{\Gamma}}$ to the right of point $\tilde{\mathbf{M}}$). (d) Acoustic wave transmissions along a straight domain wall, and (e) a zig-zag domain wall in the ***xy***-plane. The acoustic waves in both cases are excited from the sources at 17 kHz, and their transmissions are topologically-protected with negligible backscattering to the output.

6.2.3 Higher-order Topological Insulators and the Corner States

Higher-order topological insulators have become one of the frontiers in the research of topological matters. To explore this new class of topological insulators, the topological corner state, which signifies the existence of higher-order topological phenomena, can be investigated in the future. Based on the bulk-boundary correspondence, topological insulators of an order N are known to have (N-1)-dimensional boundary states, and second-order topological insulators are known to have no (N-1)-dimensional boundary states but (N-2)-dimensional ones. In other words, a 2D second-order topological insulator will have topologically-protected 0D corner states. The corner states have been studied in mechanical and electromagnetic systems with square lattices exhibiting topological properties based on the quantization of quadruple moments. The concept has been extended to Kagome lattices that have a non-trivial bulk topology characterized by quantized Wannier centers. To provide a general description of the concept, in Figure 6.4, a triangular-lattice with cylindrical air-filled resonators connected by thinner cylindrical rods between nearest-neighbors shows the acoustic pressure distributions for the (a) corner, (b) edge, and (c) bulk states. The three states are separated by frequencies in the phononic band structure. Depending on the bulk topology, all modes will be confined to the bulk region if the bulk topology is trivial, whereas edge or corner states will emerge if the bulk topology is non-trivial. The positions of the corner states agree well with the Wannier centers of the structure. It is also possible to make the corners be topologically-protected local resonance points by changing the shape of corners. The investigation of corner states in higher-order topological insulators will open possibilities of confining sound, elastic, or even heat waves at corners that are attractive for particle trapping or locally enhancing or sensing the phononic field.

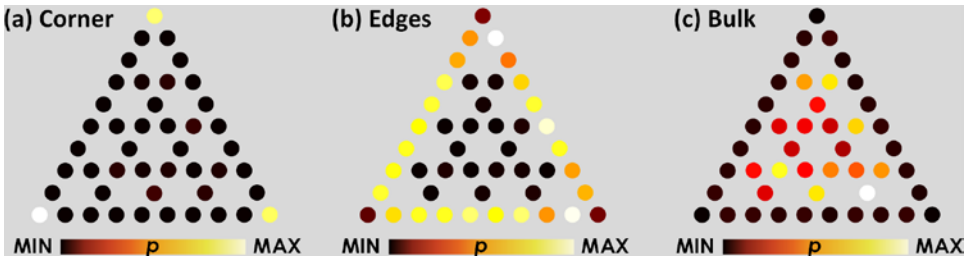

Figure 6.4 A general description of the (a) corner, (b) edge, and (c) bulk state supported by a triangular-lattice of air-filled cylindrical resonators connected by thinner cylindrical rods between the nearest-neighbors. The acoustic pressure distribution identifies the three states excited at varying frequencies and confined at different regions of the structure, where the position of corner states agree with Wannier centers.

6.2.4 Complete or Near-complete Solar Reflection

While it has been experimentally demonstrated recently that composites with varying-diameter glass bubbles in a PDMS matrix having micrometer thick can achieve a solar reflectivity over 90% and show significant radiative cooling temperature reduction, the most optimal cooling performance has not yet reached due to the incomplete reflection of the solar irradiation. Though increasing the composite thickness may have a marginal enhancement of solar reflectivity, a thicker composite also loses the merit of film flexibility which can be important as a coating for the non-flat building exterior. Numerically optimizing the distribution and sizes of the glass bubbles may not be a feasible approach due to the computational cost. The exploration of other bubble materials, those which induce greater refractive-index-contrast and exhibit insignificant UV absorption (TiO_2 is not a good choice here though it has a much higher refractive index than glass), could benefit the development of solar reflector that can reflect solar irradiation completely or near completely.

6.2.5 Characterization of Thermal Transport in Symmetric and Asymmetric Si Nanoporous Structures

In-plane thermal conductivity measurements can be performed to demonstrate the key findings discussed in Chapter 2. Potential experimental samples are illustrated in Figure 6.5. By

comparing the thermal conductivity of squared-lattice circular pores, in (b), and squared-lattice of triangular pores, in (c), with identical porosity, the effect of pore shapes can be shown. By measuring the hexagonal-lattice circular pores, in (a), and compare the thermal conductivity of that of the squared-lattice pores, the effect of pore alignments can be characterized. The effect of pore size distributions of alternating and uniform schemes can be compared by measuring potential samples shown in (d) and (e). Out-of-plane thermal conductivity can be characterized using the 3ω technique as well to complete the understanding of the thermal conduction of Si nanoporous structures discussed in this dissertation. The potential experimental setup for the in-plane and out-of-plane thermal conductivity measurements is shown in Figure 6.6 (a) and (b), respectively.

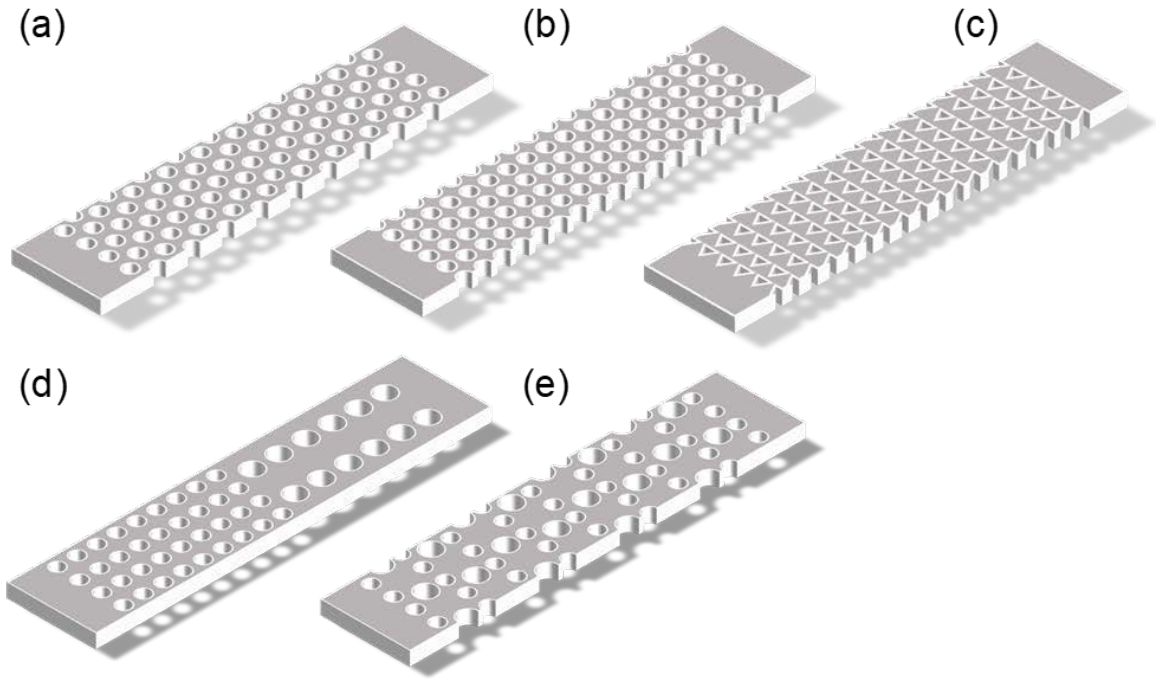

Figure 6.5 Schematics of potential experimental samples for thermal conductivity measurements of Si nanoporous structures having (a) hexagonal-lattice circular pores, (b) squared-lattice circular pores, (c) squared-lattice triangular pores, (d) circular pores following a uniform pore size distribution, and (e) circular pores following an alternating pore size distribution from small to large pores. Note that the dimensions in (a)-(e) are for illustration purposes only and do not reflect the real geometries of samples in practice.

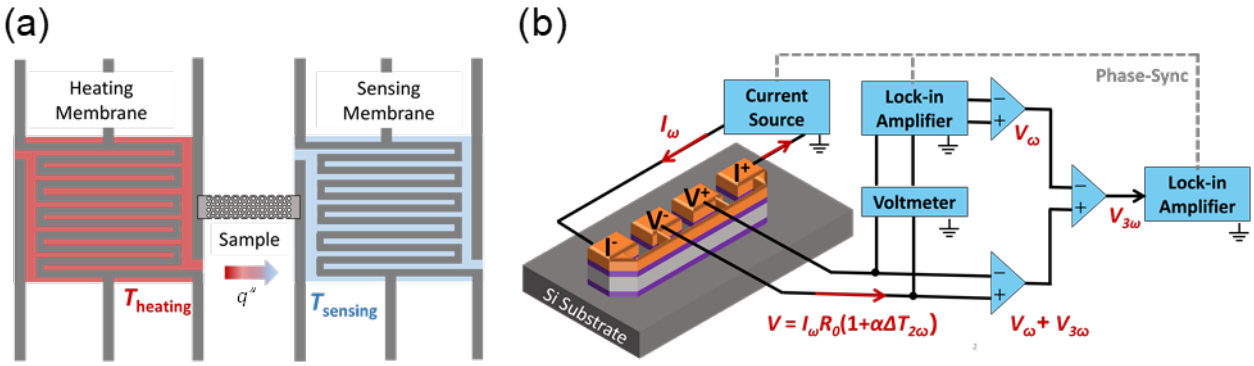

Figure 6.6 Potential experimental setup for the (a) in-plane and (b) out-of-plane thermal conductivity measurements.

Appendices

1. Thermal Conductivity Modeling

We start with the internal energy *U* which can be expressed as

$$U = \int_0^{\omega_0} \hbar\omega \, f_{BE}(\omega, T) D(\omega) d\omega \tag{1}$$

where ω_0 is a cut-off frequency, $\hbar$ is the reduced Planck's constant, ω is the angular-frequency, $f_{BE}(\omega, T)$ is the Bose-Einstein distribution $\frac{\frac{\hbar\omega}{k_B} exp\left(\frac{\hbar\omega}{k_B T}\right)}{\left[exp\left(\frac{\hbar\omega}{k_B T}\right)-1\right]^2}$, T is the temperature, and $D(\omega)$ is the phonon density of states.

The volumetric specific heat *C* is calculated based on *U* as

$$C = \frac{\partial U}{\partial T} = \int_0^{\omega_0} \hbar\omega \frac{\partial f_{BE}}{\partial T} D(\omega) d\omega \tag{2}$$

where $\frac{\partial f_{BE}}{\partial T}$ is the partial differentiation of the Bose-Einstein distribution for the temperature *T*.

We approximate the phonon dispersion relation by a quadratic form $\omega(k) = v_s k + ck^2$ and solve the wave vector *k* such that

$$k = -\frac{v_s}{2c} - \sqrt{\frac{v_s^2}{c^2} + \frac{\omega}{c}} \tag{3}$$

where v_s is the phonon group velocity and *c* is a fitting parameter. Best fitting to the longitudinal acoustic and transverse acoustic modes of the phonon dispersion relation from neural scattering experiment yields $v_{s,\,LA} = 9000$ ms^{-1}, $v_{s,\,TA} = 5230$ ms^{-1}, $c_{LA} = -2\times10^{-7}$ and $c_{TA} = -2.26\times10^{-7}$.

The phonon density of states $D(\omega)$ can then be expressed as

$$D(\omega) = 3\frac{4\pi^2 k^2 dk/(2\pi/L)^3}{V d\omega} = \frac{3k^2 dk}{2\pi^2 d\omega}$$

$$= \frac{3}{2\pi^2}\left(\frac{v_s^2}{2c^2}+\frac{\omega}{c}+\frac{v_s}{c}\sqrt{\frac{v_s^2}{c^2}+\frac{\omega}{c}}\right)\left[-\frac{1}{2c}\left(\frac{v_s^2}{c^2}+\frac{\omega}{c}\right)^{-\frac{1}{2}}\right]$$

$$= \left(-\frac{3v_s^2}{8\pi^2c^3}-\frac{3\omega}{4\pi^2c^2}\right)\left(\frac{v_s^2}{c^2}+\frac{\omega}{c}\right)^{-\frac{1}{2}}+\frac{3v_s}{4\pi^2c^2} \tag{4}$$

The thermal conductivity based on the kinetic theory can be expressed as

$$\begin{aligned} k &= \frac{1}{3}\int_0^{\omega_0}\hbar\omega\frac{\partial f_{BE}}{\partial T}D(\omega)v_g(\omega)\Lambda_{eff}(\omega)d\omega \\ &= \frac{1}{3}\int_0^{\omega_{0,LA}}\hbar\omega\frac{\frac{\hbar\omega}{k_B}exp\left(\frac{\hbar\omega}{k_BT}\right)}{T^2\left[exp\left(\frac{\hbar\omega}{k_BT}\right)-1\right]^2}\frac{3}{2\pi^2}\left(\frac{v_s^2}{2c^2}+\frac{\omega}{c}\right. \\ &\quad \left.+\frac{v_s}{c}\sqrt{\frac{v_s^2}{c^2}+\frac{\omega}{c}}\right)\left[\Lambda_B^{-1}+\tau_{imp}^{-1}v_g^{-1}(\omega)+\tau_U^{-1}v_g^{-1}(\omega)\right]^{-1}d\,\omega \\ &\quad +\frac{2}{3}\int_0^{\omega_{0,TA}}\hbar\omega\frac{\frac{\hbar\omega}{k_B}exp\left(\frac{\hbar\omega}{k_BT}\right)}{T^2\left[exp\left(\frac{\hbar\omega}{k_BT}\right)-1\right]^2}\frac{3}{2\pi^2}\left(\frac{v_s^2}{2c^2}+\frac{\omega}{c}\right. \\ &\quad \left.+\frac{v_s}{c}\sqrt{\frac{v_s^2}{c^2}+\frac{\omega}{c}}\right)\left[\Lambda_B^{-1}+\tau_{imp}^{-1}v_g^{-1}(\omega)+\tau_U^{-1}v_g^{-1}(\omega)\right]^{-1}d\,\omega \end{aligned} \tag{5}$$

The phonon-boundary, -impurity, and Umklapp scattering are considered in the thermal conductivity calculation in this dissertation, while other phonon scattering mechanisms exist and examples are depicted in Fig. A1 for bulk Si. The intrinsic phonon mean free path in bulk Si due to phonon-impurity and Umklapp scattering is modified by the addition of nanoporous, as depicted in Fig. A1. The effective phonon mean free path accounts for the diffuse phonon scattering at pore boundaries and this effect is captured by the ray tracing simulation.

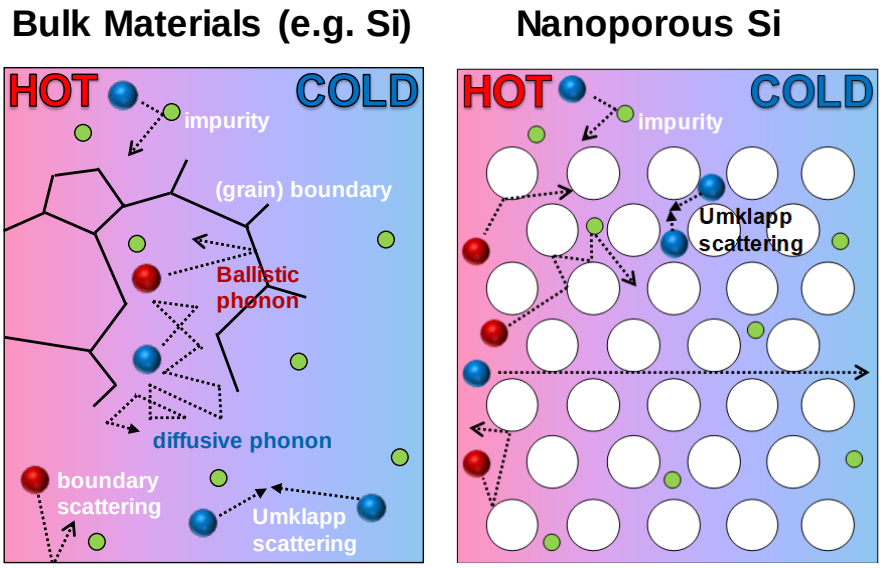

Figure A1. Phonon scattering mechanisms in bulk Si and nanoporous Si. The phonon transport can be either diffusive or ballistic, depending on the critical dimension of the material. Phonons can be scattered by various mechanisms including phonon-boundary, -impurity, -grain boundary, and Umklapp scattering.

2. Ray Tracing Simulations

In this dissertation, the ray tracing simulation is performed in two-dimensional (2D) because we focus on understanding the phonon-boundary scattering in lateral directions and the Si nanoporous structures considered have through-holes that are uniform along the *z*-direction. The pore shapes studied in this dissertation all possess symmetry at least along *x*- and/or *y*-axis. Therefore, a unit cell is first selected to reduce computational cost. Taking squared-lattice circular pores as an example, as shown in Fig. A2, the top and bottom boundaries of the unit cell are subject to specular boundary conditions. Phonons hitting these boundaries are going to be reflected specularly as if they pass the boundary into an adjacent unit cell along the mirror-like direction. Along the heat flow direction, the left and right boundaries are set to be periodic, allowing phonon exiting either boundary to re-emerge from the opposite boundary with identical *y*-coordinate and direction. Phonons scattered by the pore

boundary can move specularly or diffusely, depending on the surface specularity coefficient between 0 and 1. For diffuse phonon scattering at the pore boundary, a new direction is determined by randomly assigning an angle between 0 to 180° to the local normal direction, emulating the photon emission. The length of the simulation domain, *L*, along the *x*-direction is multiple of a single unit cell. Phonons are injected into the unit cell from either left or right boundary at an angle randomly picked from 0 to 180°, again emulating the photon emission. The phonon trajectory is traced and recorded during the simulation. For a single phonon, the simulation terminates when the phonon travels *L* or goes back to the initial boundary. In all ray tracing simulations in this dissertation, 5×10^6 phonons are considered. Among these phonons, those traveling *L* distance will be considered as transmitted phonons and an average transmission coefficient $\langle\tau\rangle$ is calculated by dividing the number of transmitted phonons by the total number of injected phonons. The phonon-boundary scattering mean free path in the ballistic regime is then computed based on $\langle\tau\rangle$ and combined with phonon mean free paths due to impurity and Umklapp scattering via Matthiessen's rule. Finally, the thermal conductivity is to be calculated using Eq. (4).

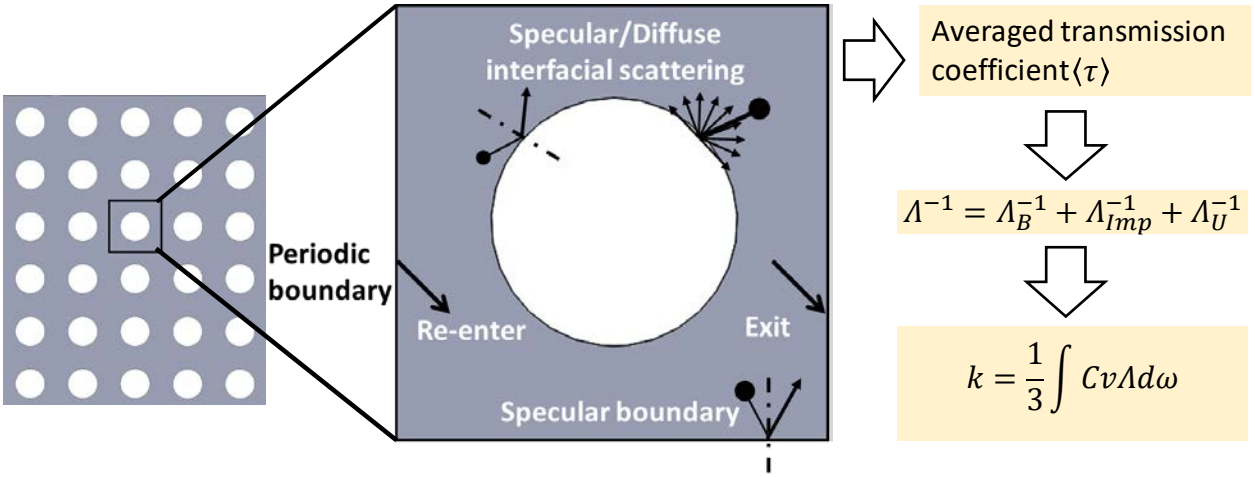

Figure A2. Flowchart of the ray tracing simulation.

The main purpose of the Monte Carlo Ray Tracing simulation is to numerically solve the Boltzmann Transport Equation for phonon transport in nanoporous structures with varying geometrical parameters. The ray tracing algorithm is developed for both 2D and three-dimensional (3D) scenarios. The ray tracing algorithm is validated in 3D against the experimental data of silicon nanomeshes. The 2D ray tracing algorithm is developed by modifying the equations used in the 3D scenario. Though no fundamental difference is expected for ray tracing simulations in 2D and 3D, the 2D ray tracing algorithm is validated against published modeling results for silicon nanoporous structures with varying pore shapes and pore configurations. As shown in Fig. A3, the effective thermal conductivity κ_{eff} computed for aligned squared (AS) pores, staggered squared (SS) pores, aligned triangular (AT) pores, and staggered triangular (ST) pores by the 2D ray tracing algorithm developed in this work and by solving the mean free path-dependent BTE (MFP-BTE) are in a good agreement (uncertainties range from 4% to 7%).

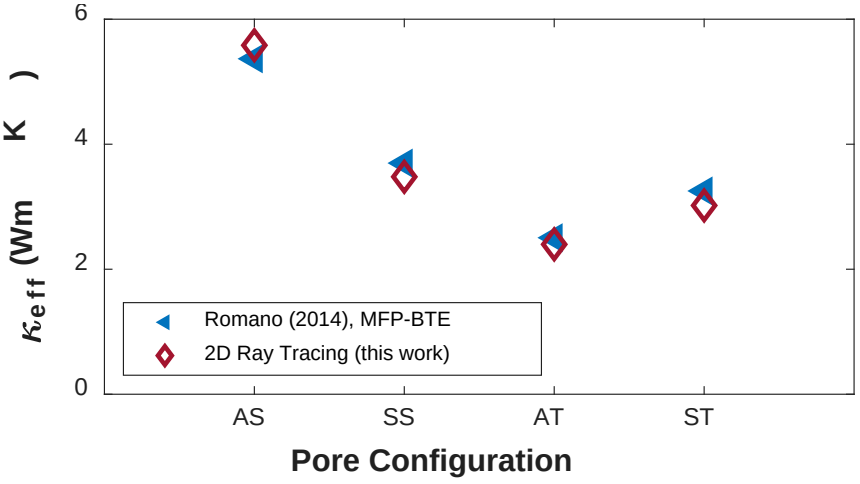

Figure A3. Effective thermal conductivity computed for aligned squared (AS), staggered squared (SS), aligned triangular (AT), and staggered triangular (ST) pores in 2D by using 2D ray tracing algorithm developed in this work and by solving the MFP-BTE in the published literature. The results obtained by the two methods agree well (uncertainties are between 4% to 7%).

An averaged transmission coefficient for phonons $\langle \mathcal{T} \rangle$ is calculated through Monte Carlo integration over the polar (θ) and azimuthal (ϕ) angles and the cross-sectional area (A) of a unit cell of the nanoporous structure, $\int_0^{2\pi} \int_0^{\pi/2} \tau(\theta, \phi, A) \cos\theta \sin\theta d\theta d\phi dA / \pi A$. These three variables account for phonons injected into the unit cell at random positions and along random directions in 3D space. To minimize the computational cost, a unit cell is chosen and the parallel computation is enabled using the parallel-for function family in MATLAB. Using the silicon nanomeshes that have been experimentally characterized as an example. The schematic of the unit cell in the MATLAB model is illustrated in Fig. A4.

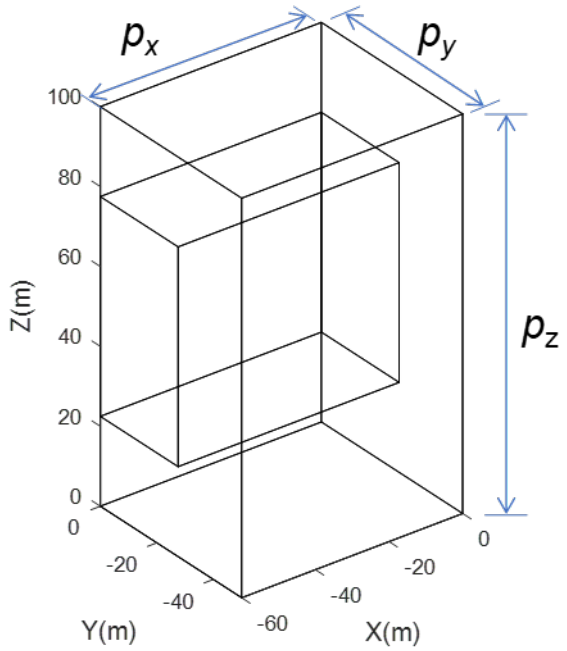

Figure A4. The schematic of the unit cell of Si nanomeshes generated in the MATLAB ray tracing model. The pitches along *x*, *y*, and *z* axes are p_x, p_y, and p_z. The dimension is in nanometers. The unit cell is half of a single nanomesh and the plane of symmetry is in *yz*. The rectangular object in the center represents the pore. The object outside the pore represents silicon.

Phonons are injected into the unit cell from the top surface by emulating the photon emission. The position is randomly selected within the top surface and we can define this initial position as

$[x_1, y_1, z_1]$. The initial direction is randomly chosen as well and is defined by θ and ϕ, respectively, as

$$\theta = \sin^{-1}\sqrt{R_1} \tag{6.a}$$

$$\phi = 2\pi R_2 \tag{6.b}$$

where R_1 and R_2 are two random numbers between 0 and 1. θ and ϕ range from 0 to π and 0 to $\frac{\pi}{2}$, respectively. The two angle forms a hemisphere with its center aligned with the surface normal ([0,0,-1]) of the top surface. The next position of the phonon is determined by finding the next closed surface along its direction. The distance from the initial position to each surface in the unit cell is calculated and the one with the minimum is chosen as the surface the phonon will collide on. In general, this procedure is implemented when searching for the next surface for a phonon to collide with. Denoting the current direction of the phonon as $\vec{d}_c = [d_{c,x},\ d_{c,y},\ d_{c,z}]$ and the surface normal of surface i in the unit cell as $\vec{n}_i = [n_{i,x}, n_{i,y}, n_{i,z}]$, the direction along which the phonon lands on the surface i can be found by

$$\psi_i = \cos^{-1}(\vec{d}_c \cdot \vec{n}_i) \tag{7}$$

If ψ is 90° or 270°, the phonon is moving parallel with the surface, so no collision will happen. Using the origin [0, 0, 0] as a global reference, the shortest distance between the surface i labeled by the surface normal $\vec{n}_i = [n_{i,x}, n_{i,y}, n_{i,z}]$ can be computed by a dot product

$$\vec{D}_i = n_{i,x}x_i + n_{i,y}y_i + n_{z,i}z_i \tag{8}$$

where $[x_i, y_i, z_i]$ is one of the vortex points of the surface i. ψ_i and $\vec{D}_i$ are computed for all the surfaces $j = 1 \ldots N$ in the unit cell except for the surface i that the phonon is currently on ($i \neq j$). Usually, if the surface is flat, a phonon cannot collide with the same surface successively.

However, if the surface is concave, for example, if a spherical surface is considered, the algorithm will be modified correspondingly to consider the same surface as the next possible surface to collide with. Among all the surfaces in the unit cell besides the current surface the phonon locates, the surfaces $i's$ with ψ_i = 90° or 270° will not be considered. For other surfaces that are qualified, the distance between the phonon's current position and the surface will be calculated as

$$L_i = -\frac{\vec{n}_i \cdot p_c + \vec{D}_i}{\cos\psi_i} \tag{9}$$

where $p_c = [p_{c,x},\ p_{c,y},\ p_{c,z}]$ is the current position for the phonon. Note that if L_i is negative, it indicates that the phonon's next direction made an acute angle with the surface normal $\vec{n}_i$, which means the phonon is leaving that surface. The surfaces $i's$ with positive L_i will be tested afterward to see if their current direction will transverse the area of the surface i. For each surface i, the position that the phonon will land is determined by

$$p_{L,i} = p_c + \vec{d}_c \cdot L_i \tag{10}$$

Using the right-hand rule, by successively taking the cross product of the vector made by $p_{L,i}$ and each vortex points of the surface i denoted by $v_{ik} = [v_{ik,x}, v_{ik,y}, v_{ik,z}]$ (k is the index of vortex points) in a counter-clockwise direction, if $p_{L,i}$ stays within the surface i can be determined.

A specularity coefficient ϱ ($0 \leq \varrho \leq 1$) is used to determine whether the collision is specular or not. In the ray tracing simulation, this coefficient is global. Specifically for each collision, a random number R_3 ($0 \leq R_3 \leq 1$) is generated to compare with ϱ. As ϱ indicates the possibility a phonon will be scattered specularly, $R_3 \leq \varrho$ means the phonon will experience specular scattered for sure, and the phonon will be diffusely scattered otherwise.

If a specular scattering happens, the new phonon direction is computed by the law of reflection, where the angle of incident is equal to the angle of reflection, as

$$\vec{d}_n = 2\vec{n}_i \cdot \left[\vec{n}_i \cdot \left(-\vec{d}_c\right)\right] + \vec{d}_c \tag{11}$$

If a diffuse scattering happens, the new phonon direction is computed in analog to the photon emission using two random numbers, similar to how phonons are injected into the unit cell discussed previously. The corresponding polar and azimuthal angles associated with the new direction are

$$\theta_{local} = \sin^{-1}\sqrt{R_3} \tag{12.a}$$

$$\phi_{local} = 2\pi R_4 \tag{12.b}$$

where R_3 and R_4 range from 0 to 1. Note that θ_{local} and ϕ_{local} are with respect to the local surface normal of the current surface phonon resides. The correspondingly local new direction for the phonon is computed as

$$\vec{d}_{n,local} = [\sin\theta_{local}\cos\phi_{local}, \sin\theta_{local}\sin\phi_{local}, -\cos\theta_{local}] \tag{13}$$

To translate into the global coordinate cartesian system, a rotation matrix defined by two rotation angles, namely rotation polar angle θ_{rot} and rotation azimuthal angle ϕ_{rot}, is required. Such a matrix can be expressed as

$$\boldsymbol{R} = \begin{bmatrix} \cos\theta_{rot}\cos\phi_{rot} & -\sin\phi_{rot} & \sin\theta_{rot}\cos\phi_{rot} \\ \cos\theta_{rot}\sin\phi_{rot} & \cos\phi_{rot} & \sin\theta_{rot}\sin\phi_{rot} \\ -\sin\theta_{rot} & 0 & \cos\theta_{rot} \end{bmatrix} \tag{14}$$

Then the global new direction for the phonon is computed by the matrix multiplication as

$$\vec{d}_n = \boldsymbol{R}\vec{d}_{n,local} \tag{15}$$

2D ray tracing algorithm is developed by modifying some of the equations used for the 3D scenario. Specifically, the direction of heat flow is set to be along the *x*-axis. In this case, the surface normal for the initial surface is pointed towards 0° (positive *x*) if the phonon is injected from the left boundary. As we do not need to introduce an azimuthal angle to describe the 2D coordinate system, only the polar angle θ is considered. The phonon is injected similar to that for the 3D case by emulating the photon emission, which is

$$\theta = \sin^{-1}(1 - 2R_1) + \frac{\pi}{2} \tag{16}$$

where R_1 is randomly generated from 0 to 1. The same equation is used to determine the new direction of a phonon being scattered diffusely by a pore boundary. The direction vector with respect locally to the pore boundary is calculated by

$$\vec{d}_{n,local} = \begin{bmatrix} \sin\theta_{local} \\ \cos\theta_{local} \end{bmatrix} \tag{17}$$

Again, to convert $\vec{d}_{n,local}$ to the global coordinate system, a 2D rotation matrix constructed based on a rotation polar angle θ_{rot} is employed. The matrix reads

$$\boldsymbol{R}_{\mathbf{2\times2}} = \begin{bmatrix} \cos\theta_{rot} & -\sin\theta_{rot} \\ \sin\theta_{rot} & \cos\theta_{rot} \end{bmatrix} \tag{18}$$

The global new direction for a phonon is then calculated as

$$\vec{d}_n = \boldsymbol{R}_{\mathbf{2\times2}}\vec{d}_{n,local} \tag{19}$$

3. Simulating Elastic Topological Insulators in COMSOL Multiphysics

The band structure for the six-petal holey structure is obtained by solving the eigenvalue problem Eq. (20) in COMSOL Multiphysics finite element solver.

$$\nabla \cdot \left[C : [\nabla\psi + (\nabla\psi)^T]\right] = -2\varrho\omega^2\psi \tag{20}$$

where ψ is the complex 3D wave function, C is the elasticity tensor, and ϱ is the mass density. The mechanical displacement field $\boldsymbol{u}$ is related to the wave function ψ by $\boldsymbol{u} = \mathrm{Re}\left[\psi \cdot e^{i\omega t}\right]$.

Specifically, the band structure in COMSOL Multiphysics is calculated by sweeping along the path enclosing the first Brillouin zone in the reciprocal space. The lattice structure in real space and reciprocal space are detailed in Fig. A5.

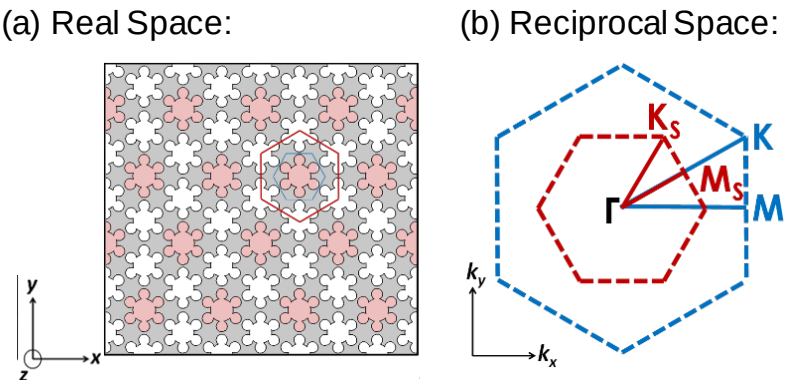

Figure A5. Hexagonal-lattice six-petal holey Si structure in (a) real space and (b) reciprocal space. **Γ**, **M**, and **K** are high-symmetry points before breaking the discrete translational symmetry, whereas Γ_S, M_S, and K_S are those when the symmetry is broken, leading to the zone-folding effect.

In real space, for a hexagonal lattice, two lattice vectors can be defined as $\overrightarrow{a_1} = \left(\frac{\sqrt{3}a}{a}, \frac{a}{2}\right)$ and $\overrightarrow{a_2} = \left(\frac{\sqrt{3}a}{a}, \frac{a}{2}\right)$. The corresponding lattice vectors $\overrightarrow{b_1}$ and $\overrightarrow{b_2}$ in reciprocal space can be computed based on the relation

$$\begin{bmatrix} b_{1x} & b_{2x} \\ b_{1y} & b_{2y} \end{bmatrix} = \frac{2\pi}{a_{1x}a_{2y} - a_{2x}a_{1y}} \begin{bmatrix} a_{2y} & -a_{1y} \\ -a_{2x} & a_{1x} \end{bmatrix} \quad (21)$$

$\overrightarrow{b_1}$ and $\overrightarrow{b_2}$ are therefore $\left(\frac{2\pi}{\sqrt{3}a}, \frac{2\pi}{a}\right)$ and $\left(\frac{2\pi}{\sqrt{3}a}, -\frac{2\pi}{a}\right)$, pointing towards 60° and -60° with respect to k_x in (b), respectively, with a norm of $\left\|\overrightarrow{b_1}\right\| = \left\|\overrightarrow{b_2}\right\| = \frac{4\pi}{\sqrt{3}a}$.

Note that in the reciprocal space, the distance between high-symmetry points Γ and M, $\overline{\Gamma M}$, is half of $\left\|\overrightarrow{b_1}\right\|$ (or $\left\|\overrightarrow{b_2}\right\|$), which is $\frac{2\pi}{\sqrt{3}a}$. The coordinates for M and K are thus $\left(\frac{2\pi}{\sqrt{3}a}, 0\right)$ and $\left(\frac{2\pi}{\sqrt{3}a}, \frac{2\pi}{3a}\right)$.

Sweeping wave vector $\vec{k}$ along the path **Γ**-**M**-**K**-**Γ** produces the band structure with a single Dirac cone, as shown in Fig. 4.1 in the main text.

The same procedure can be repeated for the folded first Brillouin zone to produce the band structure with a double Dirac cone. As the lattice constant in real space is enlarged by a factor of $\sqrt{3}a$ by breaking the discrete translational symmetry, the corresponding first Brillouin zone shrinks by a factor $\sqrt{3}a$ in reciprocal space, as shown in Fig. A5(b).

4. Effective Optical Properties of Microsphere Composites

The scattering matrix elements S_1 and S_2 are written as

$$S_1 = \sum_n \frac{2n+1}{n(n+1)}(a_n\pi_n + b_n\tau_n) \tag{22.a}$$

$$S_2 = \sum_n \frac{2n+1}{n(n+1)}(a_n\tau_n + b_n\pi_n) \tag{22.b}$$

The scattering amplitudes of the forward and backward scatterings ignoring the electromagnetic wave polarizations are written as

$$S(\theta = 0°) = \frac{1}{2}[S_1(\theta = 0°) + S_2(\theta = 0°)] \tag{23.a}$$

$$S(\theta = 180°) = \frac{1}{2}[S_1(\theta = 180°) + S_2(\theta = 180°)] \tag{23.b}$$

In Eq. (22.a) and Eq. (22.b), two angular-dependent functions $\pi_n(\theta)$ and $\tau_n(\theta)$ are defined as

$$\pi_n(\theta) = \frac{P_n^1}{\sin\theta} \tag{24.a}$$

$$\tau_n(\theta) = \frac{dP_n^1}{d\theta} \tag{24.b}$$

where P_n^1 refers to the associated Legendre polynomials of degree *n* and order 1, and θ is the scattering angle made by the incident and scattered waves. The associated Legendre polynomial of degree *m* and order *n* has the following property

$$P_n^m = (1-\mu^2)^{m/2}\frac{d^m P_n(\mu)}{d\mu^m} \tag{25}$$

Knowing that $\mu = \cos\theta$ and substituting Eq. (25) into Eq. (24), yields

$$\pi_n(\theta) = \frac{\sqrt{1-\cos^2\theta}}{\sin\theta}\frac{dP_n(\cos\theta)}{d\cos\theta} = \frac{dP_n(\cos\theta)}{d\cos\theta} \tag{26.a}$$

$$\tau_n(\theta) = \frac{d}{d\theta}\left[\sin\theta\frac{dP_n(\cos\theta)}{d\cos\theta}\right] \tag{26.b}$$

Rewriting Eq. (26.a) and Eq. (26.b) in terms of μ gives

$$\pi_n(\mu) = \sqrt{1-\mu^2}\frac{dP_n(\mu)}{d\mu} \tag{27.a}$$

$$\begin{aligned}\tau_n(\mu) &= -\sin\theta\frac{d}{d\mu}\left[\sqrt{1-\mu^2}\frac{dP_n(\mu)}{d\mu}\right] \\ &= -\frac{1}{2}\sqrt{1-\mu^2}(-2\mu)\left[\frac{\frac{dP_n(\mu)}{d\mu}}{\sqrt{1-\mu^2}} + \sqrt{1-\mu^2}\frac{d^2P_n(\mu)}{d\mu^2}\right] \\ &= \frac{\mu dP_n(\mu)}{d\mu} - (1-\mu^2)\frac{d^2P_n(\mu)}{d\mu^2}\end{aligned} \tag{27.b}$$

For forward scattering, substituting $\mu = 1$ into Eq. (27), gives

$$\pi_n(1) = \left.\frac{dP_n(\mu)}{d\mu}\right|_{\mu=1} \tag{28.a}$$

$$\tau_n(1) = \left.\frac{dP_n(\mu)}{d\mu}\right|_{\mu=1} \tag{28.b}$$

such that

$$\pi_n(1) = \tau_n(1) \tag{29}$$

Realizing that P_n also satisfies the following partial differential equation

$$\frac{1}{\sin\theta}\frac{d}{d\theta}\left(\sin\theta\frac{d\Theta}{d\theta}\right) + \left[n(n+1) - \frac{m^2}{\sin^2\theta}\right]\Theta = 0 \tag{30}$$

Eq. (30) is derived for a spherical object subject to incident electromagnetic waves, as illustrated in Fig. A6

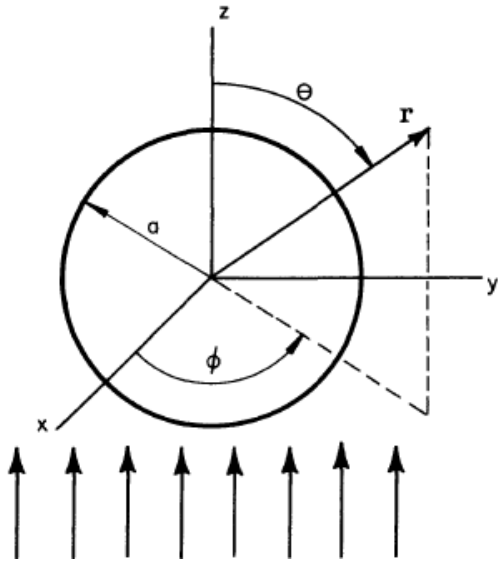

Figure A6. Electromagnetic wave incidents on a sphere in spherical coordinate.

The governing equation for the electric and magnetic fields are

$$\nabla^2\mathbf{E} + k^2\mathbf{E} = 0 \tag{31.a}$$

$$\nabla^2\mathbf{H} + k^2\mathbf{H} = 0 \tag{31.b}$$

Expressing Eq. (27) in spherical coordinate

$$\frac{1}{r^2}\frac{\partial}{\partial r}\left(r^2\frac{\partial\psi}{\partial r}\right) + \frac{1}{r^2\sin\theta}\frac{\partial}{\partial\theta}\left(\sin\theta\frac{\partial\psi}{\partial\theta}\right) + \frac{1}{r^2\sin\theta}\frac{\partial^2\psi}{\partial\phi^2} + k^2\psi = 0 \tag{32}$$

Applying separation of variable yields

$$\psi(r,\theta,\phi) = R(r)\Theta(\theta)\Phi(\phi) \tag{33}$$

and Eq. (33) produces three sets of ordinary differential equations

$$\frac{d^2\Phi}{d\phi^2} + m^2\Phi = 0 \tag{34.a}$$

$$\frac{1}{\sin\theta}\frac{d}{d\theta}\left(\sin\theta\frac{d\Theta}{d\theta}\right)+\left[n(n+1)-\frac{m^2}{\sin^2\theta}\right]\Theta=0 \tag{34.b}$$

$$\frac{d}{dr}\left(r^2\frac{dR}{dr}\right)+[k^2r^2-n(n+1)]R=0 \tag{34.c}$$

Substituting in $\Theta=P_n(\mu)$ and noting $m=0$, the above partial differential equation becomes

$$\frac{1}{\sqrt{1-\mu^2}}\left(-\sqrt{1-\mu^2}\right)\frac{d}{d\mu}\left[\sqrt{1-\mu^2}\left(-\sqrt{1-\mu^2}\right)\frac{dP_n(\mu)}{d\mu}\right]+n(n+1)P_n(\mu)=0 \tag{35}$$

Eq. (35) can be simplified to

$$\begin{aligned}&\frac{d}{d\mu}\left[(1-\mu^2)\frac{dP_n(\mu)}{d\mu}\right]+n(n+1)P_n(\mu)\\&\qquad=-2\mu\frac{dP_n(\mu)}{d\mu}+(1-\mu^2)\frac{d^2P_n(\mu)}{d\mu^2}+n(n+1)P_n(\mu)=0\end{aligned} \tag{36}$$

When $\mu=1$, Eq. (36) reduces to

$$-2\left.\frac{dP_n(\mu)}{d\mu}\right|_{\mu=1}+n(n+1)P_n(1)=0 \tag{37}$$

and further to

$$-2\pi_n(1)+n(n+1)P_n(1)=0 \tag{38}$$

Noting that $P_n(1)=1$, rearranging gives

$$\pi_n(1)=\frac{n(n+1)}{2} \tag{39}$$

Similarly, for scattering in the backward direction, or backscattering

$$\pi_n(-1)=-\tau_n(-1)=(-1)^n\frac{n(n+1)}{2} \tag{40}$$

For a composite made of *N* particles in a unit cell with permittivity $\varepsilon_s = n_s^2$ embedded in a host with permittivity $\varepsilon_h = n_h^2$, then the effective parameters are

$$\frac{\mu_{eff} - \mu_0}{\mu_{eff} + 2\mu_0} = \frac{2\pi i N}{k_h^3} \langle \overline{b_1^{Mie}} \rangle \tag{41.a}$$

$$\frac{\varepsilon_{eff} - \varepsilon_0}{\varepsilon_{eff} + 2\varepsilon_0} = \frac{2\pi i N}{k_h^3} \langle \overline{a_1^{Mie}} \rangle \tag{41.b}$$

The volume fraction *f* correlates with *N* by

$$N = \frac{3f}{4\pi r^3} \tag{42}$$

where *a* is the microsphere radius.

Substituting into Eq. (41) yields

$$\frac{\mu_{eff} - \mu_0}{\mu_{eff} + 2\mu_0} = i \frac{3f}{2(k_h r)^3} \langle \overline{b_1^{Mie}} \rangle \tag{43.a}$$

$$\frac{\varepsilon_{eff} - \varepsilon_0}{\varepsilon_{eff} + 2\varepsilon_0} = i \frac{3f}{2(k_h r)^3} \langle \overline{a_1^{Mie}} \rangle \tag{43.b}$$

Denoting $\gamma = \frac{3f}{2(k_h r)^3}$, Eq. (43) finally reduces to

$$\frac{\mu_{eff} - \mu_0}{\mu_{eff} + 2\mu_0} = i\gamma \langle \overline{b_1^{Mie}} \rangle \tag{44.a}$$

$$\frac{\varepsilon_{eff} - \varepsilon_0}{\varepsilon_{eff} + 2\varepsilon_0} = i\gamma \langle \overline{a_1^{Mie}} \rangle \tag{44.b}$$

The effective properties μ_{eff} and ε_{eff} can be expressed as

$$\mu_{eff} = 1 + i \frac{3f}{2x^3} (S_{\theta=0} + S_{\theta=\pi}) \tag{45.a}$$

$$\varepsilon_{eff} = \varepsilon_P \left[1 + i \frac{3f}{2x^3} (S_{\theta=0^\circ} + S_{\theta=\pi}) \right] \tag{45.b}$$

where x is the size parameter $x = \frac{2\pi r}{\lambda}$ and λ is the wavelength.

Following the Mie theory derivation above and the effective optical properties expression, the extinction, scattering, absorption coefficients, real and imaginary parts of the dielectric constants n and k, and the absorption lengths in Ref. [76] were reproduced. As shown in Fig. A7, A8, and A9, good agreements can be seen, which validated the Mie theory calculation.

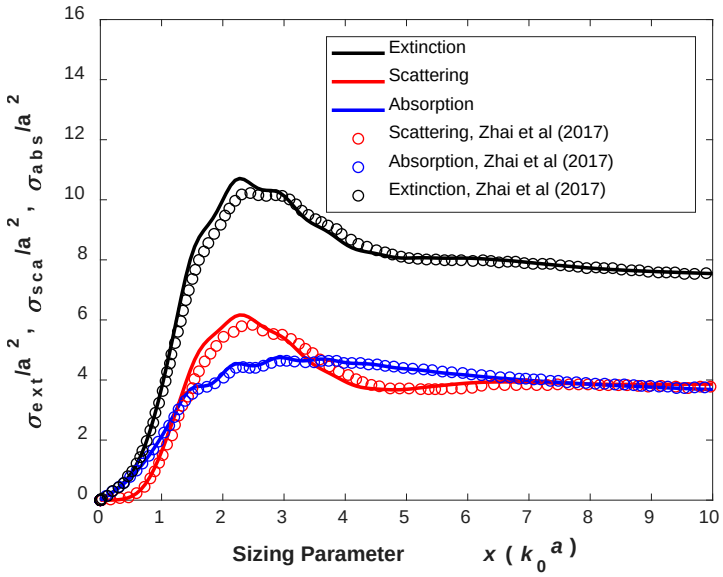

Figure A7. The extinction, scattering, and absorption coefficients computed via Mie theory. The hollow markers are the results reported in Ref. [76] and the solid lines are the results calculated using the algorithms developed in the current doctoral research work.

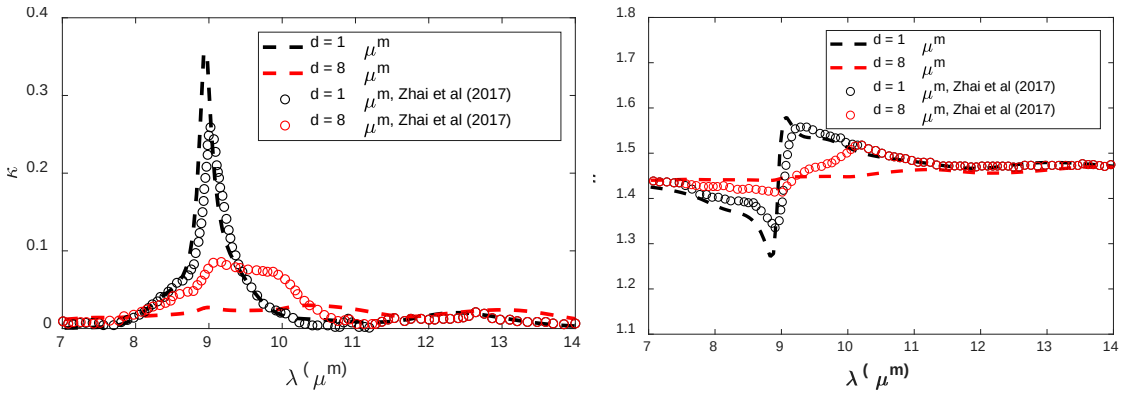

Figure A8. The imaginary and real parts of the dielectric constants k and n for SiO_2 microspheres with diameters 1 and 8 μm in the TPX polymer matrix at a volume fraction of 6 vol%. The values

for d = 1 μm from Ref. [76] and our calculation agrees well, whereas some discrepancy appears for the values for d = 8 μm. The discrepancy may be due to the difference in the source of optical properties used in Ref. [76] and our calculation. Despite the difference in values, the overall trend is well captured.

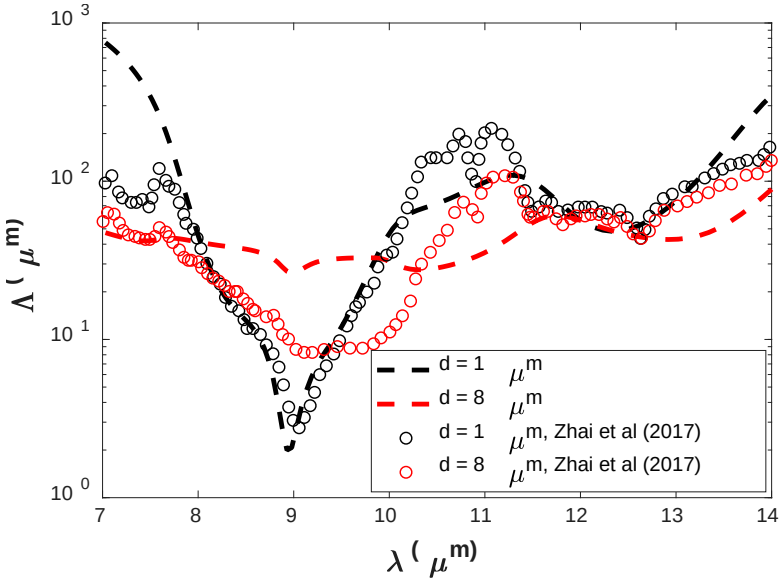

Figure A9. The absorption length Λ for solid SiO_2 microspheres with diameters of 1 and 8 μm in the TPX matrix at a volume fraction of 6 vol%. Fair agreements are obtained for Λ for d = 1 μm, whereas for d = 8 μm, some discrepancy is observed. The discrepancy may be due to the difference in optical properties used in Ref. [76] and our calculation.

Differing from the Mie theory for the solid microsphere, the Mie scattering coefficients for the coated microsphere are expressed as the following

$$a_n = \frac{\left(\widetilde{D}_n/m_2 + n/y\right)\psi_n(y) - \psi_{n-1}(y)}{\left(\widetilde{D}_n/m_2 + n/y\right)\xi_n(y) - \xi_{n-1}(y)} \tag{46.a}$$

$$b_n = \frac{\left(m_2\tilde{G}_n + n/y\right)\psi_n(y) - \psi_{n-1}(y)}{\left(m_2\tilde{G}_n + n/y\right)\xi_n(y) - \xi_{n-1}(y)} \tag{46.b}$$

where two size parameters are considered for the core and shell as $x = \frac{2m_1\pi r_1}{\lambda}$ and $y = \frac{2m_2\pi r_2}{\lambda}$, and effective refractive index $m = m_2/m_1$. The subscripts "1" and "2" correspond to the media of the core and shell. $\widetilde{D}_n$ and $\tilde{G}_n$ are introduced to avoid the singularity at $r_1 = 0$ and they can be expressed as

$$\widetilde{D}_n = \frac{D_n(m_2x) - A_n\chi_n'(m_2y)/\psi_n(m_2y)}{1 - A_n\chi_n(m_2y)/\psi_n(m_2y)} \tag{47.a}$$

$$\widetilde{G}_n = \frac{D_n(m_2x) - B_n\chi_n'(m_2y)/\psi_n(m_2y)}{1 - B_n\chi_n(m_2y)/\psi_n(m_2y)} \tag{47.b}$$

where A_n and B_n are respectively

$$A_n = \psi_n(m_2x)\frac{mD_n(m_1x) - D_n(m_2x)}{mD_n(m_1x)\chi_n(m_2x) - \chi_n'(m_2x)} \tag{48.a}$$

$$B_n = \psi_n(m_2x)\frac{D_n(m_1x)/m - D_n(m_2x)}{D_n(m_1x)\chi_n(m_2x)/m - \chi_n'(m_2x)} \tag{48.b}$$

As a validation, the extinction, scattering, and absorption coefficients of a single SiO_2 microsphere calculated by using the Mie theory for solid microspheres and Mie theory for hollow microspheres but with $r_1 = 0$ are compared. And as expected, they lead to the same results, as shown in Fig. A10.

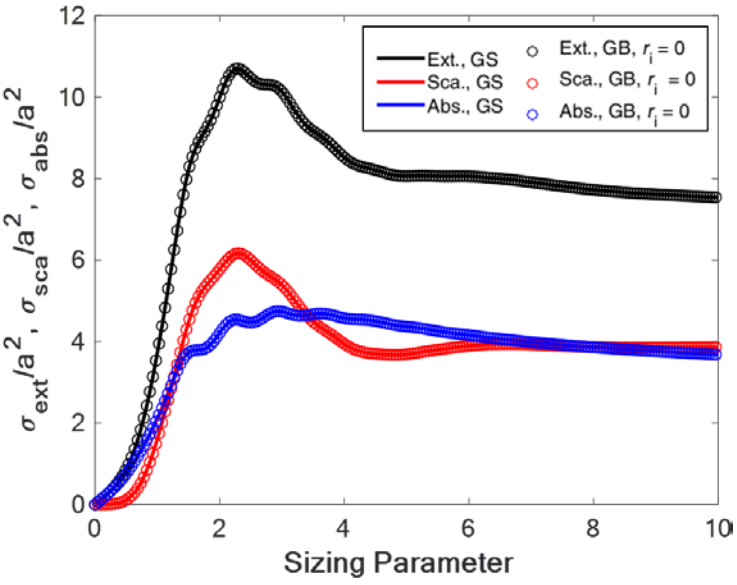

Figure A10. Comparison of the extinction, scattering, and absorption coefficient of a solid SiO_2 microsphere using Mie theory developed for solid microspheres and Mie theory developed for hollow microspheres with $r_1 = 0$.

Bibliography

[1] Shi L, Dames C, Lukes JR, Reddy P, Duda J, Cahill DG, et al. Evaluating broader impacts of nanoscale thermal transport research. Nanoscale Microscale Thermophys Eng. 2015;19(2):127.

[2] Wang Y, Chen KS, Cho SC. PEM Fuel Cells: Thermal and Water Management Fundamentals. Momentum Press. 2013.

[3] Glassbrenner CJ, Slack GA. Thermal conductivity of silicon and germanium from 3°K to the melting point. Phys Rev. 1964;134(4A).

[4] Asheghi M, Kurabayashi K, Kasnavi R, Goodson KE. Thermal conduction in doped single-crystal silicon films. J Appl Phys. 2002;91(8):5079.

[5] Asheghi M, Touzelbaev MN, Goodson KE, Leung YK, Wong SS. Temperature-dependent thermal conductivity of single-crystal silicon layers in soi substrates. J Heat Transfer. 1998;120(1):30.

[6] Asheghi M, Leung YK, Wong SS, Goodson KE. Phonon-boundary scattering in thin silicon layers. Appl Phys Lett. 1997;71(13):1798.

[7] Lee J, Lee W, Wehmeyer G, Dhuey S, Olynick DL, Cabrini S, et al. Investigation of phonon coherence and backscattering using silicon nanomeshes. Nat Commun [Internet]. 2017;8:14054. Available from: http://dx.doi.org/10.1038/ncomms14054

[8] Nomura M, Kage Y, Nakagawa J, Hori T, Maire J, Shiomi J, et al. Impeded thermal transport in Si multiscale hierarchical architectures with phononic crystal nanostructures. Phys Rev B - Condens Matter Mater Phys. 2015;91(20):205422.

[9] Kim B, Janet N, Clews PJ, Reinke CM, Goettler D, Leseman ZC, et al. Thermal Conductivity Manipulation in Single Crystal Silicon Via Lithographycally Defined Phononic Crystals. 2012 IEEE 25th Int Conf Micro Electro Mech Syst [Internet]. 2012;(12617970):176. Available from: https://ieeexplore.ieee.org/abstract/document/6170122

[10] Hopkins PE, Reinke CM, Su MF, Olsson RH, Shaner EA, Leseman ZC, et al. Reduction in the thermal conductivity of single crystalline silicon by phononic crystal patterning. Nano Lett. 2011;11(1):107.

[11] Lim J, Wang HT, Tang J, Andrews SC, So H, Lee J, et al. Simultaneous thermoelectric property measurement and incoherent phonon transport in holey silicon. ACS Nano. 2016;10(1):124.

[12] Lee J, Lim J, Yang P. Ballistic phonon transport in holey silicon. Nano Lett. 2015;15(5):3273.

[13] Tang J, Wang HT, Lee DH, Fardy M, Huo Z, Russell TP, et al. Holey Silicon as an Efficient Thermoelectric Material. Nano Lett [Internet]. 2010 Oct 13;10(10):4279. Available from: http://pubs.acs.org/doi/abs/10.1021/nl102931z

[14] Song D, Chen G. Thermal conductivity of periodic microporous silicon films. Appl Phys Lett. 2004;84(5):687.

[15] Ravichandran J, Yadav AK, Cheaito R, Rossen PB, Soukiassian A, Suresha SJ, et al. Crossover from incoherent to coherent phonon scattering in epitaxial oxide superlattices. Nat Mater. 2014;13(2):168.

[16] Garg J, Chen G. Minimum thermal conductivity in superlattices: A first-principles formalism. Phys Rev B - Condens Matter Mater Phys. 2013;87(14):140302.

[17] Jain A, Yu YJ, Mcgaughey AJHH. Phonon transport in periodic silicon nanoporous films with feature sizes greater than 100 nm. Phys Rev B. 2013;87(19):195301.

[18] Esfarjani K, Chen G, Stokes HT. Heat transport in silicon from first-principles calculations. Phys Rev B - Condens Matter Mater Phys. 2011;84(8):085204.

[19] Anufriev R, Yanagisawa R, Nomura M. Aluminium nanopillars reduce thermal conductivity of silicon nanobeams. Nanoscale. 2017;9(39):15083.

[20] He Y, Donadio D, Lee JH, Grossman JC, Galli G. Thermal transport in nanoporous silicon: Interplay between disorder at mesoscopic and atomic scales. ACS Nano. 2011;5(3):1839.

[21] Yang B, Chen G. Partially coherent phonon heat conduction in superlattices. Phys Rev B - Condens Matter Mater Phys. 2003;67(19):195311.

[22] Hopkins PE, Phinney LM, Rakich PT, Olsson RH, El-Kady I. Phonon considerations in the reduction of thermal conductivity in phononic crystals. Appl Phys A Mater Sci Process. 2011;103(3):575.

[23] Nomura M, Nakagawa J, Sawano K, Maire J, Volz S. Thermal conduction in Si and SiGe phononic crystals explained by phonon mean free path spectrum. Appl Phys Lett. 2016;109(17):173104.

[24] Dechaumphai E, Chen R. Thermal transport in phononic crystals: The role of zone folding effect. In: Journal of Applied Physics. 2012. p. 073508.

[25] Alaie S, Goettler DF, Su M, Leseman ZC, Reinke CM, El-Kady I. Thermal transport in phononic crystals and the observation of coherent phonon scattering at room temperature. Nat Commun [Internet]. 2015;6:7228. Available from: http://www.ncbi.nlm.nih.gov/pubmed/26105560

[26] Cahill DG, Braun P V., Chen G, Clarke DR, Fan S, Goodson KE, et al. Nanoscale thermal transport. II. 2003-2012. Appl Phys Rev. 2014;1:011305.

[27] Yu JK, Mitrovic S, Tham D, Varghese J, Heath JR. Reduction of thermal conductivity in phononic nanomesh structures. Nat Nanotechnol. 2010;5(10):718.

[28] Maire J, Anufriev R, Yanagisawa R, Ramiere A, Volz S, Nomura M. Heat conduction tuning by wave nature of phonons. Sci Adv. 2017;3(8):e1700027.

[29] Marconnet AM, Kodama T, Asheghi M, Goodson KE. Phonon conduction in periodically porous silicon nanobridges. Nanoscale Microscale Thermophys Eng. 2012;16(4):199.

[30] Yu Z, Ferrer-Argemi L, Lee J. Investigation of thermal conduction in symmetric and asymmetric nanoporous structures. J Appl Phys. 2017;122(24):244305.

[31] Hasan MZ, Kane CL. Colloquium: Topological insulators. Rev Mod Phys. 2010;82(4):3045.

[32] Qi XL, Zhang SC. Topological insulators and superconductors. Rev Mod Phys. 2011;83(4):1057.

[33] Thouless DJ, Kohmoto M, Nightingale MP, Den Nijs M. Quantized hall conductance in a two-Dimensional periodic potential. Phys Rev Lett. 1982;49(6):405.

[34] Hatsugai Y. Chern number and edge states in the integer quantum Hall effect. Phys Rev Lett. 1993;71(22):3697.

[35] Kane CL, Mele EJ. Z2 topological order and the quantum spin hall effect. Phys Rev Lett. 2005;95(14):146802.

[36] Zhang Y, Tan YW, Stormer HL, Kim P. Experimental observation of the quantum Hall effect and Berry's phase in graphene. Nature. 2005;438(7065):201.

[37] Novoselov KS, Jiang Z, Zhang Y, Morozov S V., Stormer HL, Zeitler U, et al. Room-temperature quantum hall effect in graphene. Science. 2007;315(5817):1379.

[38] Haldane FDM, Raghu S. Possible realization of directional optical waveguides in photonic crystals with broken time-reversal symmetry. Phys Rev Lett. 2008;100(1):013904.

[39] Wang Z, Chong Y, Joannopoulos JD, Soljačić M. Observation of unidirectional backscattering-immune topological electromagnetic states. Nature. 2009;461(7265):772.

[40] Lu L, Joannopoulos JD, Soljačić M. Topological photonics. Vol. 8, Nature Photonics. 2014. p. 821.

[41] Ma G, Xiao M, Chan CT. Topological phases in acoustic and mechanical systems. Nat Rev Phys. 2019;1(4):281.

[42] Roux P, De Rosny J, Tanter M, Fink M. The aharonov-bohm effect revisited by an acoustic time-reversal mirror. Phys Rev Lett. 1997;79(17):3170.

[43] Fleury R, Sounas DL, Sieck CF, Haberman MR, Alù A. Sound isolation and giant linear nonreciprocity in a compact acoustic circulator. Science. 2014;343(6170):516.

[44] Yang Z, Gao F, Shi X, Lin X, Gao Z, Chong Y, et al. Topological Acoustics. Phys Rev Lett. 2015;114(11):114301.

[45] Ni X, He C, Sun XC, Liu XP, Lu MH, Feng L, et al. Topologically protected one-way edge mode in networks of acoustic resonators with circulating air flow. New J Phys. 2015;17(5):053016.

[46] Khanikaev AB, Fleury R, Mousavi SH, Alù A. Topologically robust sound propagation in an angular-momentum-biased graphene-like resonator lattice. Nat Commun. 2015;6.

[47] Souslov A, Van Zuiden BC, Bartolo D, Vitelli V. Topological sound in active-liquid metamaterials. Nat Phys. 2017;13(11):1091.

[48] Nash LM, Kleckner D, Read A, Vitelli V, Turner AM, Irvine WTMM. Topological mechanics of gyroscopic metamaterials. Proc Natl Acad Sci U S A [Internet]. 2015;112(47):14495. Available from: http://arxiv.org/abs/1504.03362%0Ahttp://dx.doi.org/10.1073/pnas.1507413112

[49] Wang YT, Luan PG, Zhang S. Coriolis force induced topological order for classical mechanical vibrations. New J Phys. 2015;17(7):073031.

[50] Kane CL, Mele EJ. Quantum Spin hall effect in graphene. Phys Rev Lett. 2005;95(22):226801.

[51] Bernevig BA, Hughes TL, Zhang SC. Quantum spin hall effect and topological phase transition in HgTe quantum wells. Science. 2006;314(5806):1757.

[52] König M, Wiedmann S, Brüne C, Roth A, Buhmann H, Molenkamp LW, et al. Quantum spin hall insulator state in HgTe quantum wells. Science. 2007;318(5851):766.

[53] Roman S, Sebastian DH. Observation of phononic helical edge states in a mechanical topological insulator. Science. 2015;349(6243):47.

[54] He C, Ni X, Ge H, Sun X-CC, Chen Y-BY-FF Bin, Lu M-HH, et al. Acoustic topological insulator and robust one-way sound transport. Nat Phys [Internet]. 2016;12(12):1124. Available from: http://www.nature.com/doifinder/10.1038/nphys3867

[55] Zhang Z, Wei Q, Cheng Y, Zhang T, Wu D, Liu X. Topological Creation of Acoustic Pseudospin Multipoles in a Flow-Free Symmetry-Broken Metamaterial Lattice. Phys Rev Lett. 2017;118(8):084303.

[56] Yves S, Fleury R, Lemoult F, Fink M, Lerosey G. Topological acoustic polaritons: Robust sound manipulation at the subwavelength scale. New J Phys. 2017;19(7):075003.

[57] Zheng LY, Theocharis G, Tournat V, Gusev V. Quasitopological rotational waves in mechanical granular graphene. Phys Rev B. 2018;97(6):060101.

[58] Hafezi M, Demler EA, Lukin MD, Taylor JM. Robust optical delay lines with topological protection. Nat Phys. 2011;7(11):907.

[59] Liang GQ, Chong YD. Optical Resonator Analog of a Two-Dimensional Topological Insulator. Phys Rev Lett. 2013;110(20):203904.

[60] Peng YG, Qin CZ, Zhao DG, Shen YX, Xu XY, Bao M, et al. Experimental demonstration of anomalous Floquet topological insulator for sound. Nat Commun [Internet]. 2016;7:13368. Available from: http://dx.doi.org/10.1038/ncomms13368

[61] Yu ZQ, Ren ZQ, Lee J. Phononic topological insulators based on six-petal holey silicon structures. Sci. Rep. 2019; 9: 1805.

[62] Wu S, Wu Y, Mei J. Topological helical edge states in water waves over a topographical bottom. New J Phys. 2018;20(2):023051.

[63] Yu SY, He C, Wang Z, Liu FK, Sun XC, Li Z, et al. Elastic pseudospin transport for integratable topological phononic circuits. Nat Commun [Internet]. 2018;9:3072. Available from: http://dx.doi.org/10.1038/s41467-018-05461-5

[64] Mousavi SH, Khanikaev AB, Wang Z. Topologically protected elastic waves in phononic metamaterials. Nat Commun [Internet]. 2015;6:8682. Available from: http://dx.doi.org/10.1038/ncomms9682

[65] Miniaci M, Pal RK, Morvan B, Ruzzene M. Experimental Observation of Topologically Protected Helical Edge Modes in Patterned Elastic Plates. Phys Rev X. 2018;8(3):031074.

[66] Nie X, Yoo Y, Hewakuruppu H, Sullivan J, Krishna A, Lee J, et al. Cool White Polymer Coatings based on Glass Bubbles for Buildings. Sci Rep. 2020;10:6661.

[67] Mandal J, Fu Y, Overvig AC, Jia M, Sun K, Shi NN, et al. Hierarchically porous polymer coatings for highly efficient passive daytime radiative cooling. Science. 2018;362(6412):315.

[68] Santamouris M, Feng J. Recent progress in daytime radiative cooling: Is it the air conditioner of the future? Buildings. 2018;8(12):168.

[69] Burke M, Hsiang SM, Miguel E. Global non-linear effect of temperature on economic production. Nature. 2015;527(7577):235.

[70] Gueymard CA, Myers D, Emery K. Proposed reference irradiance spectra for solar energy systems testing. Sol Energy. 2002;73(6):443.

[71] Lord SD. A New Software Tool for Computing Earth's Atmospheric Transmission of Near- and Far-Infrared Radiation. NASA Tech Memo 103957. 1992;103957.

[72] Raman AP, Anoma MA, Zhu L, Rephaeli E, Fan S. Passive radiative cooling below ambient air temperature under direct sunlight. Nature. 2014;515(7528):540.

[73] Orel B, Gunde MK, Krainer A. Radiative cooling efficiency of white pigmented paints. Sol Energy. 1993;50(6):477.

[74] Synnefa A, Santamouris M, Livada I. A study of the thermal performance of reflective coatings for the urban environment. Sol Energy. 2006;80(8):968.

[75] Zhao D, Aili A, Zhai Y, Lu J, Kidd D, Tan G, et al. Subambient Cooling of Water: Toward Real-World Applications of Daytime Radiative Cooling. Joule. 2019;3(1):111.

[76] Zhai Y, Ma Y, David SN, Zhao D, Lou R, Tan G, et al. Scalable-manufactured randomized glass-polymer hybrid metamaterial for daytime radiative cooling. Science. 2017;355(6329):1062.

[77] Huang Z, Ruan X. Nanoparticle embedded double-layer coating for daytime radiative cooling. Int J Heat Mass Transf. 2017;104:890.

[78] Atiganyanun S, Plumley JB, Han SESJSMESJ, Hsu K, Cytrynbaum J, Peng TL, et al. Effective Radiative Cooling by Paint-Format Microsphere-Based Photonic Random Media. ACS Photonics. 2018;5(4):1181.

[79] Peoples J, Li X, Lv Y, Qiu J, Huang Z, Ruan X. A strategy of hierarchical particle sizes in nanoparticle composite for enhancing solar reflection. Int J Heat Mass Transf. 2019;131:487.

[80] Nakagawa J, Kage Y, Hori T, Shiomi J, Nomura M. Crystal structure dependent thermal conductivity in two-dimensional phononic crystal nanostructures. Appl Phys Lett [Internet]. 2015;107(2):023104. Available from: http://dx.doi.org/10.1063/1.4926653

[81] Holland M. Analysis of Lattice Thermal Conductivity. Phys Rev. 1963;132(6):2461.

[82] Callaway J. Model for lattice Thermal Conductivity at Low Temperatures. Phys Rev. 1959;113(4):1046.

[83] Mingo N, Yang L, Li D, Majumdar A. Predicting the Thermal Conductivity of Si and Ge Nanowires. Nano Lett. 2003;3(12):1713.

[84] Moore AL, Saha SK, Prasher RS, Shi L. Phonon backscattering and thermal conductivity suppression in sawtooth nanowires. Appl Phys Lett. 2008;93(8):083112.

[85] Ravichandran NK, Minnich AJ. Coherent and incoherent thermal transport in nanomeshes. Phys Rev B - Condens Matter Mater Phys. 2014;89(20):205432.

[86] Li D, Wu Y, Kim P, Shi L, Yang P, Majumdar A. Thermal conductivity of individual silicon nanowires. Appl Phys Lett. 2003;83(14):2934.

[87] Péraud JPM, Hadjiconstantinou NG. Efficient simulation of multidimensional phonon transport using energy-based variance-reduced Monte Carlo formulations. Phys Rev B - Condens Matter Mater Phys. 2011;84(20):205331.

[88] Blanc C, Rajabpour A, Volz S, Fournier T, Bourgeois O. Phonon heat conduction in corrugated silicon nanowires below the Casimir limit. Appl Phys Lett. 2013;103(4):043109.

[89] Feser JP, Sadhu JS, Azeredo BP, Hsu KH, Ma J, Kim J, et al. Thermal conductivity of silicon nanowire arrays with controlled roughness. J Appl Phys. 2012;112(11):114306.

[90] Hao Q, Xiao Y, Zhao H. Analytical model for phonon transport analysis of periodic bulk nanoporous structures. Appl Therm Eng. 2017;111:1409.

[91] Hao Q, Xiao Y, Zhao H. Characteristic length of phonon transport within periodic nanoporous thin films and two-dimensional materials. J Appl Phys. 2016;120(6 232323):065101.

[92] Romano G, Grossman JC. Toward phonon-boundary engineering in nanoporous materials Toward phonon-boundary engineering in nanoporous materials. Appl Phys Lett. 2014;105:033116.

[93] Wang Z, Alaniz JE, Jang W, Garay JE, Dames C. Thermal conductivity of nanocrystalline silicon: Importance of grain size and frequency-dependent mean free paths. Nano Lett. 2011;11(6):2206–13.

[94] Romano G, Esfarjani K, Strubbe DA, Broido D, Kolpak AM. Temperature-dependent thermal conductivity in silicon nanostructured materials studied by the Boltzmann transport equation. Phys Rev B. 2016;93(3):035408.

[95] Datta S. Electronic Transport in Mesoscopic Systems. In: Cambridge University Press [Internet]. 1997. Available from: http://adsabs.harvard.edu/abs/1997etms.book.....D

[96] Jeong C, Datta S, Lundstrom M. Full dispersion versus Debye model evaluation of lattice thermal conductivity with a Landauer approach. J Appl Phys [Internet]. 2011;109(7):073718. Available from: http://arxiv.org/abs/1011.3864%5Cnhttp://www.arxiv.org/pdf/1011.3864.pdf

[97] Hashin Z, Shtrikman S. A Variational approach to the theory of the effective magnetic permeability of multiphase materials. J Appl Phys. 1962;33(10):3125.

[98] Mingo N. Calculation of Si nanowire thermal conductivity using complete phonon dispersion relations. Phys Rev B [Internet]. 2003;68(11):113308. Available from: https://link.aps.org/doi/10.1103/PhysRevB.68.113308

[99] Pop E, Dutton RW, Goodson KE. Analytic band Monte Carlo model for electron transport in Si including acoustic and optical phonon dispersion. J Appl Phys. 2004;96(9):4998.

[100] Pop E, Dutton RW, Goodson KE. Monte Carlo simulation of Joule heating in bulk and strained silicon. Appl Phys Lett. 2005;86(8):082101.

[101] Henry AS, Chen G. Spectral phonon transport properties of silicon based on molecular dynamics simulations and lattice dynamics. J Comput Theor Nanosci. 2008;5(2):141.

[102] Hao Q. General effective medium formulation for thermal analysis of a polycrystal - The influence of partially specular phonon transmission across grain boundaries. J Appl Phys. 2014;116(3):034305.

[103] Hsieh TY, Lin H, Hsieh TJ, Huang JC. Thermal conductivity modeling of periodic porous silicon with aligned cylindrical pores. J Appl Phys. 2012;111(12):124329.

[104] Hao Q. Influence of structure disorder on the lattice thermal conductivity of polycrystals: A frequency-dependent phonon-transport study. J Appl Phys. 2012;111(1):014309.

[105] Hao Q, Zhu G, Joshi G, Wang X, Minnich A, Ren Z, et al. Theoretical studies on the thermoelectric figure of merit of nanograined bulk silicon. Appl Phys Lett. 2010;97(6):063109.

[106] Hao Q, Chen G, Jeng MS. Frequency-dependent Monte Carlo simulations of phonon transport in two-dimensional porous silicon with aligned pores. J Appl Phys. 2009;106(11):114321.

[107] Zeng Y, Marconnet A. A direct differential method for measuring thermal conductivity of thin films. Rev Sci Instrum. 2017;88(4):044901.

[108] Weber W. Adiabatic bond charge model for the phonons in diamond, Si, Ge, and α− Sn. Phys Rev B. 1977;15(10):4789.

[109] Yang F, Dames C. Mean free path spectra as a tool to understand thermal conductivity in bulk and nanostructures. Phys Rev B - Condens Matter Mater Phys. 2013;87(3):035437.

[110] Hori T, Shiomi J, Dames C. Effective phonon mean free path in polycrystalline nanostructures. Appl Phys Lett. 2015;106(17):171901.

[111] Mittal A, Mazumder S. Monte Carlo Study of Phonon Heat Conduction in Silicon Thin Films Including Contributions of Optical Phonons. J Heat Transfer [Internet].

2010;132(5):052402. Available from: http://heattransfer.asmedigitalcollection.asme.org/article.aspx?articleid=1449549

[112] Wei ZY, Wehmeyer G, Dames C, Chen YF. Geometric tuning of thermal conductivity in three-dimensional anisotropic phononic crystals. Nanoscale. 2016;8(37):16612–20.

[113] Tian Z, Esfarjani K, Shiomi J, Henry AS, Chen G. On the importance of optical phonons to thermal conductivity in nanostructures. Appl Phys Lett. 2011;99(5):053122.

[114] McGaughey AJH, Landry ES, Sellan DP, Amon CH. Size-dependent model for thin film and nanowire thermal conductivity. Appl Phys Lett. 2011;99(13):131904.

[115] ANSYS. © ANSYS, Inc. 2014. p. http://www.ansys.com/es_es.

[116] Romano G, Grossman JC. Phonon bottleneck identification in disordered nanoporous materials. Phys Rev B. 2017;96(11):115425.

[117] Park W, Romano G, Ahn ECEC, Kodama T, Park J, Barako MTMTMTMT, et al. Phonon Conduction in Silicon Nanobeam Labyrinths. Sci Rep [Internet]. 2017;7:6233. Available from: http://www.nature.com/articles/s41598-017-06479-3

[118] Wolf S, Neophytou N, Stanojevic Z, Kosina H. Monte Carlo Simulations of Thermal Conductivity in Nanoporous Si Membranes. J Electron Mater. 2014;43(10):3870.

[119] Wang H, Hu S, Takahashi K, Zhang X, Takamatsu H, Chen J. Experimental study of thermal rectification in suspended monolayer graphene. Nat Commun [Internet]. 2017;8:15843. Available from: http://www.nature.com/doifinder/10.1038/ncomms15843

[120] Iizuka H, Fan S. Consideration of enhancement of thermal rectification using metamaterial models. J Quant Spectrosc Radiat Transf [Internet]. 2014;148:156. Available from: http://dx.doi.org/10.1016/j.jqsrt.2014.07.007

[121] Zhu J, Hippalgaonkar K, Shen S, Wang K, Abate Y, Lee S, et al. Temperature-gated thermal rectifier for active heat flow control. Nano Lett. 2014;14(8):4867.

[122] Wang L, Li B. Thermal memory: A storage of phononic information. Phys Rev Lett. 2008;101(26):267203.

[123] Lo WC, Wang L, Li B. Thermal transistor: heat flux switching and modulating. J Phys Soc Japan. 2008;77(5):054402.

[124] Li B, Wang L, Casati G. Negative differential thermal resistance and thermal transistor. Appl Phys Lett. 2006;88(14):143501.

[125] Xu W, Zhang G, Li B. Interfacial thermal resistance and thermal rectification between suspended and encased single layer graphene. J Appl Phys. 2014;116:134303.

[126] Chang CW, Okawa D, Majumdar A, Zettl A. Solid-State Thermal Rectifier. Science [Internet]. 2006;314(5802):1121. Available from: http://www.sciencemag.org/cgi/doi/10.1126/science.1132898

[127] Wang L, Li B. Thermal logic gates: Computation with phonons. Phys Rev Lett. 2007;99(17):177208.

[128] Yang N, Zhang G, Li B. Thermal rectification in asymmetric graphene ribbons. Appl Phys Lett. 2009;95(3):033107.

[129] Dames C. Solid-State Thermal Rectification With Existing Bulk Materials. J Heat Transfer [Internet]. 2009;131(6):061301. Available from: http://heattransfer.asmedigitalcollection.asme.org/article.aspx?articleid=1475084

[130] Schmotz M, Maier J, Scheer E, Leiderer P. A thermal diode using phonon rectification. New J Phys. 2011;13(11):113027.

[131] Wang Y, Vallabhaneni A, Hu J, Qiu B, Chen YP, Ruan X. Phonon lateral confinement enables thermal rectification in asymmetric single-material nanostructures. Nano Lett. 2014;14(2):592.

[132] Chen Z, Wong C, Lubner S, Yee S, Miller J, Jang W, et al. A photon thermal diode. Nat Commun [Internet]. 2014;5:5446. Available from: http://www.nature.com/doifinder/10.1038/ncomms6446

[133] Liu YY, Zhou WX, Tang LM, Chen KQ. An important mechanism for thermal rectification in graded nanowires. Appl Phys Lett. 2014;105(20):203111.

[134] John Miller, Jang W, Dames C. Thermal Rectification By Ballistic Phonons in Asymmetric Nanostructures. 2009 ASME Summer Heat Transf Conf. 2009;43574:317.

[135] Feng Y, Liang X. Thermal Rectification of Silicene Nanosheets With Triangular Cavities by Molecular Dynamics Simulations. J Heat Transfer [Internet]. 2017;139(5):052402. Available from: http://heattransfer.asmedigitalcollection.asme.org/article.aspx?doi=10.1115/1.4035015

[136] Moore JE. The birth of topological insulators. Vol. 464, Nature. 2010. p. 194.

[137] Rechtsman MC, Zeuner JM, Plotnik Y, Lumer Y, Podolsky D, Dreisow F, et al. Photonic Floquet topological insulators. Nature. 2013;496(7444):196.

[138] Paulose J, Chen BGG, Vitelli V. Topological modes bound to dislocations in mechanical metamaterials. Nat Phys. 2015;11(2):153.

[139] Mei J, Chen Z, Wu Y. Pseudo-time-reversal symmetry and topological edge states in two-dimensional acoustic crystals. Sci Rep [Internet]. 2016;6:32752. Available from: http://dx.doi.org/10.1038/srep32752

[140] Xiao M, Chen WJ, He WY, Chan CT. Synthetic gauge flux and Weyl points in acoustic systems. Nat Phys. 2015;11(11):920.

[141] Huo SY, Chen JJ, Huang HB, Huang GL. Simultaneous multi-band valley-protected topological edge states of shear vertical wave in two-dimensional phononic crystals with veins. Sci Rep. 2017;7:10335.

[142] Brendel C, Peano V, Painter O, Marquardt F. Snowflake phononic topological insulator at the nanoscale. Phys Rev B. 2018;97(2):020102.

[143] Chaunsali R, Chen CW, Yang J. Subwavelength and directional control of flexural waves in zone-folding induced topological plates. Phys Rev B. 2018;97(5):054307.

[144] Liu TW, Semperlotti F. Tunable Acoustic Valley-Hall Edge States in Reconfigurable Phononic Elastic Waveguides. Phys Rev Appl [Internet]. 2018;9(1):14001. Available from: https://doi.org/10.1103/PhysRevApplied.9.014001

[145] Yang L, Yu K, Wu Y, Zhao R, Liu S. Topological spin-Hall edge states of flexural wave in perforated metamaterial plates. J Phys D Appl Phys. 2018;51(32):325302.

[146] Chaunsali R, Chen CW, Yang J. Experimental demonstration of topological waveguiding in elastic plates with local resonators. New J Phys. 2018;20(11):113036.

[147] Guo Y, Dekorsy T, Hettich M. Topological guiding of elastic waves in phononic metamaterials based on 2D pentamode structures. Sci Rep [Internet]. 2017;7(1):1–7. Available from: http://dx.doi.org/10.1038/s41598-017-18394-8

[148] Wang P, Lu L, Bertoldi K. Topological Phononic Crystals with One-Way Elastic Edge Waves. Phys Rev Lett. 2015;115(10):104302.

[149] Peano V, Brendel C, Schmidt M, Marquardt F. Topological phases of sound and light. Phys Rev X. 2015;5(3):031011.

[150] Royer D, Dieulesaint E. Elastic Waves in Solids: Free and guided propagation. In: Springer Science & Business Media [Internet]. 1999. Available from: http://books.google.fr/books?id=SzwQ1UYspyQC

[151] Landau LD, Lifshitz EM. Electrodynamics of Continuous Media, 2nd Ed. In: Butterworth-Heinemann. 1984.

[152] Ma T, Shvets G. All-Si valley-Hall photonic topological insulator. New J Phys. 2016;18(2):025012.

[153] Lu J, Qiu C, Ke M, Liu Z. Valley Vortex States in Sonic Crystals. Phys Rev Lett. 2016;116(9):093901.

[154] Pal RK, Ruzzene M. Edge waves in plates with resonators: An elastic analogue of the quantum valley Hall effect. New J Phys. 2017;19(2):025001.

[155] Brendel C, Peano V, Painter O, Marquardt F. Pseudomagnetic fields for sound at the nanoscale. Proc Natl Acad Sci [Internet]. 2017;114(17):E3390. Available from: http://arxiv.org/abs/1607.04321%0Ahttp://dx.doi.org/10.1073/pnas.1615503114

[156] Foehr A, Bilal OR, Huber SD, Daraio C. Spiral-based phononic plates: From wave beaming to topological insulators. Phys Rev Lett [Internet]. 2018;120(20):205501. Available from: http://arxiv.org/abs/1712.01360

[157] Safavi-Naeini AH, Hill JT, Meenehan S, Chan J, Gröblacher S, Painter O. Two-dimensional phononic-photonic band gap optomechanical crystal cavity. Phys Rev Lett. 2014;112(15):153603.

[158] Ghasemi Baboly M, Reinke CM, Griffin BA, El-Kady I, Leseman ZC. Acoustic waveguiding in a silicon carbide phononic crystals at microwave frequencies. Appl Phys Lett. 2018;112(10):103504.

[159] N. Kuo, S. Gong GP. Ultra High Frequency Phononic Crystal in Silicon Carbide. In: 2011

16th International Solid-State Sensors, Actuators and Microsystems Conference. 2011. p. 2486.

[160] Deng Y, Ge H, Tian Y, Lu M, Jing Y. Observation of zone folding induced acoustic topological insulators and the role of spin-mixing defects. Phys Rev B. 2017;96(18):184305.

[161] Anufriev R, Ramiere A, Maire J, Nomura M. Heat guiding and focusing using ballistic phonon transport in phononic nanostructures. Nat Commun. 2017;8:15505.

[162] Li T, Zhai Y, He S, Gan W, Wei Z, Heidarinejad M, et al. A radiative cooling structural material. Science. 2019;364(6442):760.

[163] Hsu PC, Liu C, Song AY, Zhang Z, Peng Y, Xie J, et al. A dual-mode textile for human body radiative heating and cooling. Sci Adv. 2017;3(11):e1700895.

[164] Hsu PC, Song AY, Catrysse PB, Liu C, Peng Y, Xie J, et al. Radiative human body cooling by nanoporous polyethylene textile. Science. 2016;353(6303):1019.

[165] Youngquist RC, Nurge MA, Johnson WL, Gibson TL, Surma JM. Cryogenic deep space thermal control coating. J Spacecr Rockets. 2018;55(3):622.

[166] Xie D, Yang Z, Liu X, Cui S, Zhou H, Fan T. Broadband omnidirectional light reflection and radiative heat dissipation in white beetles: Goliathus goliatus. Soft Matter. 2019;15(21):4294.

[167] Cai L, Song AY, Wu P, Hsu PC, Peng Y, Chen J, et al. Warming up human body by nanoporous metallized polyethylene textile. Nat Commun. 2017;8:496.

[168] Dai B, Li K, Shi L, Wan X, Liu X, Zhang F, et al. Bioinspired Janus Textile with Conical Micropores for Human Body Moisture and Thermal Management. Adv Mater. 2019;31(41):1904113.

[169] Fan D, Sun H, Li Q. Thermal control properties of radiative cooling foil based on transparent fluorinated polyimide. Sol Energy Mater Sol Cells. 2019;195:250.

[170] Peng Y, Chen J, Song AY, Catrysse PB, Hsu PC, Cai L, et al. Nanoporous polyethylene microfibres for large-scale radiative cooling fabric. Nat Sustain. 2018;1(2):105.

[171] Zhou L, Song H, Liang J, Singer M, Zhou M, Stegenburgs E, et al. A polydimethylsiloxane-coated metal structure for all-day radiative cooling. Nat Sustain. 2019;2(8):718.

[172] Cheng Z, Wang F, Wang H, Liang H, Ma L. Effect of embedded polydisperse glass microspheres on radiative cooling of a coating. Int J Therm Sci. 2019;140:358.

[173] Xing Z, Tay SW, Ng YH, Hong L. Porous SiO2 Hollow Spheres as a Solar Reflective Pigment for Coatings. ACS Appl Mater Interfaces. 2017;9(17):15103.

[174] Zeng G, Yang J, Hong R, Li Z, Chen Y, Li F, et al. Preparation and thermal reflectivity of nickel antimony titanium yellow rutile coated hollow glass microspheres composite pigment. Ceram Int. 2018;44(8):8788.

[175] Gao Q, Wu X, Lu D, Fan Y. Optical property and thermal performance of hollow glass microsphere/BiOBr1-xIx composites as a novel colored near infrared reflective pigment. Dye Pigment. 2018;154:21.

[176] Gao Q, Wu X, Fan Y, Meng Q. Novel near infrared reflective pigments based on hollow glass microsphere/BiOCl1-xIx composites: Optical property and superhydrophobicity. Sol Energy Mater Sol Cells. 2018;180:138.

[177] Lim Y, Lee S, Li Y, Kim S, Kang TH, Suh YD, et al. Transparent and UV-Reflective Photonic Films and Supraballs Composed of Hollow Silica Nanospheres. Part Part Syst Charact. 2020;37(4):1900405.

[178] Čekon M, Kalousek M, Hraška J, Ingeli R. Spectral optical properties and thermodynamic performance of reflective coatings in a mild climate zone. Energy Build. 2014;77:343.

[179] Sandin O, Nordin J, Jonsson M. Reflective properties of hollow microspheres in cool roof coatings. J Coatings Technol Res. 2017;14(4):817.

[180] Cai Q, Ye H, Lin Q. Analysis of the optical and thermal properties of transparent insulating materials containing gas bubbles. Appl Therm Eng. 2016;100:468.

[181] Palmer BA, Yallapragada VJ, Schiffmann N, Wormser EM, Elad N, Aflalo ED, et al. A highly reflective biogenic photonic material from core–shell birefringent nanoparticles. Nat Nanotechnol. 2020;15(2):138.

[182] Chen M, Mandal J, Ye Q, Li A, Cheng Q, Gong T, et al. A Scalable Dealloying Technique To Create Thermally Stable Plasmonic Nickel Selective Solar Absorbers. ACS Appl Energy Mater. 2019;2(9):6551.

[183] Schneider N, Zeiger C, Kolew A, Schneider M, Leuthold J, Hölscher H, et al. Nanothermoforming of hierarchical optical components utilizing shape memory polymers as active molds. Opt Mater Express. 2014;4(9):1895.

[184] Zhuang J, Tian Q, Zhou H, Liu Q, Liu P, Zhong H. Hierarchical porous TiO 2@C hollow microspheres: One-pot synthesis and enhanced visible-light photocatalysis. J Mater Chem. 2012;22(14):7036.

[185] Alden JD, Atiganyanun S, Vanderburg R, Lee SH, Plumley JB, Abudayyeh OK, et al. Radiative cooling by silicone-based coating with randomly distributed microbubble inclusions. J Photonics Energy. 2019;9(3):032705.

[186] Jacucci G, Bertolotti J, Vignolini S. Role of Anisotropy and Refractive Index in Scattering and Whiteness Optimization. Adv Opt Mater. 2019;7(23):1900980.

[187] Yuksel A, Yu ET, Cullinan M, Murthy J. Effect of particle size distribution on near-field thermal energy transfer within the nanoparticle packings. J Photonics Energy. 2019;9(3):032707.

[188] Tervo E, Francoeur M, Cola B, Zhang Z. Thermal radiation in systems of many dipoles. Phys Rev B. 2019;100(20):205422.

[189] Yuksel A, Tervo E, Cola B, Murthy J. Thermo-optical properties of packed nanoparticle

thermal interface materials. In: 2017 16th IEEE Intersociety Conference on Thermal and Thermomechanical Phenomena in Electronic Systems (ITherm). 2017. p. 164.

[190] Bohren CF, Donald R. Huffman. Absorption and scattering of light by small particles. In: Wiley. 1983.

[191] Mätzler C. MATLAB Functions for Mie Scattering and Absorption. IAP Res Rep. 2002;8(1):9.

[192] Zhang Y, Xu Y, Chen S, Lu H, Chen K, Cao Y, et al. Ultra-Broadband Directional Scattering by Colloidally Lithographed High-Index Mie Resonant Oligomers and Their Energy-Harvesting Applications. ACS Appl Mater Interfaces. 2018;10(19):16776.

[193] Shang G, Häntsch Y, Furlan KP, Janßen R, Schneider GA, Petrov A, et al. Highly selective photonic glass filter for saturated blue structural color. APL Photonics. 2019;4(4):046101.

[194] Wood DL, Nassau K. Refractive index of cubic zirconia stabilized with yttria. Appl Opt. 1982;21(16):2978.

[195] Palik ED. Handbook of optical constants of solids. In: Elsevier. 2012.

[196] Querry M. Optical Constants of Minerals and Other Materials from the Millimeter to the Ultraviolet. Vol. CRDEC-CR88, US Army Chemical Research, Development and Engineering Center, Aberdeen Proving Ground, MD. 1987.

[197] Burresi M, Cortese L, Pattelli L, Kolle M, Vukusic P, Wiersma DS, et al. Bright-white beetle scales optimise multiple scattering of light. Sci Rep. 2014;4:6075.

[198] Krenn, Angela, Youngquist, Robert, Gibson, Tracy, Snyder, Sarah, Johnson, Wesley, Wendell J. Cryogenic Thermal Control Coatings: An Overview [Internet]. Cocoa Beach, FL, United States; 2020. Available from: https://ntrs.nasa.gov/search.jsp?R=20200001076

[199] Yu Z, Nie X, Yuksel A, Lee J. Reflectivity of solid and hollow microsphere composites and the effects of uniform and varying diameters. J. Appl. Phys. 2020; 128(5): 053103.